THE DEVELOPMENT OF AN EXPERIMENTAL, LOW PROFILE, BROADBAND TRAVELLING WAVE TUBE AMPLIFIER

By

Nicolaos Vassilopoulos

Submitted in fulfilment of the academic requirements
for the degree of Doctor of Philosophy
in the Department of Electronic Engineering,
University of Natal.

Durban, May 1994.

ABSTRACT

An experimental, field replaceable travelling wave tube (TWT) with low profile, TEM transitions has been developed with the aim of combining the cost advantages of field replaceable TWTs with the bandwidth advantages of TEM transitions. Field replaceable TWTs are cheaper because their periodic permanent magnet (PPM) stacks (which are expensive) are easier to produce and can be reused. Standard TEM transitions have a high profile and prevent TWTs from being plugged into PPM stacks. The stacks of packaged TWTs are therefore built onto the tubes, using split ring magnets, before the tubes are potted. Upon failure, such tubes are discarded together with their focusing, coupling and cooling structures.

Two types of low profile, TEM transitions were investigated: a ring and a plug transition. In the former, the helix was joined to a metal ring that was sandwiched between two ceramic rings in the vacuum envelope. Due to its high shunt capacitance, this transition was narrowband. In the plug transition, the helix was joined to a small metal plug in the wall of a ceramic tube. Plug transitions with a return loss of better than 10 dB over an octave were made but some technological difficulties were encountered. Metal/ceramic joining with active solder is therefore discussed.

The development of graphite attenuators was attempted but graphite of high enough resistivity to achieve the attenuation and matching required was not available. Thin film attenuators were therefore used instead. Some good attenuators were made but the molybdenum films were sensitive to processing conditions.

An empirical procedure was developed to magnetize PPM stacks to a wanted profile. The stacks that were designed and built resulted in good beam focusing. TWT tests were made using an automated test station that was built. Maximum RF gains and output powers of 20 dB and 43 dBm respectively were measured.

The TWT design, construction and testing was a combination of materials science and microwave work. Some simulations were used to solve electromagnetic problems but much of the work was practical, involving trial and error and many measurements.

To My Mother and Father

PREFACE

The research described is part of the concluding work in the TWT Demonstrator Project that has been running at the Materials Science Laboratory of the University of Natal for several years. This Project was to demonstrate that prototype TWTs could be designed and built in South Africa. The author joined the Project research team in January 1990 after receiving a bachelor's degree from the Department of Electronic Engineering at the University of Natal.

The experimental work was carried out at the University. Most of the components required by the author were made either in the Laboratory or in the workshops of the Department. Most of the experimental structures were then assembled, brazed and welded together by the author in the Laboratory. Cold measurements were made on the RF structures using the HP8510B Vector Network Analyzer in the Radiation Laboratory of the Department. Some work was also conducted in the Advanced Communications Laboratory of the Department and in the Physics, Geology and Mechanical Engineering Departments of the University.

The author was responsible for the design, construction and testing of low profile TWTs, with TEM transitions, as whole vacuum devices. The TWT amplification theory and electron gun design were the subjects of parallel research projects by Ph.D. candidates Reynolds and Foulis and were therefore not treated in depth by the author.

Unless specifically indicated to the contrary in the text, this whole thesis is the author's own work, and has not been submitted in part, or in whole to any other university.

OUTLINE

Travelling wave tubes (TWTs) can be classified as being of either packaged or field replaceable type. Packaged tubes are commonly of metal/ceramic construction. Each tube's magnetic focusing system is built onto it before the tube is potted inside a casing. Upon failure, a packaged tube is discarded together with its magnetic focusing, collector cooling and microwave circuit coupling structures.

Field replaceable tubes have a low profile and can easily be removed from these structures. Their vacuum envelopes are made of glass and transverse electric (TE) or transverse magnetic (TM) wave transitions are used to couple to each tube's helix (or other type of slow wave structure).

Broadband, transverse electromagnetic (TEM) transitions allow for the broad bandwidth of a tube's helix to be fully utilised. TEM transitions have a high profile and cannot be used in field replaceable TWTs because coaxial lines protrude radially from the tube walls and prevent the tubes from being plugged into PPM stacks. The stacks are therefore built onto the tubes using split ring magnets.

If TWTs with TEM transitions had a low profile that allowed them to be field replaceable, both their replacement and manufacturing costs would be reduced:

TWTs have a finite service life. Although the cause of failure is random, it is often due to reduced cathode emission, the loss of vacuum or cathode heater burnout. The magnetic focusing, collector cooling, and microwave circuit structures of a TWT are less likely to fail. When a tube fails, replacement costs are reduced if it is possible to replace only the TWT and to reuse the other structures. The cost reduction is significant because the magnetic focusing system is one of the more expensive components of a TWT.

One of the final steps in the manufacture of a TWT is the adjustment of its PPM stack. Magnetic shunts are placed externally across magnets while the electron beam transmission and TWT gain are optimized. Besides being shunted, magnets are also rotated, making use of magnet imperfection related transverse fields to optimize the beam and stack alignment. Adjustment costs can exceed 10 percent of the total cost

of each TWT but are reduced if stacks can be screened before final adjustment on a TWT.

The PPM stacks of field replaceable TWTs are cheaper than those of packaged tubes because stack screening and adjustment are simpler. Since the stacks of field replaceable TWTs are not integral parts of the tubes, their fields can easily be measured. Viable stacks can then be adjusted with well-characterized electron guns and the tubes can then be tested with preadjusted stacks.

Since field replaceable, broadband TWTs would be cheaper, and hence more competitive than the presently available packaged types, the research reported in this thesis was done to develop their prototype. Active brazing techniques were used to keep manufacturing costs low and to speed up production. Two basic types of low profile, TEM transitions were investigated:

The first was a low profile transition in which the helix was joined to a metal ring that had been sandwiched between two insulating ceramic rings. These metal and ceramic rings formed part of the vacuum envelope. This design was chosen because it allowed for simple annular joint technology to be used, because it offered the option of rotating the TWT to align the PPM stack and beam axes, and because it was possible that impedance matching could be improved by moving the RF feed point around the ring. Due to its high shunt capacitance, the ring transition was narrowband and therefore offered little or no advantage over existing designs with TE or TM transitions.

The low profile transition design was therefore modified to reduce its shunt capacitance by replacing the ring with a small metal plug in the wall of a ceramic tube. This alumina tube was active brazed to a pair of molybdenum tubes in the vacuum envelope. Improved impedance matching was achieved at the expense of some technological difficulties. The author believes that a metal/ceramic TWT that can be easily removed from its PPM focusing stack because it has such low profile, plug type TEM transitions, is a distinct and original contribution to the state of the art. The author also believes that the low profile annular joints devised to join the alumina tubes to molybdenum tubes using active solder are novel.

More robust TWTs result in cost savings because they are less easily damaged. One way to improve robustness is to use high power attenuators that could safely absorb the power reflected from the output of even very poorly matched TWTs. High power attenuators that could easily be made from graphite in the University workshops were developed but graphite of high enough resistivity to achieve the attenuation and matching required was not available. These attenuators were therefore replaced by lower power attenuators made by coating the alumina helix support rods with thin films of molybdenum.

The diameter of the electron beam was initially chosen to be small in relation to the inside diameter of the helix. This low beam filling factor relaxed the requirements of the PPM stacks that had to focus the beams of several TWTs without being readjusted. A procedure was developed to magnetize PPM stacks to a wanted profile. The author believes that this procedure is novel. Although vacuum tube companies have procedures to do the same, these are unavailable for possibly proprietary reasons and were therefore not seen in the literature.

The TWTs used electron guns that were designed by Foulis. These guns had several degrees of freedom that would further reduce the costs of the low profile TWTs.

An automated test station was built and used to test the TWTs. Besides being more efficient than manual testing, automation quickens response to alarm conditions. Two low profile TWTs survived the journey from the drawing board to operation on the automated test station. Many others did not make it.

ACKNOWLEDGEMENTS

Many people helped to make this project both successful and enjoyable. I thank them all but to name each of them would be difficult, if not impossible. I am especially grateful, however, to:

My mentor, Professor Lee Nattrass, who supervised this work, for the professional advice and assistance, the personal guidance and the financial support he so willingly offered over the past few years.

Bruce Foulis, who designed the electron guns of the TWTs, for the many constructive discussions we shared and for making the Materials Science Laboratory more fun to work in.

Chris Reynolds, who provided the theoretical parallel to my more practical project, for his TWT RF performance predictions and advice, and for his contributions to the TWT test station.

Clyde Johnson for patiently and accurately machining many tiny parts out of difficult materials.

Clive Booth, for making some of the parts that were needed and for teaching me much of the practical side to vacuum tube research, a side that cannot be learnt from books alone.

Howard Reader, for his advice in microwave measurement and electromagnetics matters.

Günter Väth for aid in the design, construction, testing, and repair of electronic circuits.

UEC projects for the loan of the solid state, microwave power amplifier used in TWT testing. And the CSIR for their support of the TWT Demonstrator Project. Also the FRD, the Materials Science Laboratory and the University of Natal for providing the funds that supported me for the duration of my postgraduate studies.

CONTENTS

CHAPTER 3

REFLECTED WAVE ATTENUATOR

CHAPTER 4

PPM FOCUSING SYSTEM

CHAPTER 5

MODIFICATIONS TO AN EXISTING ELECTRON GUN DESIGN

CHAPTER 6

TWT CONSTRUCTION

CHAPTER 7

AUTOMATED TESTING OF TWTs

LIST OF TABLES, FIGURES AND PLATES

CHAPTER 1

INTRODUCTION

CHAPTER 2

LOW PROFILE, TEM TRANSITIONS TO A TWT HELIX

CHAPTER 3

REFLECTED WAVE ATTENUATOR

CHAPTER 4

PPM FOCUSING SYSTEM

LIST OF SYMBOLS

B_0	peak axial flux density
B_{air}	peak axial flux density of a magnet in air
B_{stack}	peak axial flux density of a cell in a PPM stack
c	speed of light
C_R	capacitance of the ring transition's ring
C	shunt capacitance of helix tail
C	discontinuity capacitance of transition
G	gain
L	cold loss of circuit
L	magnetic field period of a PPM stack
L	inductance of helix tail
L	discontinuity inductance of transition
P	perveance of electron gun
Q	quality factor of resonant circuit
S_{11}	reflecton coefficient from port one
S_{22}	reflecton coefficient from port two
S_{21}	forward transmission (from port one to port two)
S_{12}	reverse transmission (from port two to port one)
T	thickness of a PPM stack pole piece
v_p	phase velocity
Z_0	characteristic impedance
$Z_{0H}(f)$	characteristic impedance of a helix (as a function of frequency)
ξ	ratio of the cathode-to-switching electrode to cathode-to-anode voltages
ρ	voltage reflection coefficient
ρ_i	voltage reflection coefficient of input transition
ρ_o	voltage reflection coefficient of output transition
ρ_s	voltage reflection coefficient of sever or attenuator
τ	voltage transmission coefficient
ψ	pitch angle of helix

LIST OF ABBREVIATIONS

A/D	analogue-to-digital
CRT	cathode-ray tube
CW	continuous-wave
D/A	digital-to-analogue
DC	direct current
DUT	device under test
EB	electron-beam
HP-IB	Hewlett-Packard's IEEE 488 standard interface bus
HP ITG II	Hewlett-Packard Interactive Test Generator II software package
IF	intermediate frequency
PC	personal computer
PCB	printed circuit board
PPM	periodic permanent magnet
PVC	poly(vinyl chloride)
RF	radiofrequency
rms	root mean square
rpm	revolutions per minute
SWS	slow wave structure
TDR	time domain reflectometer
TE	transverse electric
TEM	transerse electromagnetic
TM	transverse magnetic
TWT	travelling wave tube
TWT LP8	label for low profile travelling wave tube No. 8
VSWR	voltage standing wave ratio

CHAPTER 1

INTRODUCTION

1.1 INTRODUCTION

Since this thesis is about the development of travelling wave tubes (TWTs), its introductory chapter begins with a definition of a travelling wave tube (TWT):

> A TWT is a vacuum tube that uses a continuous interaction between a linear electron beam and an electromagnetic wave, travelling at a phase velocity similar to the beam velocity, to achieve amplification of the wave.

In the following section of this chapter, the reader is shown what the TWTs that were developed looked like. The various components of a TWT are thereby introduced. How a TWT works is then explained qualitatively (a quantitative description of the electron beam/travelling wave interaction is available in Appendix A). The chapter closes with an explanation of the motivation behind the design of TWTs that have low profile, TEM, transitions to their helices.

1.2 THE COMPONENTS OF A TWT

Figure 1.1 is a cross section of one of the TWTs that were made and Figure 1.2 is a photograph of it. This tube's electron beam was produced by a modified Pierce electron gun [1] and was collected by a water-cooled collector at the other end of the TWT. A metal/ceramic vacuum envelope was used to keep air out of the tube and a periodic permanent magnet (PPM) stack provided the axial magnetic field that confined the beam inside a helix RF structure.

The helix was used to reduce the phase velocity, v_p, of a signal, fed onto the cathode-end of the helix, to the velocity of the electron beam. A wave travels along a helical wire at approximately the speed of light, c, but its phase velocity is equal to the speed of light multiplied by the sine of the pitch angle ψ:

$$v_p \approx c \sin \psi \qquad (1.1)$$

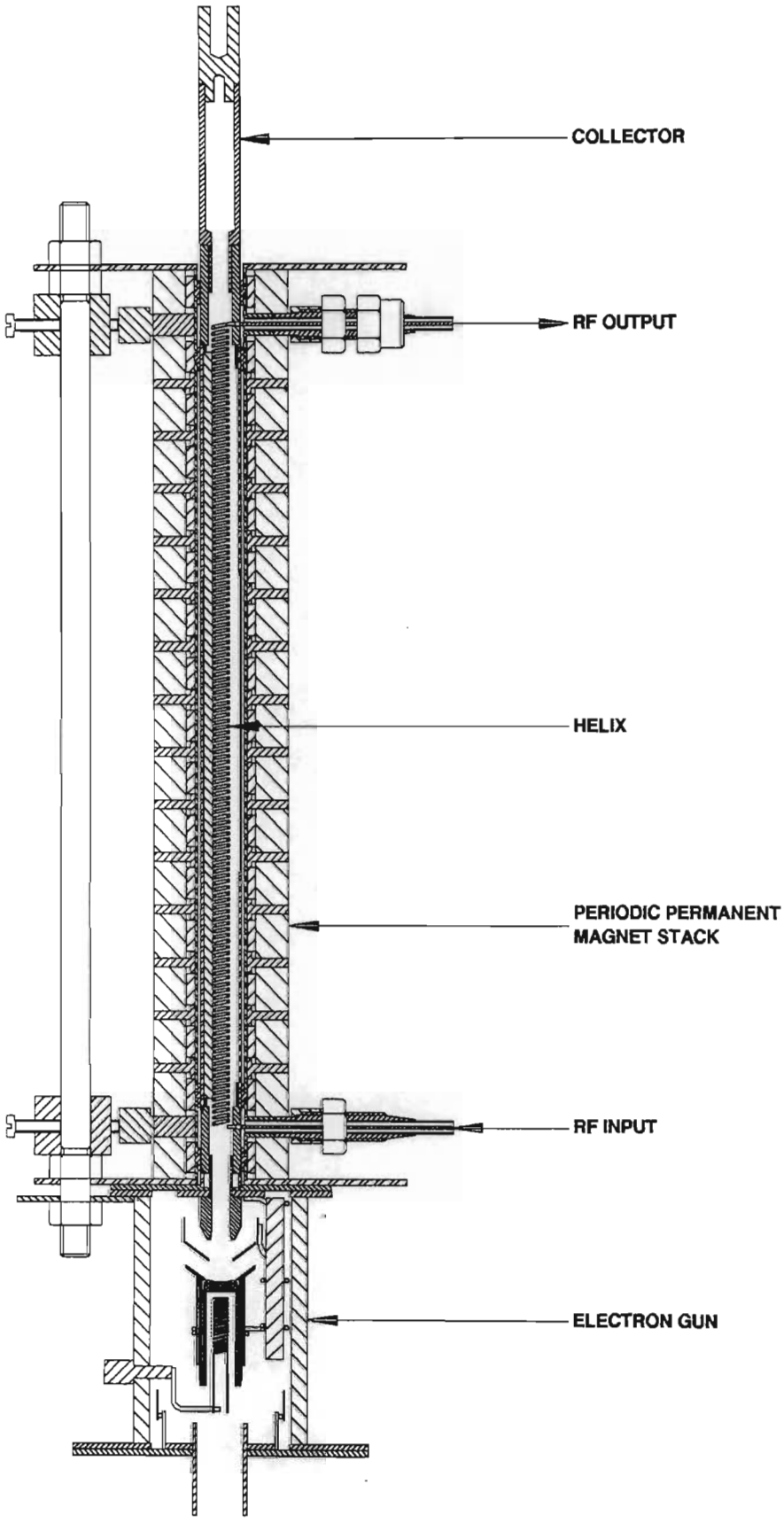

Figure 1.1 A Cross Section of TWT LP10

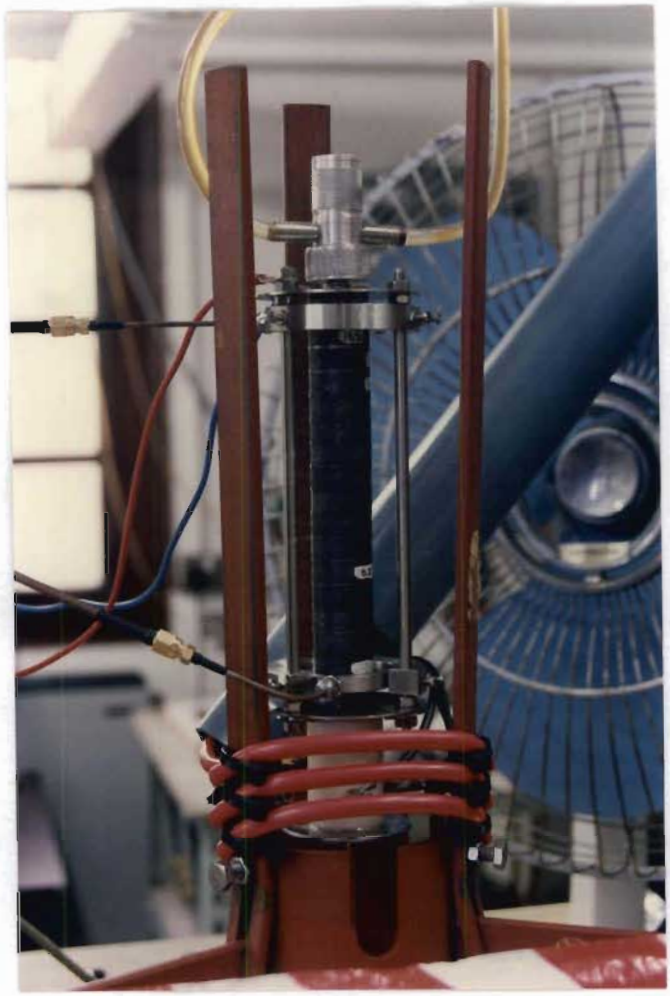

Figure 1.2 A Photograph of TWT LP10

A helix is called a slow wave structure (SWS) because it can be designed to synchronize a wave travelling along it with an electron beam travelling inside it at only a fraction of the speed of light.

Interaction occurs between the axial electric field components of a helix wave and a beam travelling down the axis of the helix. This interaction results in an energy transfer from the beam to the wave that therefore grows as it travels towards the collector-end of the helix.

Other than the helix, many other types of SWS that produce a significant axial electric field exist (examples are given in [2], [3], [4], [5]). Of all the other types of SWS, none matches the helix in bandwidth. For instance, coupled cavity TWTs typically have bandwidths of less than 25 per cent, significantly lower than the more than two octaves

achievable with helix TWTs. Coupled cavity TWTs do however have the advantage of being able to deliver higher RF output powers than their helix counterparts.

Helix TWTs typically deliver hundreds to thousands of watts of average or continuous RF power in the 650 MHz to 10 GHz frequency range [6]. Their output powers drop with increasing frequency and some tens of watts are typical at 50 GHz. Coupled cavity TWTs operate at powers of between hundreds of kilowatts at 750 MHz and hundreds of watts at 100 GHz [6].

Not shown in Figure 1.1 is the lossy section in the middle of the helix. The purpose of this attenuator is to prevent any reflections of the RF signal at the output port from being fed back to the input port. If they did, there would be a danger of them reflecting back down the tube as input signals causing oscillations or erratic variations in the gain of the tube with frequency.

1.3 A QUALITATIVE DESCRIPTION OF THE AMPLIFICATION PROCESS [3]

The electric field due to a wave on a helix is shown in Fig 1.3. In this case there are four helix turns per wavelength on the wire and the field pattern repeats every four turns. There are large axial components of electric field inside the helix. It is these axial components that allow interaction between the helix wave and the beam.

Imagine that the wave is travelling from left to right and that an electron beam is travelling with it along the axis of the helix. Some electrons are decelerated and others are accelerated by the axial electric field components. The forces on the electrons are toward the regions **P** and away from the regions **N** of Figure 1.3.

If the axial velocity of the beam is the same as that of the electric field, the electrons experience a continuous force toward regions **P** as they travel down the helix. This results in the formation of electron bunches in regions **P**.

Now, fields due to the bunching electrons in the beam cause electrons on the helix to move away from regions **P** and towards regions **N** and result in the enhancement of the field of the wave on the helix. Some amplification has occurred.

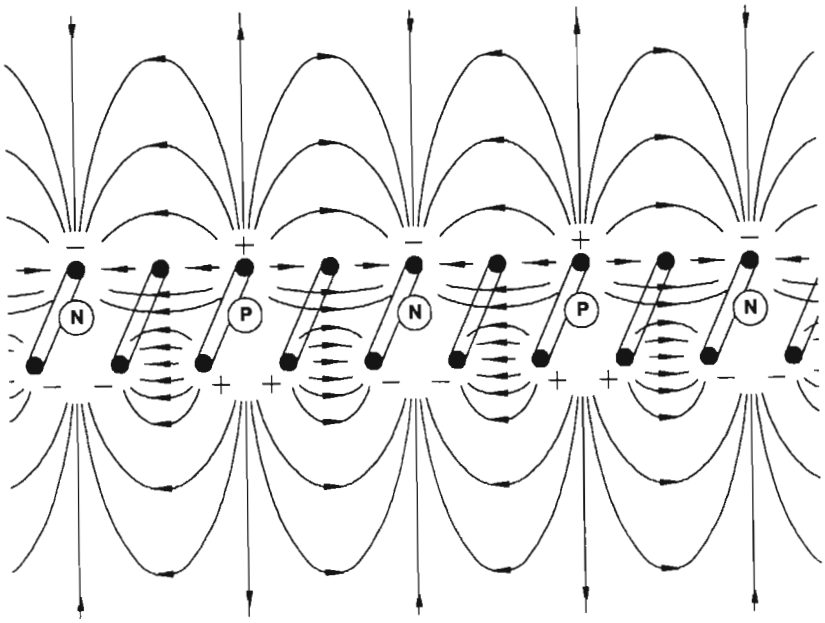

Figure 1.3 RF Charge and Electric Field Pattern For a Helix

(After A.S. Gilmour, *Microwave Tubes*, Artech House, 1986.)

The enhanced helix field causes further bunching of the beam that, in turn, causes more amplification. Signal growth continues exponentially due to these mutual interactions of the beam and the circuit, as illustrated in Figure 1.4. The resulting amplification can be approximated using the classic, simple, small-signal gain theory of Pierce (described in Appendix A) or other, later, small- or large-signal theories (such as the small-signal theory of Reynolds [7]).

The phase velocity of the growing circuit wave is always slightly less than the beam velocity (see Appendix A). This results from the requirements for energy transfer from the electron bunches to the wave. As the bunches grow, their potential energy increases and the beam's kinetic energy decreases.

Amplification is linear for small signals and nonlinear for large signals. Nonlinearities are partly due to the increasing space charge forces of growing electron bunches making further bunching more difficult. Another cause of nonlinearities is the loss of phase synchronism between the growing signal and the electron bunches that occurs as the beam slows down. For very large signals, the phase requirements for energy transfer from the bunches to the wave are no longer met and saturation occurs [8].

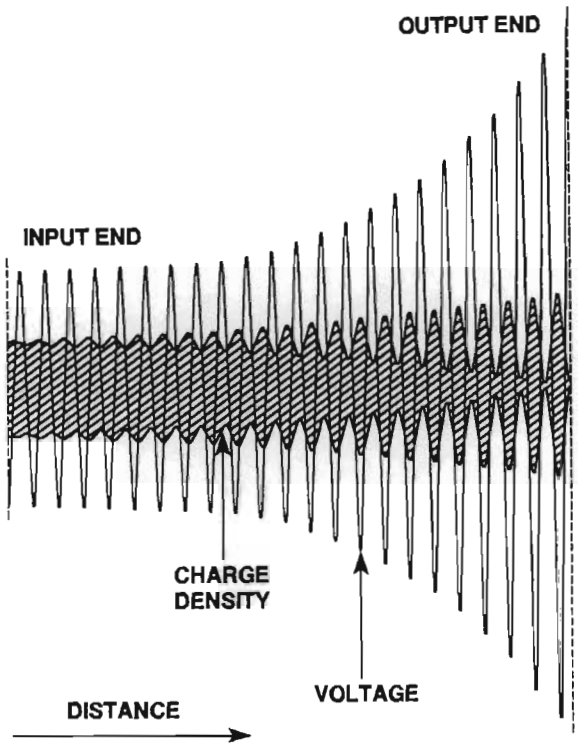

Figure 1.4 Voltage and Charge Density Build-up in a TWT

(After Reich, Ordung, Krauss and Skolnik, *Microwave Theory and Techniques*, D. Van Nostrand, Inc., 1953.)

1.4 WHY DESIGN A TWT WITH LOW PROFILE, TEM TRANSITIONS?

TWTs of many different designs have been produced since 1942, the year Kompfner invented them [9]. They can be classified as being of either packaged or field replaceable type.

Packaged tubes are commonly of metal/ceramic construction. Each tube's magnetic focusing system is built onto it before the tube is potted inside a casing. Upon failure, a packaged tube is discarded together with its magnetic focusing, collector cooling and microwave circuit coupling structures.

Field replaceable tubes have a low profile and can easily be removed from these structures. Their vacuum envelopes are made of glass and transverse electric (TE) or transverse magnetic (TM) wave transitions are used to couple to each tube's SWS.

Broadband, transverse electromagnetic (TEM) transitions allow for the broad bandwidth of a tube's helix to be fully utilised. TEM transitions have a high profile and cannot be used in field replaceable TWTs because coaxial lines protrude radially from the tube walls and prevent the tubes from being plugged into PPM stacks. Stacks are therefore built onto the tubes using split ring magnets.

If TWTs with TEM transitions had a low profile that allowed them to be field replaceable, both the replacement and manufacturing costs of the TWTs would be reduced:

TWTs have a finite service life. Although the cause of failure is random, it is often due to reduced cathode emission, the loss of vacuum or cathode heater burnout. The magnetic focusing, collector cooling, and microwave circuit structures of a TWT are less likely to fail. When a tube fails, replacement costs are reduced if it is possible to discard only the TWT and to reuse the other structures. The cost reduction is significant because the magnetic focusing system is one of the more expensive components of a TWT.

One of the final steps in the manufacture of a TWT is the adjustment of its PPM stack while the electron beam transmission and TWT gain are optimized (see Section 4.4.3 of Chapter 4). Adjustment costs can exceed 10 per cent of the total cost of each TWT [10] but are reduced if stacks can be screened before final adjustment on a TWT [11].

The PPM stacks of field replaceable TWTs are cheaper than those of packaged tubes because stack screening and adjustment are simpler. Since the stacks of field replaceable TWTs are not integral parts of the tubes, their fields can easily be measured. Viable stacks can then be adjusted with well-characterized electron guns and the tubes can then be tested with pre-adjusted stacks.

Since field replaceable, broadband TWTs would be cheaper, and hence more competitive than the presently available packaged types, the research reported in this thesis was done to develop their prototype.

The author believes that a metal/ceramic TWT that can be easily removed from its PPM focusing stack because it has low profile, TEM transitions is a distinct and original contribution to the state of the art.

REFERENCES

[1] B.D. Foulis, *A Gridless, Variable Perveance, Pierce Electron Gun*, Ph.D. Thesis, Department of Electronic Engineering, University of Natal, 1994.

[2] J.F. Gittins, *Power Travelling-Wave Tubes*, The English Universities Press Ltd, Chapter 3, 1965.

[3] A.S. Gilmour, *Microwave Tubes*, Artech House, Chapter 10, 1986.

[4] J.R. Pierce, *Traveling-Wave Tubes*, D. Van Nostrand Company, Inc., Chapter 4, 1950.

[5] J.W. Gewartowski and H.A. Watson, *Principles of Electron Tubes*, D. Van Nostrand Company, Inc., Chapters 8 and 10, 1965.

[6] Reference [3], p. 2.

[7] C.G. Reynolds, *The Analysis, Simulation and Testing of an Experimental Travelling-Wave Tube*, Ph.D. Thesis, Department of Electronic Engineering, University of Natal, 1994.

[8] Reference [2], p. 31.

[9] R. Kompfner, "The Invention of the Traveling-Wave Tube", from lecture series at the University of California at Berkley, San Fransisco Press, 1963.

[10] R.R. Moats, "Calculations of Beam Trajectories Under Non-Ideal Conditions of PPM Focusing", *IEDM*, pp. 515 to 519, 1976.

[11] D. Burnham, G.R. Ralston and F. Wohlman, Jr, "Communications TWT Magnet Stack Measurement Station", *Proceedings of the 8th International Workshop on Rare Earth Magnets and Their Applications*, Dayton, Ohio, pp. 137 to 148, May 1985.

CHAPTER 2

LOW PROFILE, TEM TRANSITIONS TO A TWT HELIX

2.1 INTRODUCTION

The reasons for designing TEM transitions with a low profile are explained in Section 1.4 of Chapter 1. This chapter introduces the problem of making the transition from a transmission line to the helix of a TWT by briefly describing four types of transition. The low profile, TEM transitions that were developed are then described in some detail from an RF point of view (constructional details are given in Chapter 6). Variations of two structures were investigated. In the first, access to the helix was via a metal ring that was brazed between two pieces of ceramic tube in the vacuum envelope of the TWT. The shunt capacitance of the ring was too high for broadband matching to be possible and a different design was developed. In this more successful design, access to the helix was via a metal plug in the wall of a ceramic tube in the TWT vacuum envelope.

2.2 SOME COMMON TYPES OF TRANSITIONS

An RF transition from a transmission line to the helix of a TWT should provide a good impedance match between the transmission line and the helix, which has a characteristic impedance that varies with frequency. Since the helix is inside a vacuum envelope, a vacuum tight RF window is needed in the signal path. This window can be part of the transition or separate from it.

A transition from a waveguide to a helix is shown in Figure 2.1. The last turn of the helix has been bent out into an antenna that couples to the electric field of the waveguide. To make a more natural transition from the helix to the antenna, the end of the helix could have been stretched out to form a taper. The choke prevents RF leakage towards the gun or the collector and the short circuit plunger is for adjustment of the impedance match. A return loss of better than 10 dB over a 30 per cent frequency band is typical for this type of transition [1]. TWTs that use such transitions can be of field replaceable type since the waveguide is not part of the vacuum envelope. The envelope is merely plugged into a hole in the waveguide and its glass wall forms the RF window.

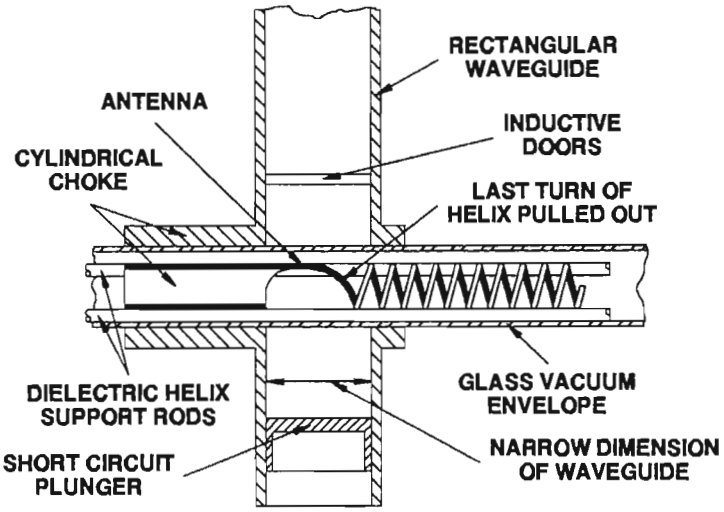

Figure 2.1 A Common Type of Waveguide to Helix Transition

(After J.F. Gittins, *Power Travelling-Wave Tubes*, The English Universities Press Ltd, 1965.)

The glass vacuum envelope of the coupled helix transition in Figure 2.2, also forms the RF window. Since the coupling structure is not part of the vacuum envelope, a TWT with coupled helix transitions can also be field replaceable. The coupling helix of this type of transition is wound in the opposite sense to, and dimensioned so that its propagation velocity is the same as, that of the TWT helix [2], [3].

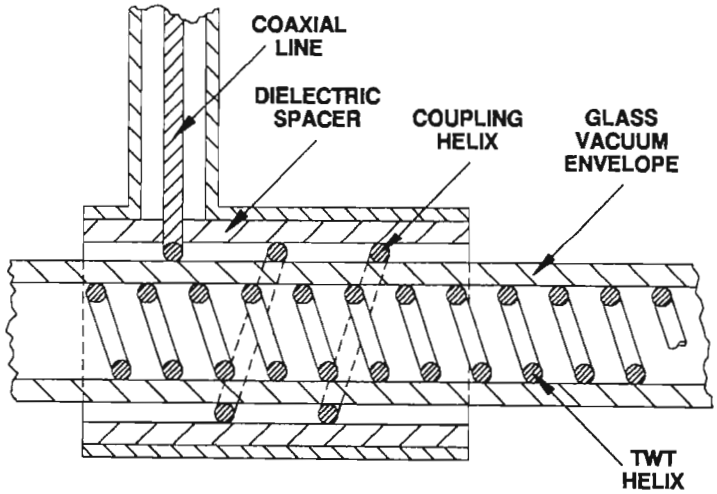

Figure 2.2 A Coupled Helix Transition

Although, if well designed, the coupled helix transition can have a broad bandwidth, it has some disadvantages: It increases the required length of a TWT's helix and the inner diameter of the tube's magnetic focusing system. The increased length and diameter of

the PPM stack result in a weight and cost increase. In addition, since a dielectric vacuum envelope is needed, a higher thermal conductivity, metallic envelope cannot be used.

A transition from coaxial line to helix with a very broad bandwidth [4] is depicted in Figure 2.3. Here, the coaxial transmission line gradually changes into a helix and the outer conductor is tapered to provide a gradual impedance change. If the transition is more than one wavelength long, excellent impedance matching is achieved [5].

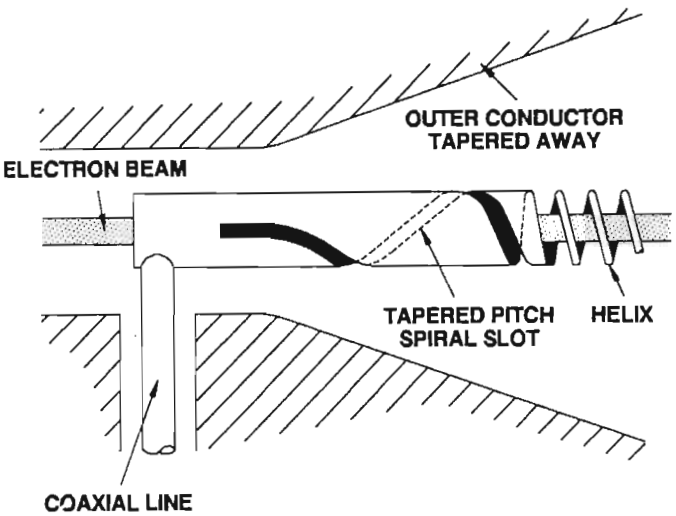

Figure 2.3 A Coaxial Line to Helix Transition with a Very Broad Bandwidth

(After J.F. Gittins, *Power Travelling-Wave Tubes*,
The English Universities Press Ltd, 1965.)

A separate RF window is needed for this transition. This window, which should be well matched, is positioned in the coaxial line some distance from the transition. Since TWTs with such transitions therefore have a high profile, with coaxial lines sticking out of the sides of their vacuum envelopes, they cannot be field replaceable.

A disadvantage of the transition of Figure 2.3 is that it occupies considerable length along the beam and hence increases the length and mass of a TWT. A broadband transition that does not take up much distance along the beam is shown in Figure 2.4. The coaxial line's centre conductor is normally tapered to transform the impedance of the line to the midband impedance of a helix (Figure 2.6 shows the impedance variation for two typical helices). The last turns of the helix can also be stretched to make a more natural transition. A match of better than 14 dB over a three to one frequency range is possible with such a transition [1]. As in the transition of Figure 2.3, a separate RF window is needed and TWTs with such transitions are not field replaceable.

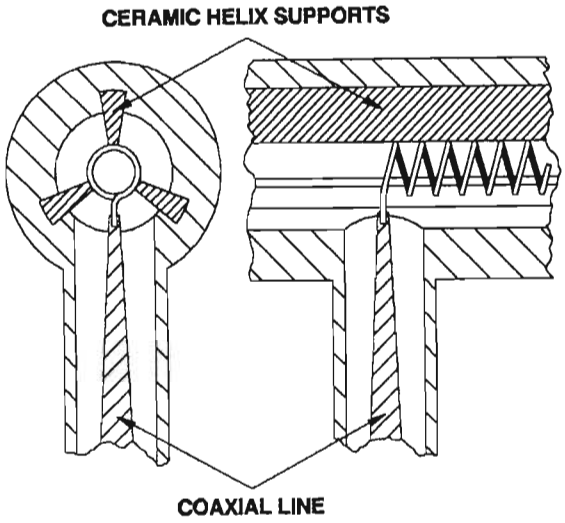

Figure 2.4 A Coaxial Line to Helix Transition with a Broad Bandwidth

(After J.F. Gittins, *Power Travelling-Wave Tubes*,
The English Universities Press Ltd, 1965.)

The first TWT Demonstrator Project TWTs that were made had transitions like the one in Figure 2.4 [6], [7], [9]. The TWTs described in this thesis had the ring or plug transitions described in the following sections.

2.3 RING TRANSITION

2.3.1 Geometry

Figure 2.5 shows the ring transition that was made. A molybdenum ring, insulated from the molybdenum TWT barrel by two pieces of alumina tube, provided a DC path between the coaxial line and the helix and gave this transition its name. Since it was part of the vacuum envelope, the ring structure also formed the vacuum window.

The coaxial line's centre conductor was pressed against the ring and the end of the helix was bent out to form a short tail that was brazed to the ring. The centre conductor passed through a hole in a molybdenum tube which fit over the ring structure. This molybdenum sleeve provided the electrical connection between the coaxial line's outer conductor and the helix sheath.

The low profile of the transition allowed the TWT to be removed from its magnet stack.

To do this, the coaxial line needed to be withdrawn. After the TWT was replaced, the line was locked back into place.

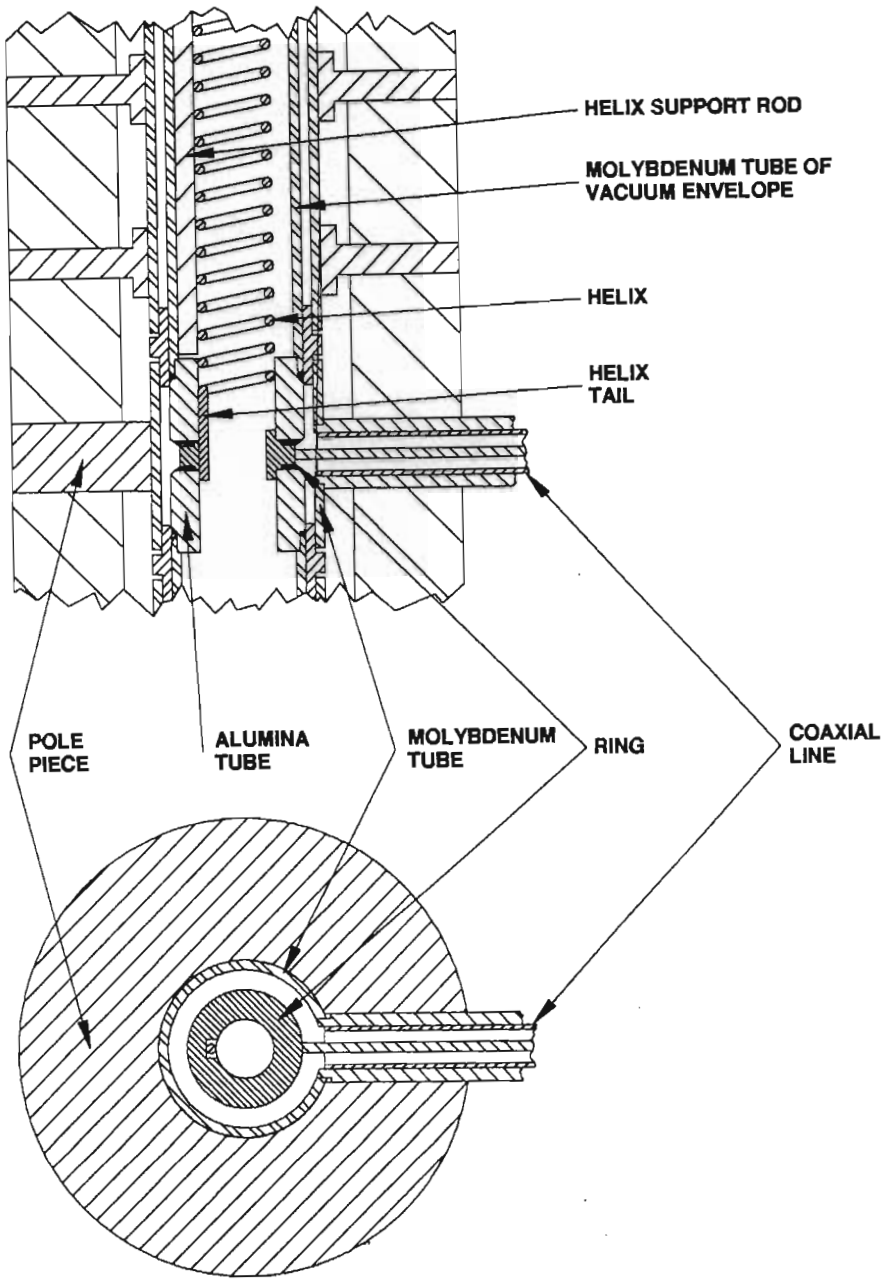

Figure 2.5 Cross Sections of the Ring Transition

This ring geometry was chosen for the following reasons: The joints between the ring and its insulators were straightforward to make; It was hoped that the impedance match could be adjusted by rotating the TWT and thereby changing the angle between the coaxial line and the ring; and if this angle was not critical, the ring would allow the tube to be rotated with respect to its magnet stack, permitting the alignment of the electron

beam and the stack axes to be optimized.

2.3.2 Simulations and Results

Helices with two sets of basic dimensions were used in the low profile TWTs. In the last two low profile TWTs, the helix dimensions were those specified by Reynolds [8]. The earlier helices had similar pitch, wire thickness and diameter as helices used in previous work in the Materials Science Laboratory [9]. The earlier and later helices had a pitch of 1.4 and 1.0 mm and an inner diameter of 3 and 2 mm respectively. All were wound with a pitch angle of 7.25° from 0.5 mm diameter tungsten wire and each helix was supported by three alumina rods inside a molybdenum sheath of 6 mm inner diameter. The characteristic impedance for each of the two helix geometries that were used is plotted in Figure 2.6 [10], [11].

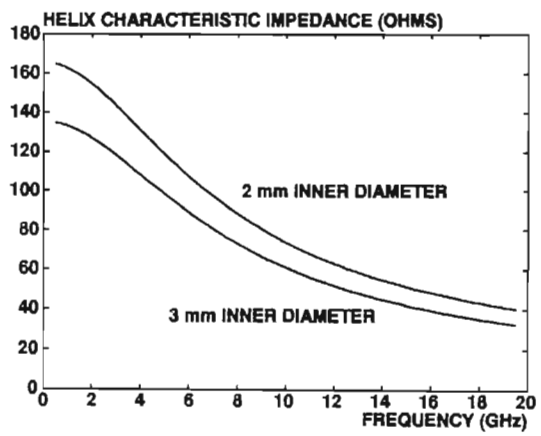

Figure 2.6 The Characteristic Impedances of the Two Helices Used

In the simple circuit model of the ring transition that is shown in Figure 2.7, the helix is considered as a lumped, resistive termination to the 50 Ω line. Since it was of 3 mm inner radius, its impedance ($\boldsymbol{Z_{0H}(f)}$) varied with frequency as plotted in the lower curve of Figure 2.6. Shunted across the helix is the capacitance of the ring ($\boldsymbol{C_R}$).

The shunt capacitance of the ring was determined as follows: MATLAB (a numeric computation software package by The MathWorks, Inc.) was used to solve Laplace's equation for a longitudinal cross section of the structure. This computation yielded an equipotential map to which field lines were added by hand using the curvilinear squares technique [12]. The capacitance per unit length between the conductors of the model was calculated from the field map [12] and was multiplied by the average circumference

of the ring to yield a value of approximately 4 pF for the ring capacitance.

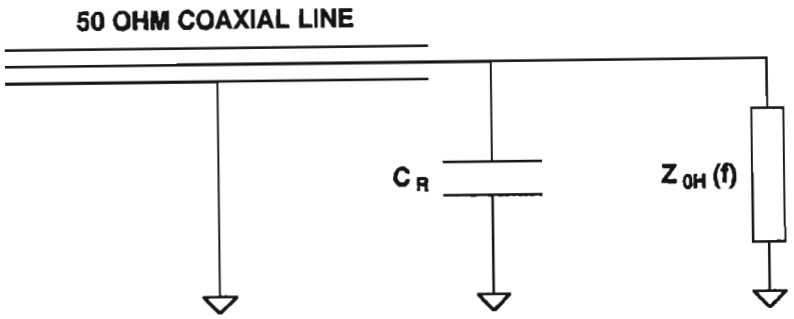

Figure 2.7 A Simple Circuit Model of the Ring Transition

The simulated reflection coefficient of the line termination in Figure 2.7 is plotted in Figure 2.8. Some results of RF measurements, made with an HP8510B network analyzer (described in Appendix B), on the ring transition are presented in Figure 2.9. The presence of a large shunt capacitance at the end of the helix is confirmed by the characteristic shape of the time domain measurement of Figure 2.9 (a). The measured reflection coefficient of the frequency domain plot of Figure 2.9 (b) was therefore very high and would have been similar to that simulated if the 300 MHz ripple, due to multiple reflections between the ring and the poorly matched TWT attenuator, had been eliminated by gating.

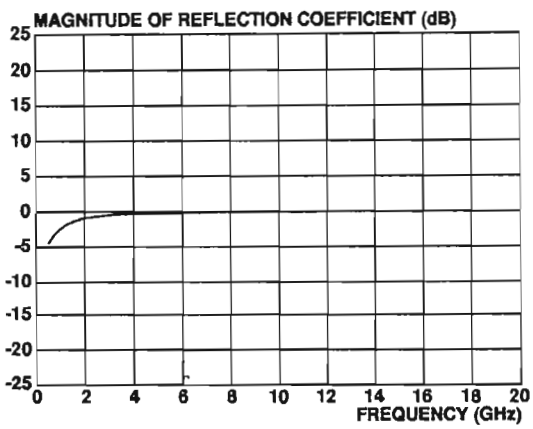

Figure 2.8 The Simulated Reflection Coefficient For the Ring Transition

The measurement in Figure 2.9 (b) was made with the point of contact of the coaxial line directly opposite the helix tail. Even worse matching was measured if the line was moved from this optimum position. A probable reason for this was that if the point of contact was moved, the two components of the signal transmitted onto the ring travelled different distances around the ring and reached the helix tail out of phase. If the point of contact of the coaxial line was directly over the helix tail, the matching was worse than if it was

directly opposite. This was possibly due to a greater discontinuity mismatch in that position.

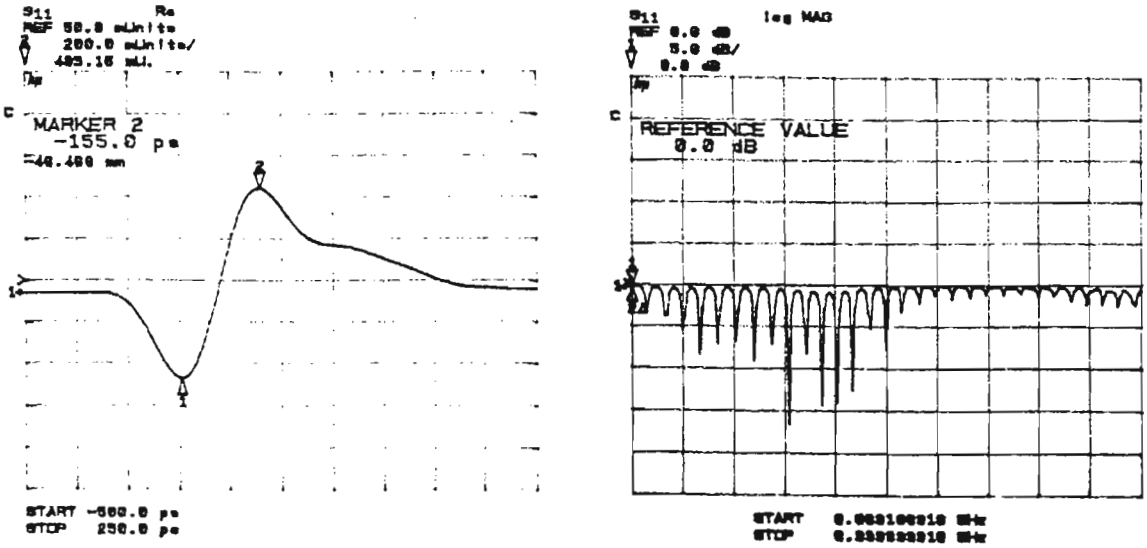

(a) Time Domain Measurement (-500 to 250 ps, 200 mUnits/)

(b) Frequency Domain Measurement (0.1 to 9 GHz, 5 dB/)

Figure 2.9 Reflection Coefficient Measurements on the Ring Transition

The susceptance of the ring could have been tuned out with a suitable matching network but this would have been a narrowband solution that was therefore not even attempted.

2.3.3 Conclusions

The low profile of the ring transition made it suitable for use in a field replaceable TWT. However, the transition did not provide a good impedance match because of the high capacitance between the transition's ring and ground. Tuning out this reactance to achieve a narrowband match would have been possible but was not attempted because a broadband, low profile transition was wanted.

2.4 PLUG TRANSITION

2.4.1 Geometry

A low profile transition with a much lower shunt capacitance than the ring transition is

shown in Figure 2.10. Connection through the vacuum envelope to the helix tail was via a 1.5 mm long, 0.7 mm diameter, metallic plug in the wall of a short tube of alumina ceramic.

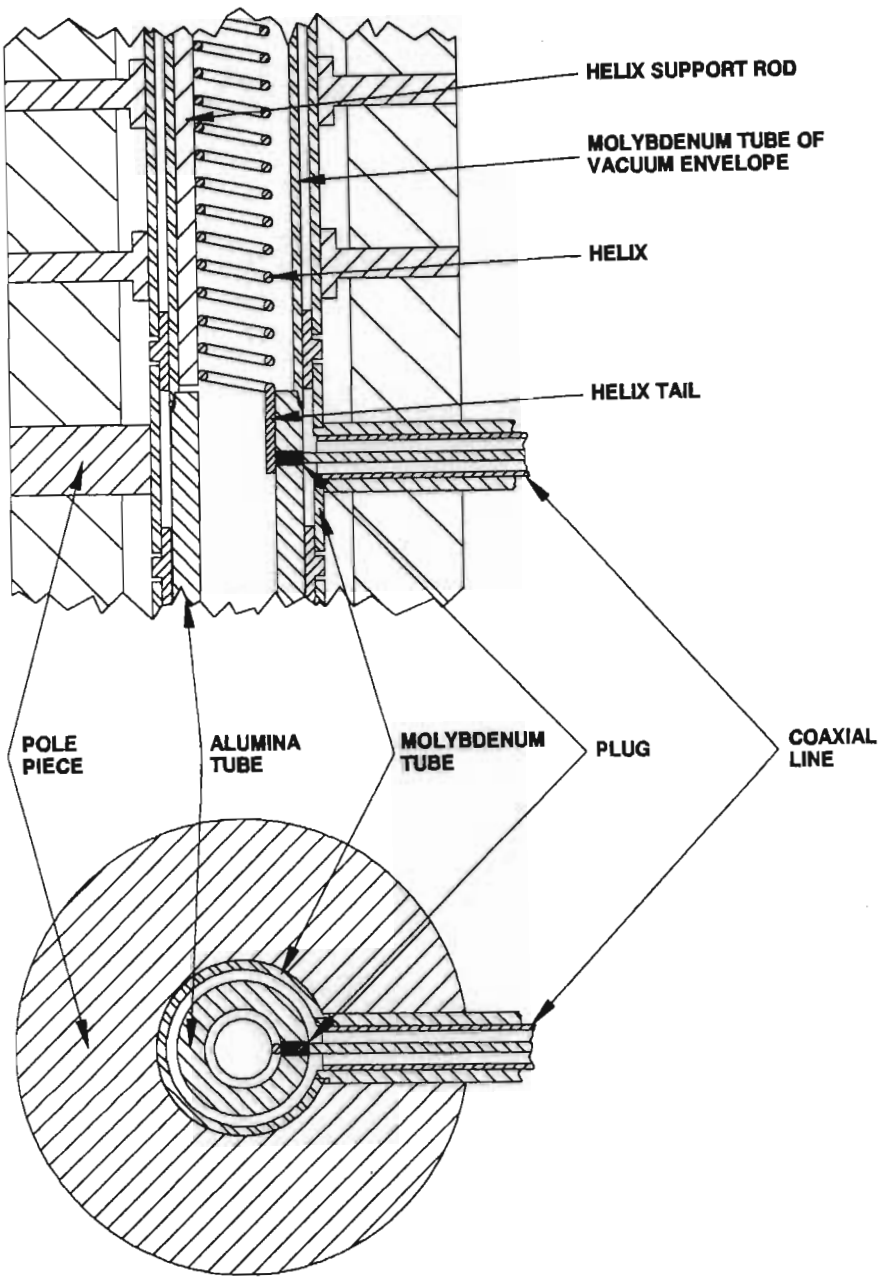

Figure 2.10 Cross Sections of a Plug Transition (3 mm inner diameter helix)

Thirteen RF structures, each with a pair of plug transitions to their helices, were built and tested. Eight of these structures had transitions that were similar to that in Figure 2.10. The two transitions of another structure differed from these only in that their plugs were in 0.7 mm diameter holes that had been countersunk as illustrated in Figure 6.11. In two

other structures, the helices had no tails, their last turns ending at plugs. Smaller, 2 mm inner diameter helices were used in the last two TWTs and their transitions were as shown in Figure 2.11.

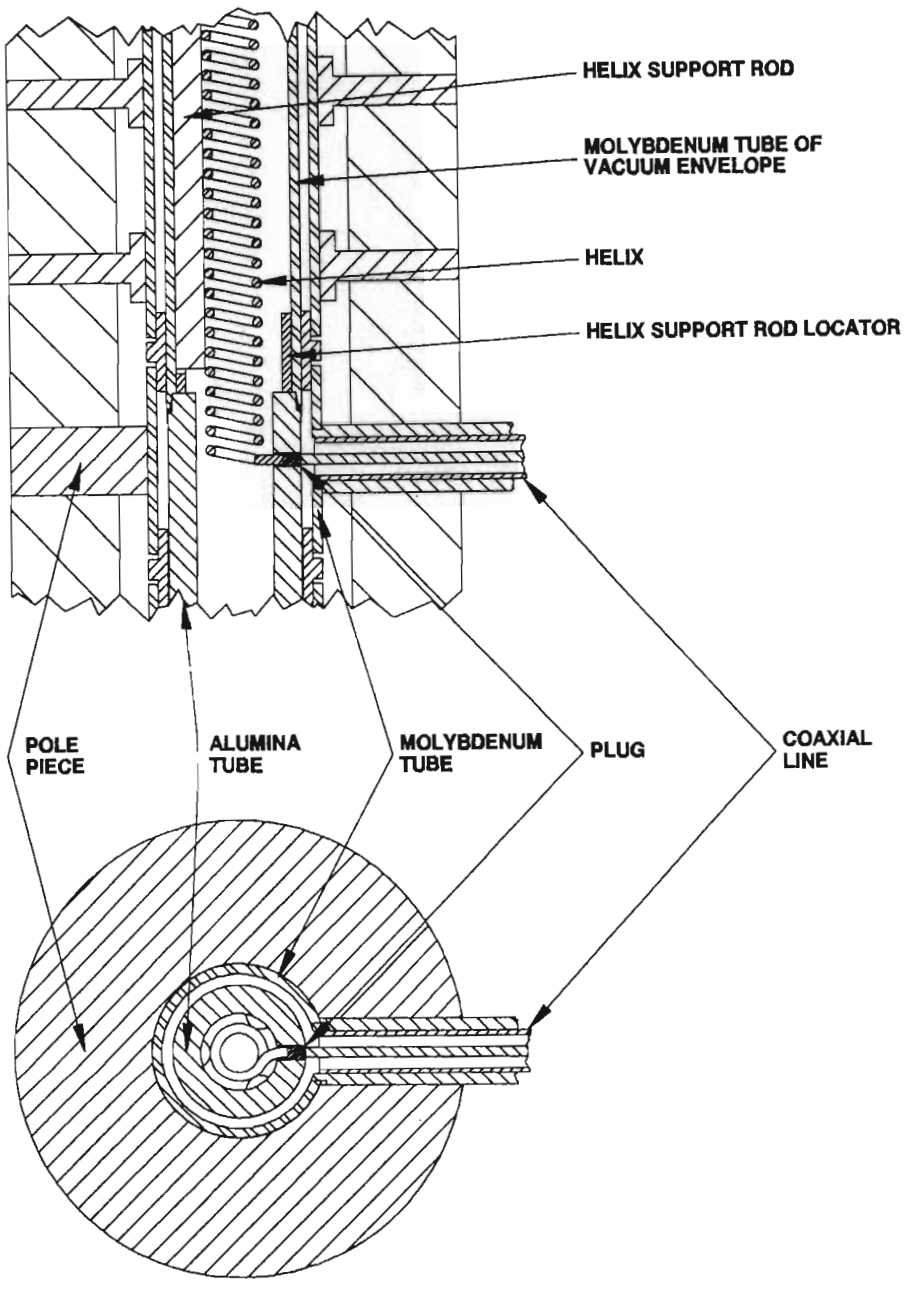

Figure 2.11 Cross Sections of a Plug Transition (2 mm inner diameter helix)

The author claims that the low profile transitions of Figures 2.5, 2.10 and 2.11 are original. Nowhere in the literature was a field replaceable, metal/ceramic TWT with broadband, TEM transitions seen mentioned. One design, due to Lichtenberg [13] and depicted in Figure 2.12, was found that had the end of its helix pass through its glass

vacuum envelope. Only in this respect was it similar to the transition of Figure 2.11, in which the end of the helix is soldered into a hole through a piece of ceramic tube in the TWT vacuum envelope.

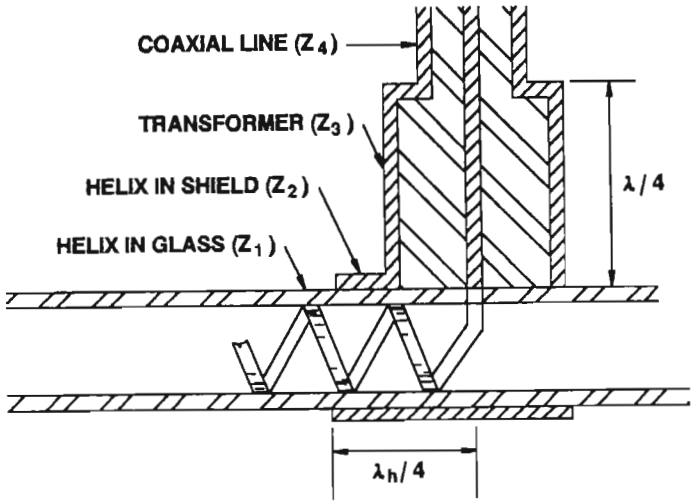

Figure 2.12 The Helix to Coaxial Line Transition of Lichtenberg

(After A.J. Lichtenberg, "Prebunched Beam Traveling-Wave Tube Studies", *IRE Transactions on Electron Devices*, pp. 345 to 351, July 1962.)

2.4.2 Simulations and Results

Figure 2.13 shows a simple circuit model of the plug transition of Figure 2.10. Here, ***C*** is the shunt capacitance of the 3.5 mm long helix tail; ***L*** is the tail's inductance; and $\boldsymbol{Z_{0H}(f)}$ is the helix impedance, which varies with frequency as plotted in the bottom curve of Figure 2.6.

C, the tail capacitance of 66 pF/m, was calculated using MSC/Magnetics, a two dimensional, finite element analysis software package, from the MacNeal-Schwendler Corporation. ***L***, the tail inductance of 555 nH/m, was approximated as follows: In the region of the 0.5 mm diameter tail, the outer conductor had a diameter of 8 mm and its axis was 1.75 mm from that of the tail. Since the tail was closer to the axis of the outer conductor than to the wall of the conductor, its inductance would not change much if it were moved to the axis. In this coaxial position its inductance would have been 555 nH/m.

Waves travelled along the tail at a phase velocity of approximately 2.4 times less than

the speed of light in a vacuum (this factor was calculated by regarding the tail as a 0.5 mm wide microstrip line with a 2 mm thick alumina substrate and a flat ground plane). So, although the physical length of the tail was only about 3.5 mm, it was a significant portion of a wavelength long at the frequencies of interest and was thus modelled as a piece of transmission line. Its characteristic impedance was calculated as 92 Ω from the above values of ***C*** and ***L***.

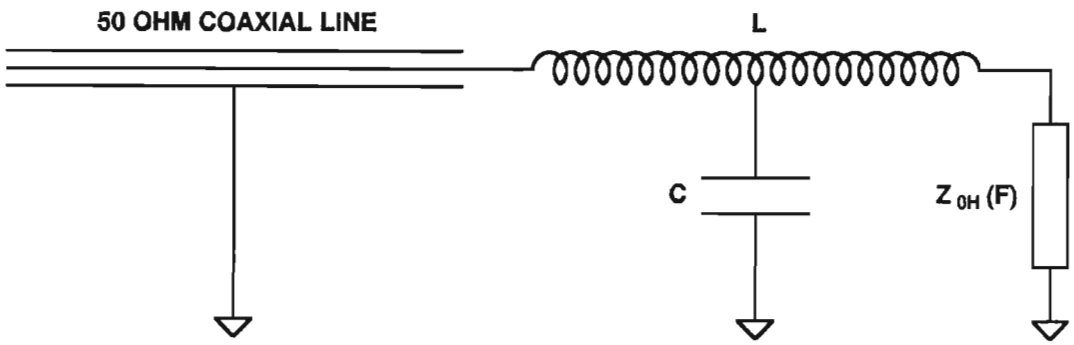

Figure 2.13 A Simple Circuit Model of the Plug Transition

The simulated reflection coefficient due to the model is plotted in Figure 2.14 (a). Some results of RF measurements on TWT LP7, a structure with transitions like the one in Figure 2.10, are presented in Figure 2.15. These measurements were made with an HP8510B network analyzer (described in Appendix B).

Figures 2.15 (a) and (b), respectively, are frequency and time domain measurements of the reflection coefficient from the input end of TWT LP7. The time domain plot shows that the dominant impedance mismatches from this end of the tube were at the plug transition (near 0 ns) and the attenuator (between 3 and 5 ns). Figure 2.15 (d) is a time domain plot of the reflection due to the transition. The three markers are the centre and limits of the gate that was used to yield the gated frequency domain plot of Figure 2.15 (c). Comparing the two frequency domain plots of Figure 2.15, it can be seen that the basic shape of the ungated curve is due to the transition. The 300 MHz ripple on this plot is due to reflections between the transition and the attenuator.

Figure 2.15 (c) shows that the transition has a match of better than 10 dB over the octave between 5 and 10 GHz. Some matching also occurs in this region of the simulated curve of Figure 2.14 (a). It is however not as good, being better than 10 dB only between 4 and 6 GHz.

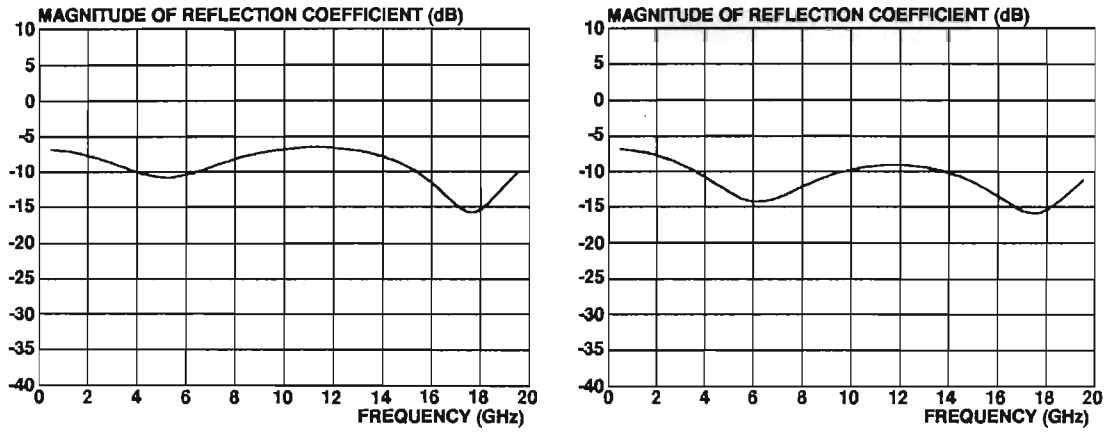

(a) 92 Ω Tail Impedance (b) 78 Ω Tail Impedance

Figure 2.14 Simulated Reflection Coefficients for the Plug Transition with a Tail

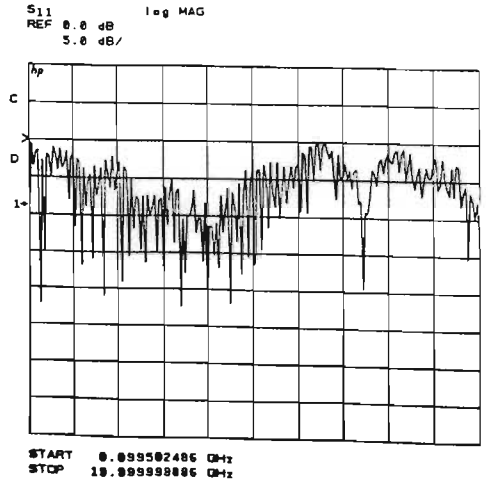

(a) Frequency Domain Measurement

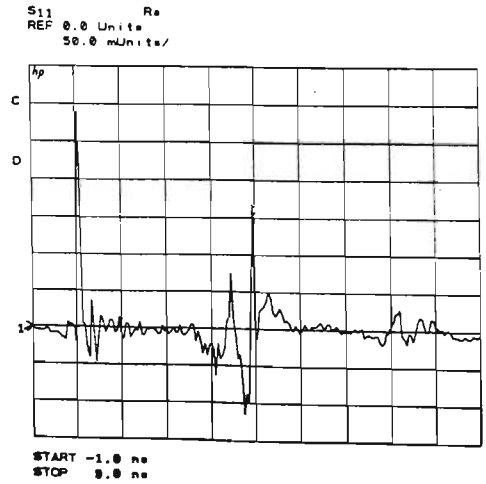

(b) Time Domain Measurement

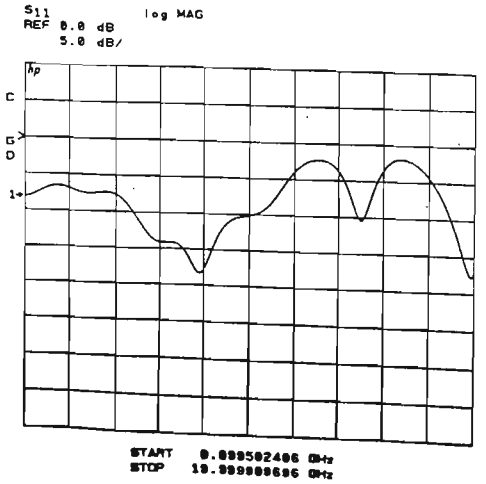

(c) Gated Frequency Domain Measurement (transition only)

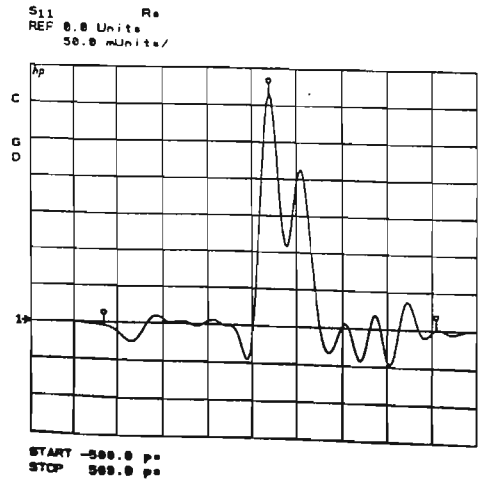

(d) Time Domain Measurement and Gate (transition only)

Figure 2.15 Reflection Coefficient Measurements on TWT LP7

Small adjustments were made to the values of the model's variables to determine its sensitivity to possible errors due to approximations. The simulated reflection coefficient was found to be most sensitive to variations in the tail impedance. Reducing the characteristic impedance of the tail from 92 to 78 Ω yielded the simulated curve of Figure 2.14 (b), which has a better than 10 dB match from 4 to 10 GHz and agrees more closely with the measured curve.

Agreement between the measured and simulated results was lower at the high frequency end of the curves where discontinuities are even larger in relation to the signal wavelength. These discontinuities were not included as lumped reactive elements in the model since the simulated and measured curves were in reasonable agreement and it would be difficult to determine the several discontinuity reactances of the complex transition.

In the time domain measurement of Figure 2.15 (d), the measurement plane (at 0 ps) was positioned at the end of the coaxial line. No large reflection was present there, indicating that the pressured butt joint between the coaxial line and the plug was good.

In time domain measurements, the time axis corresponds to the time required to travel from a reference plane to an impedance mismatch and then back to the reference plane again (see Appendix B). The first, and largest, reflection in Figure 2.15 (d) occurs 40 ps after the end of the coaxial line. This corresponds to the point where the plug meets the tail. This was concluded because the time required for a wave to travel twice through the 1.5 mm long plug would be about 30 ps (three times longer than if the plug was not surrounded by alumina dielectric). Since the reflection is positive, its amplitude of 0.315 times that of the incident pulse suggests a characteristic impedance of 96 Ω for the tail. This compares well with the 92 Ω tail impedance calculated from the values for tail inductance and capacitance given above.

The second large reflection in Figure 2.15 (d) occurs 68 ps after the first one and corresponds to the point where the helix tail bends into the first turn of the helix. This conclusion was made by considering the following: The distance along the helix tail, from the axis of the plug to the first turn of the helix, was about 3.5 mm. At a speed 2.4 times slower than that of light in a vacuum, the time taken to travel twice this distance is about 56 ps.

A reflection due to the plug is not seen in Figure 2.15 (d). It was therefore concluded that the effect of the coaxial line/plug transition was much smaller than that of the plug/tail transition. The plug had a shunt capacitance of 0.44 pF (calculated using MSC/EMAS, a two or three dimensional, finite element analysis software package from the MacNeal-Schwendler Corporation) but did not act as a lumped shunt capacitor at the transition as had been suspected. The plug was therefore not included in the models of the transitions.

Transitions made with the more massive, countersunk plugs had impedance matches that were only about 2 dB worse that those of Figure 2.15. TWT LP8 had countersunk plugs and, from 2 to 10 GHz, the return losses of its transitions varied between 6 and 15 dB, compared to the 7 and 18 dB shown in Figure 2.15 (c).

The octave bandwidth of the plug transition of Figure 2.10 could possibly have been improved by: etching or plating the tail to optimize its characteristic impedance; using an external, impedance-matching taper to transform the 50 Ω coaxial line impedance to the tail impedance; using a ceramic tube of different thickness or dielectric constant to optimize the tail impedance or electrical length; using a different physical tail length; and stretching the end of the helix out to make a more natural transition to the tail.

Plug transitions without a helix tail were made using helices of both 3 and 2 mm inner diameter. Since the results for both helix sizes were similar, only the transition of Figure 2.11 (with a 2 mm inner diameter helix) will be discussed.

By redefining C and L as the lumped discontinuity capacitance and inductance of the abrupt transitions, the simple circuit model of Figure 2.13 can be used for the tailless transitions too. $Z_{0H}(f)$ is now defined as the helix impedance inside the alumina tube of the transition. For the 2 mm inner diameter helix, this impedance was similar to that of the bottom curve of Figure 2.6, having been reduced from that of the top curve by the higher effective dielectric constant at the transition. Time domain measurements indicated that no significant reflection occurred when a wave passed from this section of helix to that of slightly higher impedance. The model therefore ignores any such effects.

Since the geometry of the transition is neither symmetrical nor simple, it would be difficult

to calculate values for ***C*** and ***L***. A few guesses were therefore made at their values to yield the simulated reflection coefficients plotted in Figure 2.16. Measured results are presented in Figure 2.17.

Figure 2.17 (b) shows that a match of better than 10 dB was measured between 11 and 14 GHz. If the discontinuity reactances are made zero, the model yields an excellent match at 11.5 GHz (curve (a)). For nonzero discontinuity reactances, the match is worsened. Two sets of discontinuity reactances produced curves (b) and (c) which look more like the measured curve than curve (a), although their simulated return loss is still too low. The model is somewhat simplistic but it was decided that the time required to solve the non-trivial problem of exactly what the effects of each component of the complex structure would have on the impedance match be better spent on the many, more urgent, practical problems that were encountered.

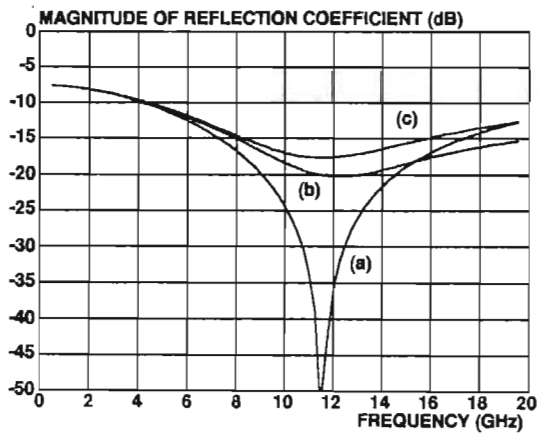

Figure 2.16 Simulated Reflection Coefficients for Plug Transition without Tail (2 mm inner diameter helix) (a) *C* = 0, *L* = 0; (b) *C* = 0.15 pF, *L* = 0.25 nH; (c) *C* = 0.12 pF, *L* = 0.12 nH

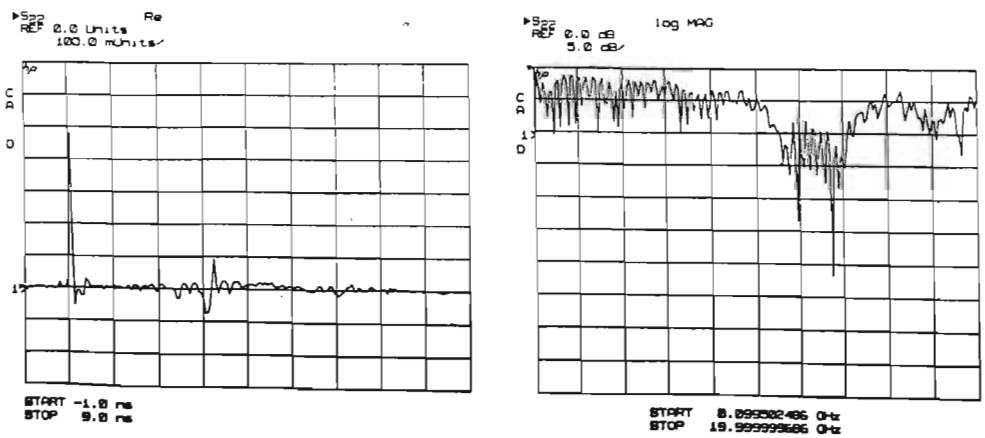

(a) Time Domain Measurement **(b) Frequency Domain Measurement**

Figure 2.17 Reflection Coefficient Measurements on TWT LP10

2.4.3 Conclusions

Four types of low profile, coaxial line to helix transitions were designed, built and tested. An acceptable match of better than 10 dB over the octave between 5 and 10 GHz was measured for the best design.

The impedance matching of the transition was due to a short tail on the end of a helix. This tail acted as an impedance transformer over an axial distance of less than three times the helix pitch. Transformation occurred inside the TWT vacuum envelope and an external transformer was not required, although it would have resulted in improved matching.

The broad bandwidth and low profile of the transition made it suitable for use in an experimental, broadband, field replaceable TWT.

REFERENCES

[1] J.F. Gittins, *Power Travelling-Wave Tubes*, The English Universities Press Ltd, Section 8.4, 1965.

[2] J.R. Pierce, *Traveling-Wave Tubes*, D. Van Nostrand Company, Inc., p. 44, 1950.

[3] Reference [1], p. 52.

[4] C.O. Lund, "A Broadband Transition from Coaxial Line to Helix", *RCA Review*, pp. 133 to 142, March 1950.

[5] A.S. Gilmour, *Microwave Tubes*, Artech House, p. 276, 1986.

[6] A.Z. Mhlongo, *Computer Aided Design and Manufacture of Co-Axial to Helix Transformers for Travelling Wave Tubes*, M.Sc. Thesis, Department of Electronic Engineering, University of Natal, 1990.

[7] N.P. Hensley, *The Construction and Testing of an Experimental Travelling Wave Tube Amplifier*, M.Sc. Thesis, Department of Electronic Engineering, University of Natal, January 1990.

[8] C.G. Reynolds, *The Analysis, Simulation and Testing of an Experimental Travelling-Wave Tube*, Ph.D. Thesis, Department of Electronic Engineering, University of Natal, 1994.

[9] E.W. Schumann, A.W. Stokes, D.M. Smith and H.L. Nattrass, "Development of an Experimental Travelling Wave Tube", *Proceedings of the Symposium on Antennas and Propagation and Microwave Theory and Techniques*, Somerset West, South Africa, pp. 157 to 164, August 1990.

[10] B.N. Basu, "Equivalent Circuit Analysis of a Dielectric-Supported Helix in a Metal Shell", *Int. J. Electronics*, Vol. 47, No. 3, pp. 311 to 314, 1979.

[11] P.K. Jain, K.V.R. Murty, S.N. Joshi and B.N. Basu, "Effect of the Finite Thickness

of the Helix Wire on the Characteristics of the Helical Slow-Wave Structure of a Traveling-Wave Tube", *IEEE Transactions on Electron devices*, Vol. ED-34, No. 5, pp. 1209 to 1213, May 1987.

[12] S. Ramo, J.R. Whinnery and T. Van Duzer, *Fields and Waves in Communication Electronics*, John Wiley & Sons, pp. 53 to 58, 1984.

[13] A.J. Lichtenberg, "Prebunched Beam Traveling-Wave Tube Studies", *IRE Transactions on Electron Devices*, pp. 345 to 351, July 1962.

CHAPTER 3

REFLECTED WAVE ATTENUATOR

3.1 INTRODUCTION

This chapter begins with an explanation of the purpose of a reflected-wave attenuator. Common methods and materials used to achieve attenuation are then discussed. Finally, the development of solid-graphite and of molybdenum film attenuators for the low profile TWTs is described from both a manufacturing and a performance point of view.

3.2 BACKGROUND

3.2.1 TWT Stability Requirements

If power reflected from an impedance mismatch at the output of a TWT is allowed to travel back down the slow wave structure to the input, part of this signal might similarly be re-reflected as an input signal. If the amplitude of this feedback signal is large enough, and if its phase is such that the feedback is positive, the TWT will oscillate.

Consider the simple TWT of Figure 3.1. Here the gain is G dB, the cold loss is L dB and the voltage reflection coefficients from the input and output transitions are ρ_i and ρ_o respectively. Oscillations may occur when

$$G - L + 20\log|\rho_o| + 20\log|\rho_i| > 0 \qquad (3.1)$$

If the left-hand side of equation (3.1) is only slightly negative, the TWT will be stable, but severe variations of gain as a function of frequency will occur.

In principle, equation (3.1) suggests that any value of stable gain can be achieved by introducing sufficient cold loss. This is not normally practical as a loss of more than about 6 dB results in a serious reduction of TWT efficiency [1]. It is difficult to achieve a return loss (- 20 log $|\rho|$) of much better than 10 dB for the transitions to and from the slow wave structure across the whole frequency band of a TWT [1]. The small signal gain is therefore limited to about 26 dB if the tube is to be stable and to about 20 dB if large gain ripple is to be avoided.

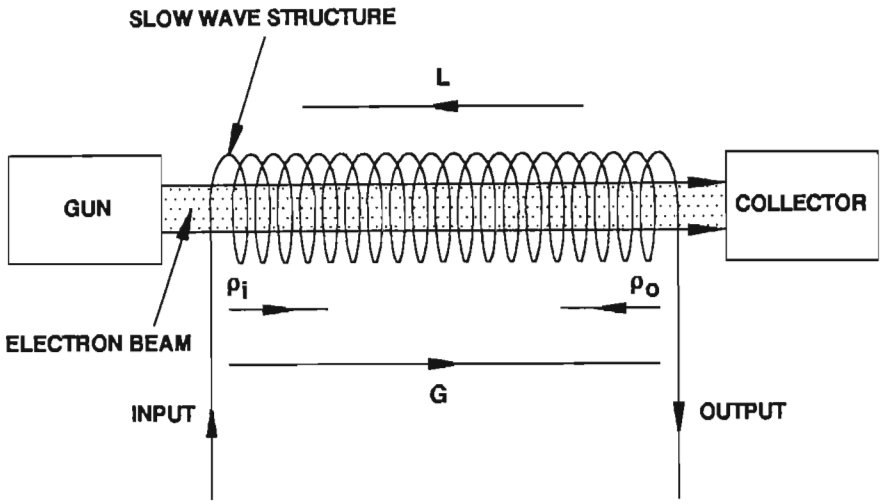

Figure 3.1 Single-Section Unsevered TWT

(After J.F. Gittins, *Power Travelling Wave Tubes*, The English Universities Press Ltd, 1965.)

The stable gain limit of about 26 dB is exceeded by introducing loss into the feedback path. Severing the slow wave structure into two parts, as shown in Figure 3.2, breaks the feedback path but RF signals are carried across the sever in the forward direction by the current and velocity modulations of the electron beam.

Matched loads, at each severed end, absorb the signals incident on them but if these loads are not perfectly matched, they will also cause reflections. There is therefore a maximum stable gain for each section of a severed tube. In the input section of the tube shown in Figure 3.2, instabilities may occur when

$$G_1 - L_i + 20\log|\rho_s| + 20\log|\rho_i| > 0 \qquad (3.2)$$

where G_1 is the gain of the input section in dB, L_i is its cold loss in dB and ρ_s and ρ_i are the voltage reflection coefficients of the sever load and of the input transition respectively. It is commonly possible to keep the reflection coefficient of a sever load lower than that of the input and output transitions. This allows the maximum stable gain per section to be higher than that for a single-section tube.

There is, however, some signal loss in the sever region. Long severs result in increased velocity spread in the beam and reduced efficiency. The total tube gain is therefore less than that of the sum of each section but nevertheless considerably higher than that for an unsevered tube. Even higher gains are possible with more than one sever.

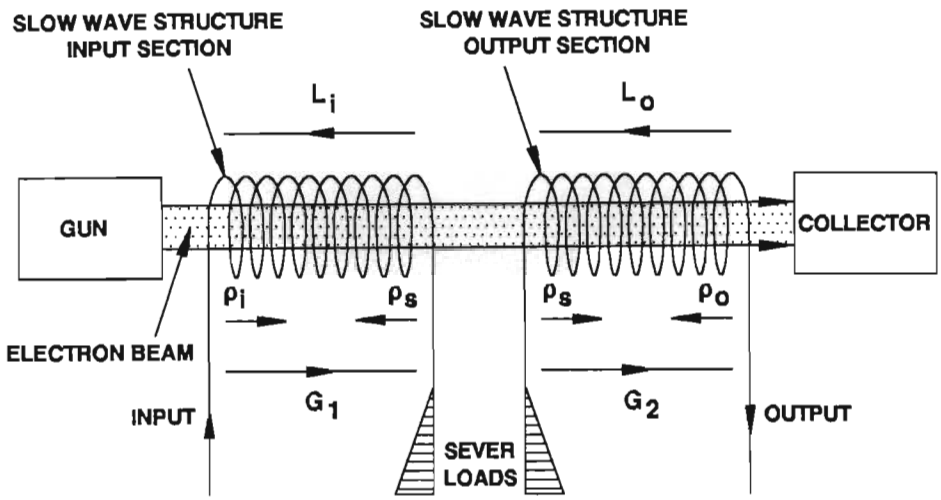

Figure 3.2 Two-Section Severed TWT

(After J.F. Gittins, *Power Travelling Wave Tubes*,
The English Universities Press Ltd, 1965.)

An alternative to a physical sever is to make part of the slow wave structure highly lossy. This attenuating region effectively severs the slow wave structure. Attenuators that are very well matched over a broad band can be made by gradually introducing the loss over several circuit wavelengths. However, this results in the attenuator occupying a considerable length along the beam. Along this length the circuit signal is too weak to control the bunching process and the velocity spread in the beam increases, reducing efficiency. In general, attenuators can be made to provide better matching than severs and they are therefore ideal for high gain, low power tubes in which efficiency is less important. Efficiency is more important in lower gain, high power tubes and such tubes tend to use severs.

The position of the attenuator is important from an efficiency point of view. If maximum efficiency is to be achieved, it is recommended that loss be avoided near the input and output of a TWT [2], [3]. Loss is therefore usually placed in the centre of a tube [2].

Nonreciprocal attenuators that employ ferrites can also be used to ensure stability. Their main advantage is that they introduce very little circuit loss in the forward direction and this results in increased efficiency [4]. Their main disadvantage, however, is in the considerable difficulties involved with incorporating the ferrite material inside the vacuum envelope of a TWT [5].

3.2.2 Obtaining RF Loss

RF loss is most commonly provided by resistive materials. Not only must these materials have appropriate resistivities, they must also be suitable for use in vacuum tubes. In addition to the high vacuum requirements of having a low vapour pressure and being capable of being outgassed, the materials must be stable and survive whatever temperatures they will reach during tube processing and operation without suffering any major changes in resistivity.

There are two classes of such materials: those of low resistance, placed in regions of high current, and those of high resistance, positioned in regions of high electric field.

Low resistance materials can be coated on conductors to a thickness greater than the skin depth. Two such materials are "Kanthall", a cobalt-iron-chromium-aluminium alloy, and iron. Both materials are magnetic and must only be applied in coatings that are thin enough to saturate without significantly altering the beam focusing field.

High resistance films can be achieved by coating dielectrics with thin layers of metal or carbon. Glass, silica, mica and alumina are all suitable dielectrics. Evaporated metal films are made by techniques such as RF sputtering and spraying. Coating with carbon is possible by thermal cracking of hydrocarbons [6], [7], and by painting or spraying of a colloidal graphite suspension. Two well-known aqueous suspensions of colloidal graphite are "Aquadag" and "Hydrokollag" and a well known mineral oil suspension is "Oildag" [8]. Carbon films are removed if heated in the presence of water [6] and this must be avoided in TWT processing.

A common example of a high resistance film attenuator is shown in Figure 3.3. Parts of the dielectric helix support rods are coated with a lossy carbon or metal film. The thickness of the film is gradually tapered to zero at the ends of the attenuator by suitable masking [9], [10] and this results in a good impedance match over a wide frequency range. An optimum value of resistivity exists for maximum attenuation per unit length [11], [12]. This is obvious, since neither a perfect insulator nor a perfect conductor are resistively lossy.

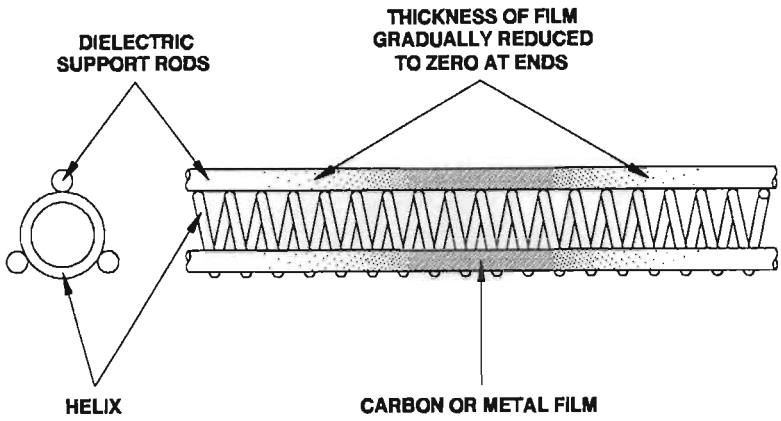

Figure 3.3 Film Attenuator Used With a Helix

Carbon film attenuators are useful for low power dissipation only. Metal film attenuators can dissipate a little more power than those made of carbon but bulk loss materials are needed for high power dissipation. One way of making these is by loading porous ceramic bodies with carbon produced by thermal cracking of hydrocarbons. The amount of loss is determined by the amount of carbon that is deposited.

A drawback of carbon-loaded, porous ceramics is that the carbon deposited in them must not be heated in the presence of water or oxygen since this will remove it. Outgassing of porous ceramics can also be a problem, and they must never come into contact with greases, solvents, or their vapours. Once these are absorbed into the pores of the ceramic, they are nearly impossible to remove [7].

Carbon/ceramic and metal/ceramic mixtures have largely replaced porous ceramics due to their very much lower outgassing rates, better thermal conductivity and lower susceptibility to attack by water vapour [7], [6]. The resistivities of these mixtures depend on their recipes. Examples of such mixtures are "Ceralloy" a hot-pressed, nonporous mixture of ceramics, such as alumina, and silicon carbide [7] and "Caberlox" a high thermal conductivity carbon/beryllia mixture [6].

High power attenuators can be made by fitting tubes or collars of lossy ceramic around a helix [12]. A cross section of a high power attenuator for a helix TWT is shown in Figure 3.4. Three carbon or metal loaded ceramic fingers are supported between the helix support rods. The finger support structure (not shown in Figure 3.4) must provide a low thermal conductivity path through which the generated heat can flow out of the

tube. Loads of this type that are suitable for use with a helix having four turns per wavelength at 5 GHz can absorb about 100 W [13].

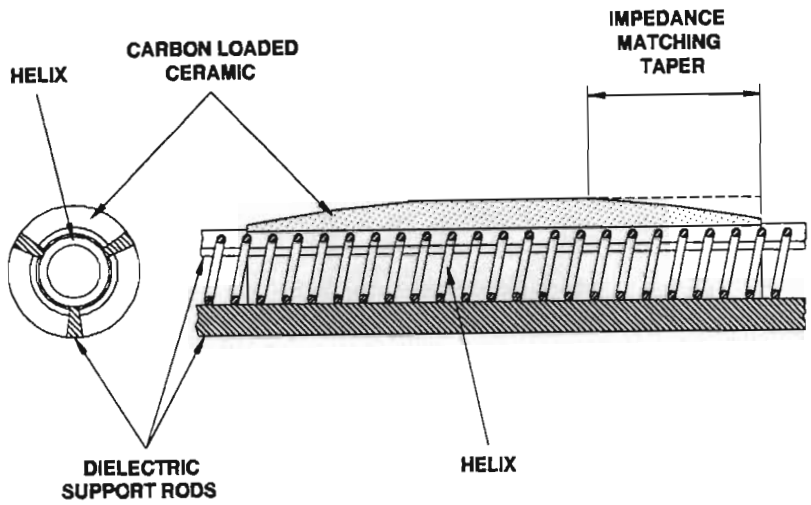

Figure 3.4 End View and Cross Section of a High Power Attenuator for a Helix

Making attenuators requires trial and error to produce the correct resistivity. Even when a procedure has been finalised there is often still a considerable resistance scatter. Final selection should be made by RF measurement of loss as there is little correlation with DC resistivity [6], [10].

3.2.3 Attenuators for the Low Profile TWTs

The attenuators' RF specifications were obtained from the TWT stability requirements (see Section 3.2.1). If worst case input and output port reflection coefficients of unity magnitude are assumed, the instability condition of equation (3.1) becomes:

$$G - L > 0 \tag{3.3}$$

To keep the left-hand side of equation (3.3) negative, the attenuation (L) is required to be higher than the gain (G) of the TWT. Gain predictions for the TWTs [14] suggested minimum attenuations of 40 and 50 dB for the tubes with larger and smaller radius helices respectively.

If a worst case cold loss of zero and a worst case input port reflection coefficient of unity magnitude is assumed, the instability condition of equation (3.2) becomes:

$$G_1 + 20\log|\rho_s| > 0 \qquad (3.4)$$

To keep the left-hand side of equation (3.4) negative, an attenuator return loss (- 20 log $|\rho_s|$) greater than the gain of the input section (G_1) is required. There is a similar requirement for stability of the output section of a TWT.

The attenuators were placed in the centre of the tubes. Assuming that the gain per section was similar, the required attenuator return loss was better than half the total TWT gain. The gain predictions [14] suggested return losses of 20 and 25 dB for the larger and smaller radius helix tubes respectively.

It was important that the attenuators not provide a DC path from the helix to the helix sheath, which was at anode potential, as this would not allow the helix current to be measured separately from the anode current. Measurements of the helix interception current were needed for evaluation and optimization of the PPM beam focusing system.

Besides satisfying the general material requirements for a vacuum tube attenuator (See Section 3.2.2), the attenuator material was required to withstand a 950°C vacuum brazing process and to be readily available and workable.

A bulk loss attenuator is capable of absorbing large amounts of power and would be useful in an experimental TWT since it would be robust enough to survive even a short or open circuit on the TWT output and possible high helix temperatures due to beam interception. Carbon or metal loaded ceramic, from which to make this attenuator, was not readily available but graphite, while not ideal, was. It was chosen because of its high thermal conductivity, its low cost, the relative ease of machining it, and its gettering properties [8].

The graphite attenuators that were developed had some disadvantages. Since their high power-handling ability was not important from a TWT stability point of view, they were replaced with lower power, high resistance film attenuators. Making such attenuators by coating the helix support rods with "Aquadag" has been investigated in the Materials Science Laboratory [15] but the technology was not used for the low profile TWT attenuators because it involves a long learning curve of trial and error before reliable adhesion is achieved. Instead, an electron beam welder was used to evaporate molybdenum for coating the helix support rods. This method was quicker than the

"Aquadag" method with less care being needed in cleaning the rods and more strongly adhesive coatings being achieved.

3.3 GRAPHITE ATTENUATOR

3.3.1 Geometry and Manufacture

A solid graphite attenuator was used in an earlier experimental TWT that had a gain of approximately 12 dB at 7 GHz [16]. This attenuator, a cross section of which is shown in Figure 3.5 (a), consisted of a tapered graphite cylinder that had been split longitudinally into three pieces that fit between the three alumina helix support rods. Due to the difficulty of positioning three loose attenuator parts in the middle of a long helix sheath, this design was not suitable for use in the low profile TWTs.

A series of ten different graphite attenuator geometries was built and tested in an attempt to develop a practical solid-graphite attenuator more suitable for the low profile TWTs [17]. All ten geometries were for a tungsten helix of 4 mm outer diameter and a molybdenum helix sheath of 6 mm inner diameter. The 0.5 mm diameter helix wire was wound to a 1.4 mm pitch. Each attenuator was similar to one or other of the six basic geometries shown in cross section in Figures 3.5 (b) to 3.5 (g). These can be described as graphite cylinders with tapered ends. Each cylinder had three longitudinal holes or slots in the walls of each end. The tapers were for impedance matching and the holes or slots were used to locate the helix support rods. An increase in the mechanical strength of the graphite structures was achieved by having the rods of one end at 60° relative to the other end. The attenuators were nevertheless fragile and were therefore reinforced with molybdenum tube in the two geometries of Figures 3.5 (f) and (g).

Care was taken not to contaminate the attenuators during and after their manufacture because graphite, due to its strong absorbing power, should be cleaned only mechanically or by heating in high vacuum [8].

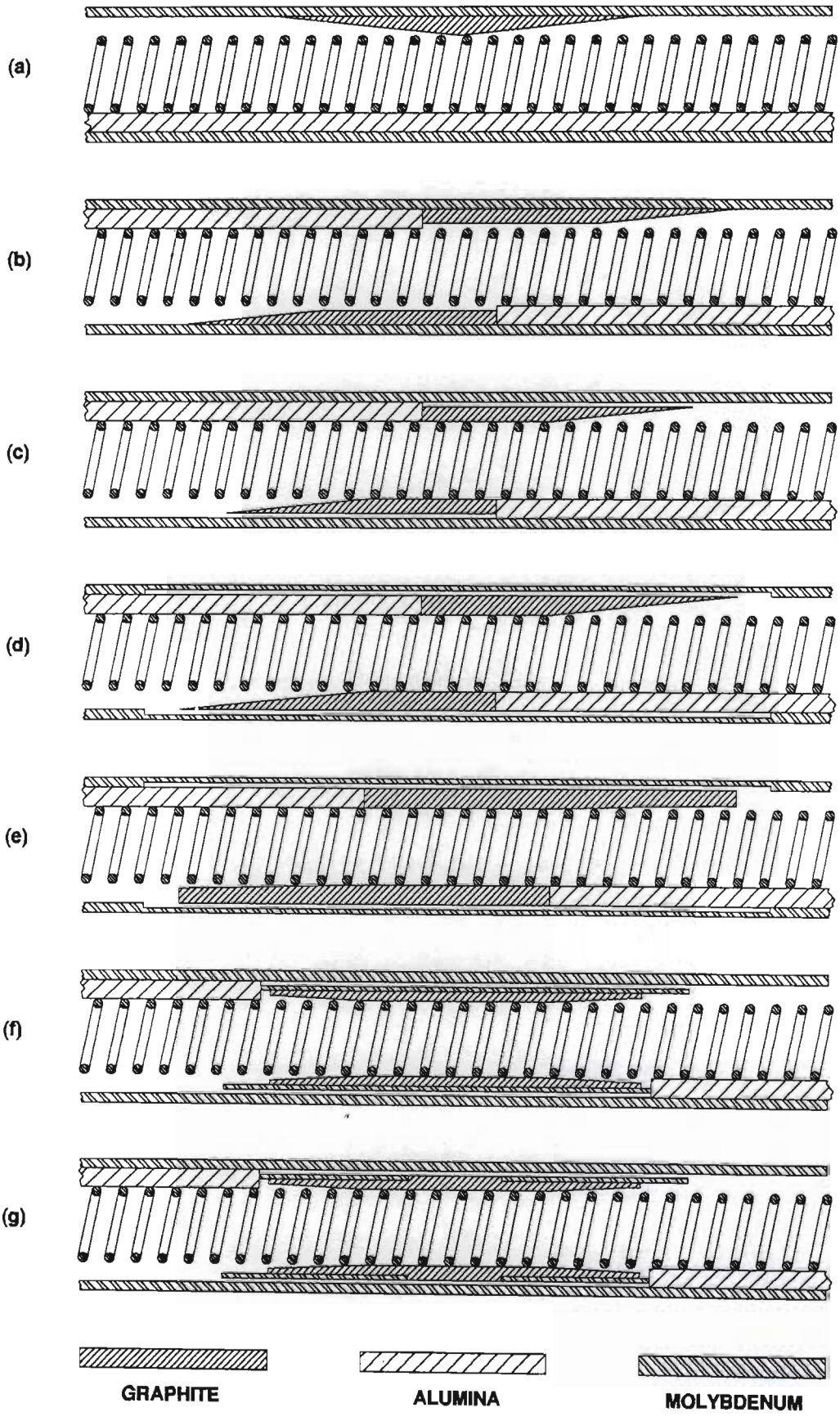

Figure 3.5 Series of Attenuator Geometries

A graphite attenuator with the geometry of Figure 3.5 (b) is shown on a coin in Figure 3.6 and together with other TWT components in Figure 6.2. This 30 mm long attenuator had an outer diameter of 6 mm and a wall thickness of 0.9 mm in its middle. The wall was tapered linearly down to approximately 0.2 mm at each end. One such end is shown in Figure 3.7. A taper length of 10 mm, corresponding to just over one wavelength of a 4 GHz helix wave, was chosen. This was because 4 GHz was at the lower end of the TWT test frequency range and the minimum length of an impedance transformer should be one wavelength long for broadband matching [18].

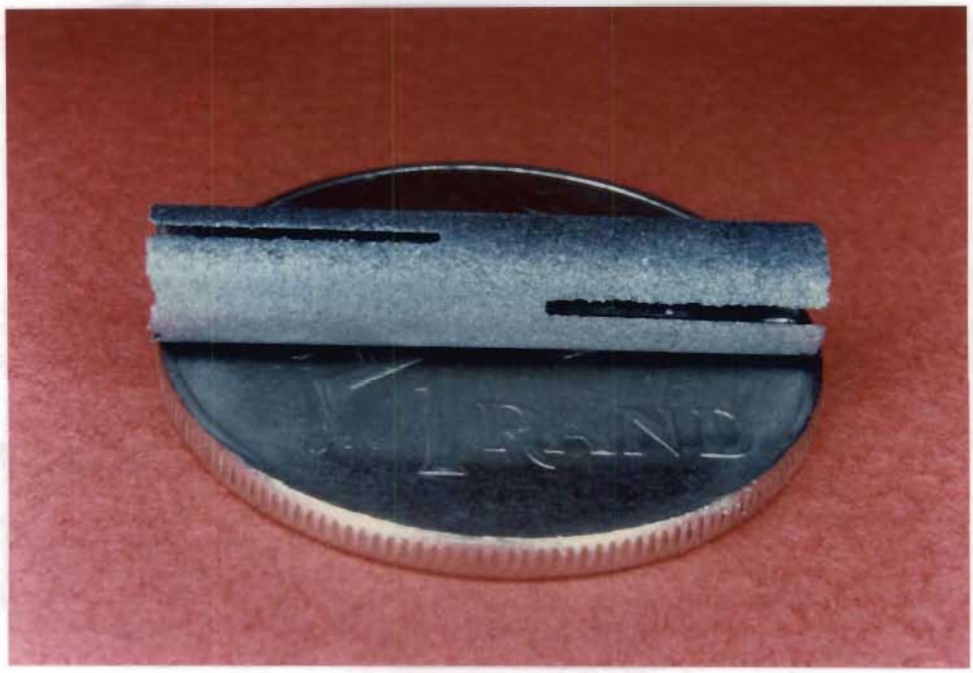

Figure 3.6 Graphite Attenuator with Geometry of Figure 3.5 (b)

The attenuators that were made to the geometries of Figures 3.5 (b) to (d) were machined from Ringsdorff's EK432 electrographite which produced excessive amounts of gas when heated in a vacuum. Subsequent attenuators were therefore made from reactor-grade graphite. This purer but softer graphite was too weak to be tapered down to 0.2 mm and the reactor-grade graphite attenuators were therefore made to the geometry of Figure 3.5 (e), with a minimum wall thickness of 0.8 mm. One end of such an attenuator is shown in Figure 3.8.

Due to the fragility of their thin graphite sections, most of the attenuators were found to be broken after the 950°C, final TWT vacuum braze. A more robust structure was therefore sought.

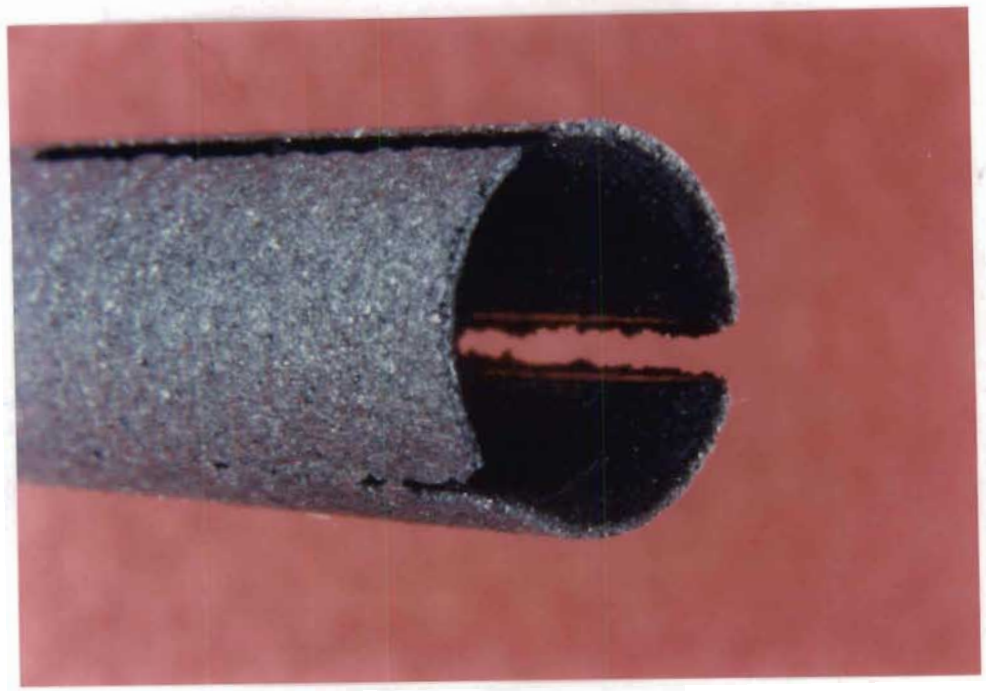

Figure 3.7 End View of Graphite Attenuator with Geometry of Figure 3.5 (b)

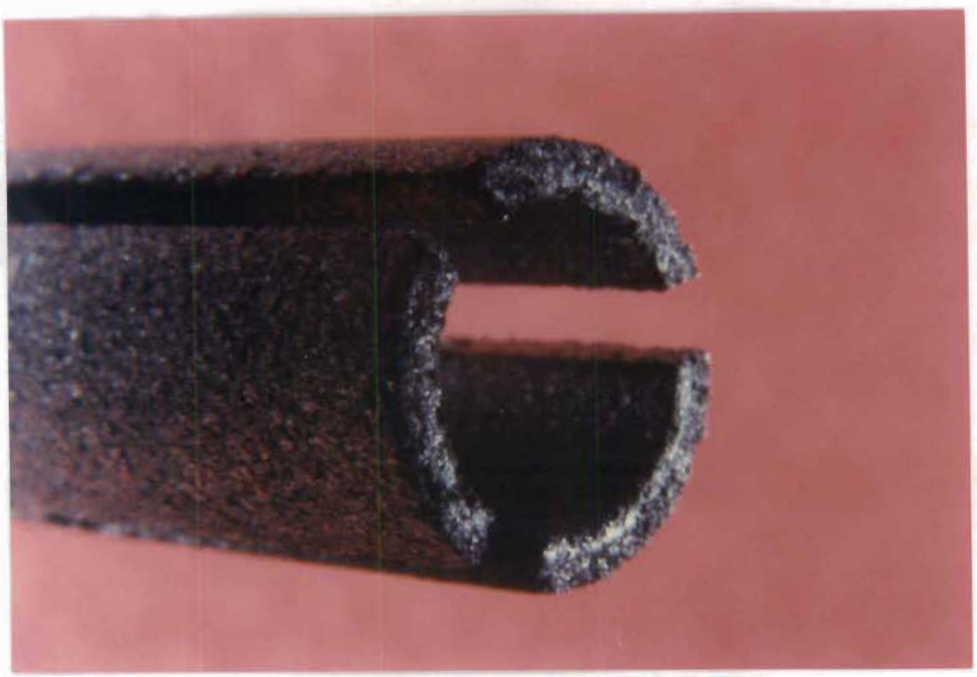

Figure 3.8 End View of Graphite Attenuator with Geometry of Figure 3.5 (e)

Graphite reacts with both molybdenum and tungsten when in direct contact for a few minutes at 1500°C [8]. Attempts were therefore made to coat the inside of a molybdenum tube with "Aquadag" and then to fire the coat on using an induction generator. The graphite flaked off before the reaction temperature was reached and did not adhere to the molybdenum. In a different approach, a graphite rod was fitted into a

molybdenum sleeve and both were heated in a horizontal position. The expansion coefficient of molybdenum was higher than that of the graphite used and the graphite therefore adhered only to the side of the tube that it was resting on. Upon cooling, the differential contraction of the fused pieces deformed the molybdenum tube giving it a slightly egg-shaped cross section. It was realised that the structure would be more useful if not heated and it was found that a graphite rod could be successfully machined when held only by the tightness of its fit inside a molybdenum tube. This method was used to produce the reinforced graphite attenuators shown in cross section in Figures 3.5 (f) and (g) and from one end in Figure 3.9. These reinforced attenuators were strong enough to survive both rough handling and the brazing cycle.

Figure 3.9 End View of Reinforced Graphite Attenuators with Geometry of Figure 3.5 (f)

The geometries of Figures 3.5 (b) and (c) resulted in a DC path from the helix to the helix sheath through graphite that was deposited onto the alumina helix support rods during TWT assembly. This problem was solved in the geometries of Figures 3.5 (d) and (e) by boring out the helix sheath in the vicinity of the attenuators and in the geometries of Figures 3.5 (f) and (g) by stopping the rods short of the graphite.

3.3.2 Results

The matching and attenuation of each attenuator were measured in both the frequency and the time domain using an HP8510B vector network analyzer (described in Appendix B). Selected data from these measurements are presented in Figures 3.10 (a) to (f).

The geometry of Figure 3.5 (b) provided a good match, shown by the low reflection coefficient in the 3 to 5 ns region of Figure 3.10 (a). The geometries of Figures 3.5 (c) to (g), however, provided poor matches. A typical measurement is shown in Figure 3.10 (b). Here the large reflection from the attenuator was detected between 3 and 4 ns after that from the TWT output transition at 0 ns. Calculations were made to determine the attenuator's effect on the helix characteristic impedance of the helix [19] [20]. The tapers of attenuators with the geometry of Figure 3.5 (b) gradually transformed the helix characteristic impedance to a lower value inside the attenuator. This resulted in a good match but the attenuation, shown in Figure 3.10 (c), was poor. This was due to the resistivity of the graphite not being high enough. Reducing the gap between helix and graphite increased the attenuation but to achieve sufficient attenuation, the length of the attenuator needed to be impractically long and the gap to be impractically small.

In the geometries of Figures 3.5 (c) to (g) the shorting of the helix turns by intimate contact with the relatively low resistivity graphite resulted in a reactive transmission characteristic impedance over a 10 mm section of what can be described as a cylindrical waveguide operating beyond cutoff. This leads to the good attenuation characteristics of Figure 3.10 (d) and the poor matching characteristics of Figure 3.10 (b). The transmission peak at 4,3 GHz in Figure 3.10 (d) is due to half wave resonance of the coaxial transmission section formed by the attenuator body and the helix sheath. This peak, together with its harmonic, was increased, as shown in Figure 3.10 (e), by the higher conductivity of the molybdenum reinforcing sleeves of attenuators with the geometry shown in Figure 3.5 (f). The geometry of Figure 3.5 (g) was designed to reduce these peaks and resulted in the 10 dB improvement shown in Figure 3.10 (f) where the 5.5 Ghz peak is related to the whole attenuator length and the 14.6 GHz peak is related to the length of each of the two 10 mm molybdenum tube sections.

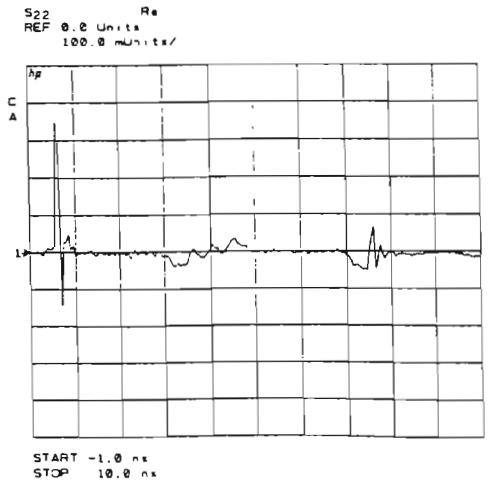

(a) Match of Geometry of Figure 3.5 (b)

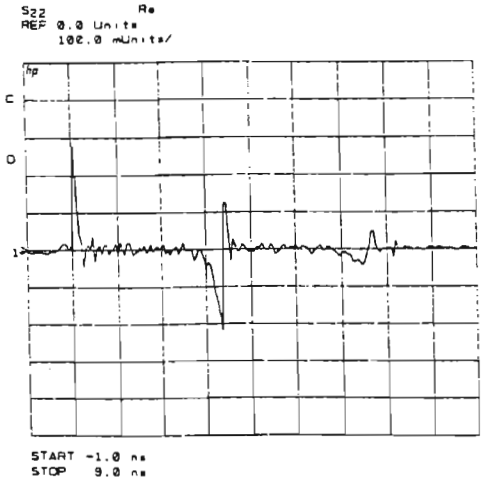

(b) Match of Geometry of Figure 3.5 (d)

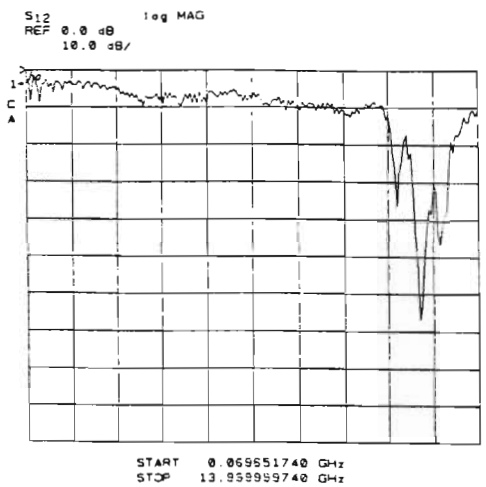

(c) Loss of Geometry of Figure 3.5 (b)

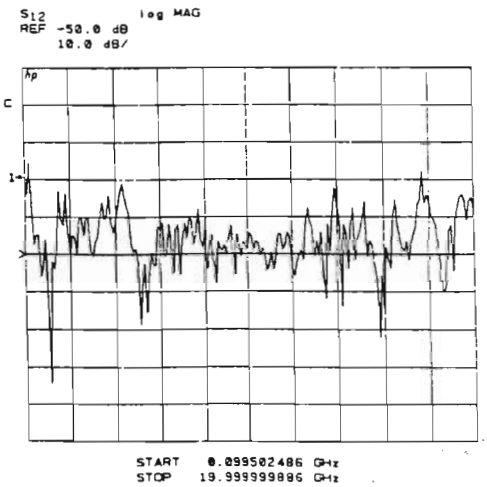

(d) Loss of Geometry of Figure 3.5 (d)

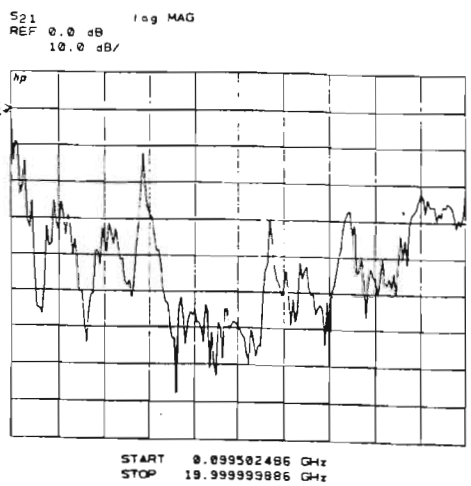

(e) Loss of Geometry of Figure 3.5 (f)

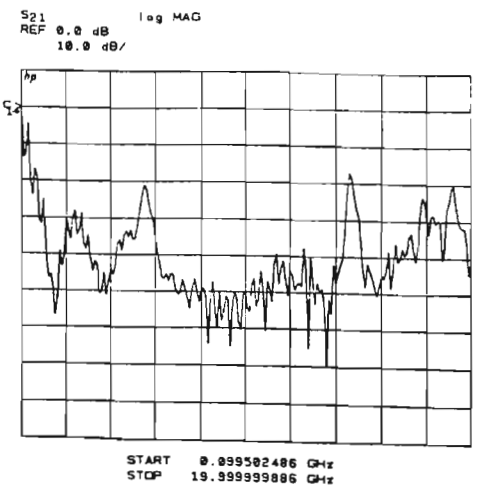

(f) Loss of Geometry of Figure 3.5 (g)

Figure 3.10 Transmission and Matching Characteristics of Graphite Attenuators

3.3.3 Conclusions

The practicality of using a solid-graphite attenuator in an experimental TWT was investigated. The conductivity of the reactor-grade graphite available was found to be too high for the chosen geometries to provide sufficiently reliable matching or attenuation without making the attenuator too long or subject to too tight a set of tolerance specifications. The results measured for the best attenuator were not easily repeatable due to the inadequate mechanical strength of the graphite and the fine tolerances required. The use of other grades of graphite, or of graphite containing compositions, having greater resistivity may have helped to reduce the severity of these problems but this was not investigated due to these compositions not being readily available.

3.4 MOLYBDENUM FILM ATTENUATOR

3.4.1 Geometry and Manufacture

The molybdenum film attenuators were of the typical design depicted in Figure 3.3 and described in Section 3.2.2. Manufacture of the molybdenum films was by vapour deposition using the Materials Science Laboratory's electron beam (EB) welder.

The vapour deposition process was developed by trial and error and is best described with the aid of Figure 3.11. A 10 mm diameter molybdenum pellet, heated at one spot by a 50 kV electron beam, was the vapour source. This pellet was placed in a 10 mm deep hole that had been drilled into a copper block of approximately thirty times the pellet's heat capacity. A mask was used to limit the length of the attenuator films and also to reduce the amount of molybdenum vapour that was deposited on the walls of the EB welder's work chamber.

Before being coated, the alumina rods were ultrasonically cleaned. The cleaning solvent was changed four times, alternating between deionised water and acetone. Each clean rod was then held in a small, clean chuck that was rotated by the EB welder's larger, three-jaw chuck. The rods were positioned at a height of about 28 mm above the plane of the top of the pellet and at a distance of 20 mm away from the electron beam.

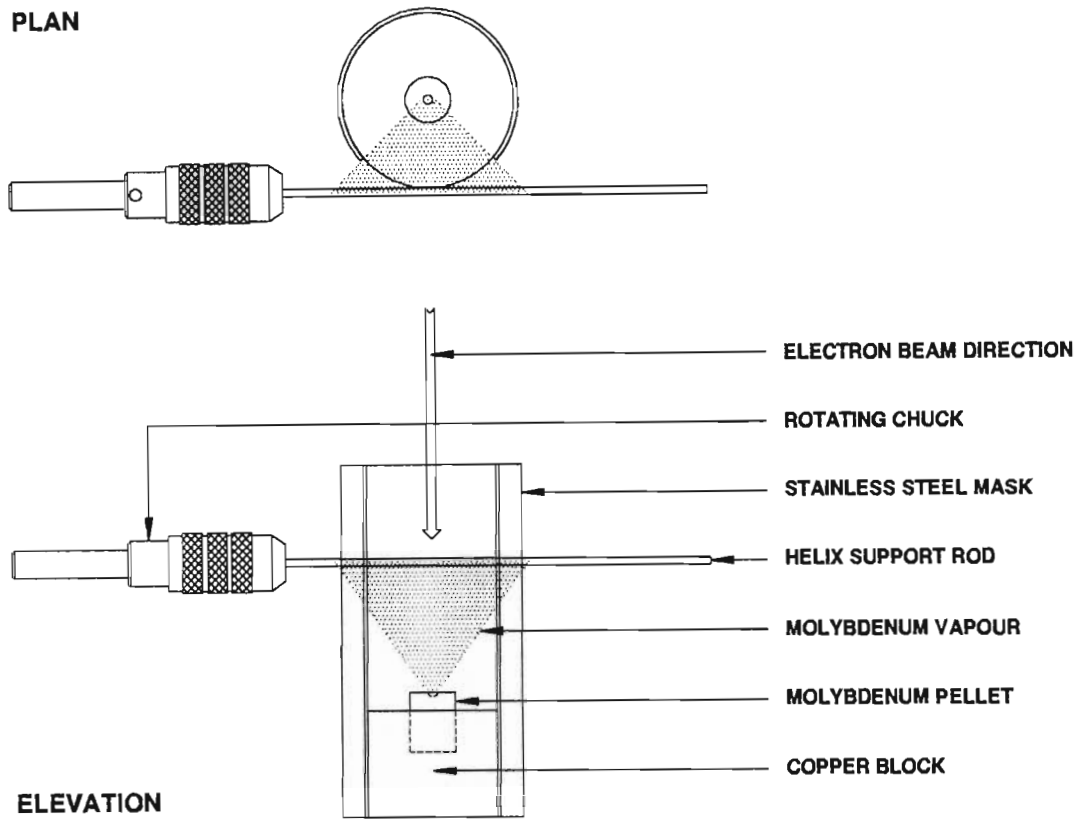

Figure 3.11 Helix Rod Coating Setup

The maximum available chuck speed of 45 rpm was used to ensure that the films were more evenly deposited around the rods. The highest speed was necessary because the coating times were short when compared to the revolution time of the chuck. Also, the molybdenum vapour concentration was not constant, but increased as a pellet heated up. Relatively long beam pulses of 30 seconds were therefore used to avoid the uneven film thicknesses due to shorter, say five second, pulses. Relatively even coatings were achieved with 30 second bursts of a 15 to 21 mA, 50 kV beam. Results were repeatable only if each end of a pellet was used just once because a hole, approximately 2 mm deep and wide, was evaporated into a pellet with each beam pulse.

3.4.2 Results

Initial experiments were made with rods that had not been cleaned and when the EB welder vacuum plant was faulty. Evaporated molybdenum atoms were oxidised both while passing through the poor vacuum of 5×10^{-2} torr and when landing on the unclean

rods. The coatings were therefore black in colour and easily rubbed off with a finger.

The vacuum plant was subsequently repaired and a liquid nitrogen cold trap was made and fitted into the EB welder's work chamber. Pressures of less than 10^{-6} torr could then be reached but coatings were made at pressures of less than 10^{-4} torr to reduce pumping times. This pressure resulted in an estimated mean free path [21] that was more than eleven times longer than the maximum of 41 mm that molybdenum atoms were required to travel. Molybdenum films made on clean rods at these reduced pressures were silver-grey in colour, as shown in Figure 3.12. The films were strongly adherent but heavy coatings (with resistances of less than 20 Ω between two points, 2 mm apart) were removed by ultrasonic agitation in deionised water.

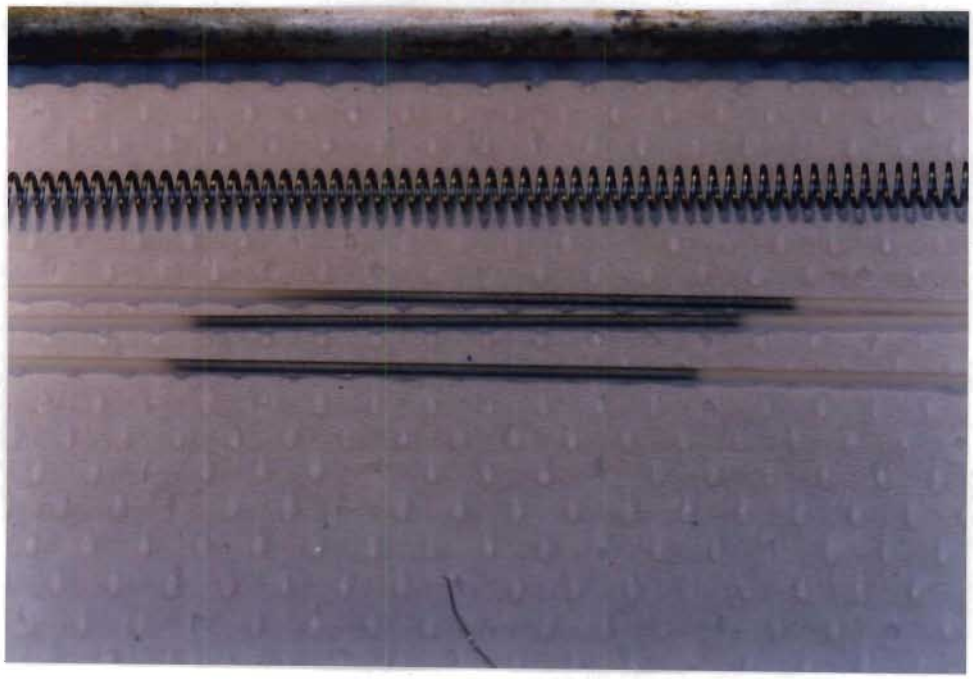

Figure 3.12 Middle section of the Helix and Molybdenum-Film-Coated Helix Support Rods of TWT LP8

The thickness of a film is proportional to its DC resistivity which is a function of the resistance between two points. A simple probe, consisting of two stainless steel needles, supported 2 mm apart, was made for the resistance measurements that were needed to compare different coatings and to assess taper gradients. Measurements were made between points on lines parallel to the rod axis and are here called two-point resistance measurements.

The variation of two-point resistance with axial distance for three typical films made with

18 mA, 50 kV pulses of 30 second duration is shown in Figure 3.13. Positioning the rods close enough to the source for the ends of the attenuator to be in a region of significantly lower vapour density than the middle section resulted in gradual film thickness tapering and a special, taper-making mask was not required. Films made using the same beam parameters varied slightly. The differences between films were due to small variations in the rod, mask and pellet positions, the beam focusing and the vacuum pressure.

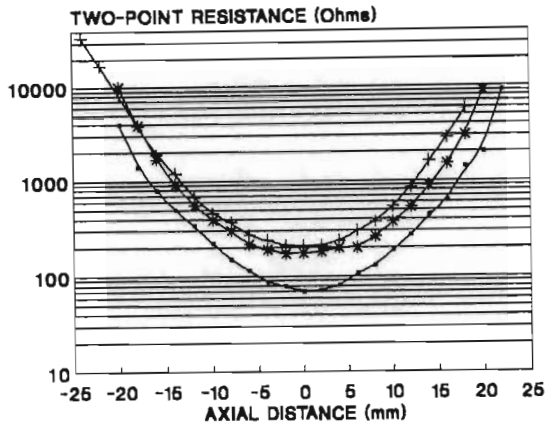

Figure 3.13 Two-Point Resistance versus Axial Distance for Three Films Made with 18 mA, 50 kV Pulses of 30 Second Duration

In addition to DC measurements, RF measurements were also needed since, as mentioned in Section 3.2.2, there is little correlation between RF loss and DC resistivity. These measurements had to be made quickly because they were part of a trial and error iteration. A test jig was therefore made to measure the RF characteristics of any three coated rods.

The jig was not required to be evacuated and it differed from TWT RF structures in that instead of using vacuum envelope transitions to the helix, the helix ends were soldered directly onto the centre conductors of semi-rigid coaxial cables. Flow of solder onto the tungsten helix was made possible by resistance welding some nickel onto the helix, and then filing the bulk of it off, before soldering. The cable outer conductors were soldered into short brass tubes that were then inserted into a molybdenum helix sheath. The sheath was designed to slide over the rest of the structure, exposing the three helix support rods and allowing them to be replaced in a few minutes.

As in the graphite attenuator case, measurements were made in both the time and the frequency domain but, to save time and because only relative amplitudes were needed, the HP8510B vector network analyzer was not calibrated (see Appendix B). Due to the

roll-off of the network analyzer test set at low frequencies, not calibrating resulted in distortion of the time domain impulses. This distortion was however not severe, since an electrical delay was used to position the reference plane of the measurements at the ends of the test jig helix.

The uncalibrated matching and transmission characteristics of the test jig, fitted with uncoated helix support rods, are shown in Figures 3.14 (a) and (b) respectively. The two reflections due to the ends of the 2 mm inner diameter helix can be seen at 0 ns and around 7.4 ns. Replacing the control rods with rods coated by films of 50, 46 and 39 Ω minimum two-point resistances resulted in the characteristics of Figures 3.14 (c) and (d). Comparison of the two pairs of figures shows that the films have reduced the transmission through the test structure by about 50 dB, without causing noticeable reflections off themselves.

The first operational TWT (TWT LP8) employed a helix, made from 0.5 mm tungsten wire, wound to a pitch of 1.4 mm and an inner diameter of 3 mm. This helix was supported in a molybdenum helix sheath of 6 mm inner diameter by three 1 mm diameter alumina rods. The sheath had been bored out slightly in the vicinity of the 45 mm long attenuator to eliminate any DC path through the attenuator from the helix to the sheath (see Section 3.2.3).

Using films of 100, 85 and 70 Ω minimum two-point resistance for the attenuator of TWT LP8 resulted in the good matching of Figure 3.15 (a) but in the poor attenuation of Figure 3.15 (b). This attenuation was about 7 dB less than what was measured for the lighter films of Figure 3.13 (with 210, 175 and 70 Ω minimum two-point resistances). Since test jig measurements had shown increased attenuation to result from heavier molybdenum films, the attenuation of TWT LP8 was expected to be higher than measured. One explanation for the low attenuation is that the optimum film conductivity for the geometry used had been exceeded, resulting in reduced losses. Another is that the films were significantly eroded by oxidation and evaporation during TWT processing.

Molybdenum forms thin surface oxide films of MoO_2 and MoO_3 if exposed to water vapour even at low temperatures [22]. These oxides rapidly evaporate in a vacuum at temperatures above 500°C. Some oxidation of the attenuator films of TWT LP8 would have occurred because they were left in humid, coastal air for five days after they were

made. The erosion of the films was probably accelerated due to them being vacuum furnace heated to 950°C three times in these five days (once when TWT LP8 was brazed together and twice more during repairs). Similar films, made at the same time as TWT LP8 and then left in air, were observed to change from a silver-grey colour to blue-black in a few months. In this time, lighter films oxidised and evaporated almost completely away. Vacuum storage of molybdenum film coated rods was subsequently used to prevent this.

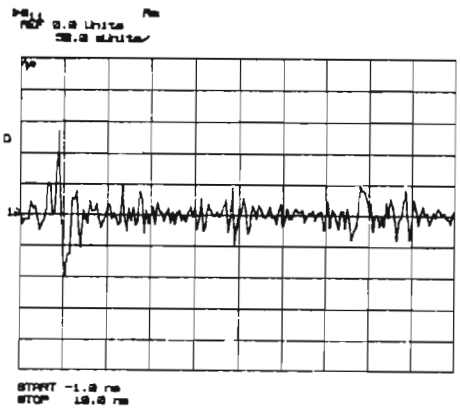

(a) Match Using Uncoated Rods

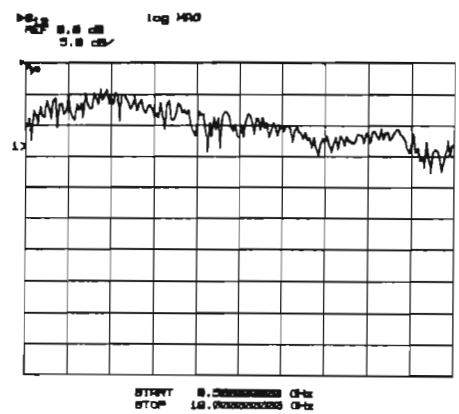

(b) Loss Using Uncoated Rods

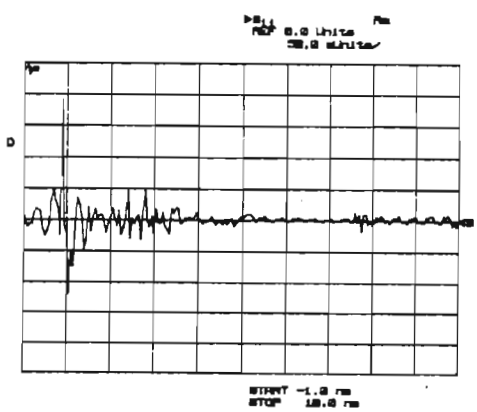

(c) Match of Coated Rods

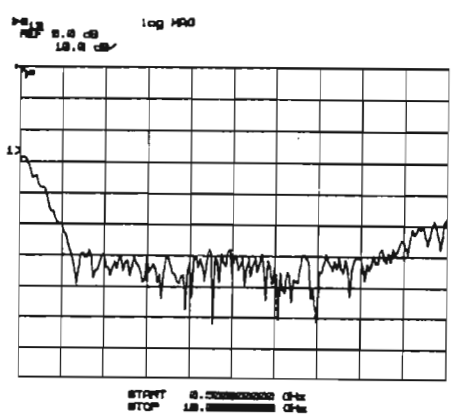

(d) Loss Using Coated Rods

Figure 3.14 Matching and Transmission Characteristics Using Test Jig

Results for the attenuator of the second operational TWT (TWT LP10) are shown in Figure 3.15 (c) and (d). The main differences between this TWT and TWT LP8 were that its helix inner diameter and pitch had been reduced to 2 and 1.0 mm respectively and

that its helix support rod diameter had therefore been increased to 1.5 mm. The reflections due to the attenuator can be seen between 3 and 4 ns after the much larger reflection due to the TWT's input port. Better matching had been measured for films with similar minimum two-point resistances in the attenuator test jig. Furthermore, the approximately 30 dB attenuation shown in Figure 3.15 (d) was significantly lower than the 60 dB loss of similar films that had not been subjected to the 950°C TWT vacuum braze.

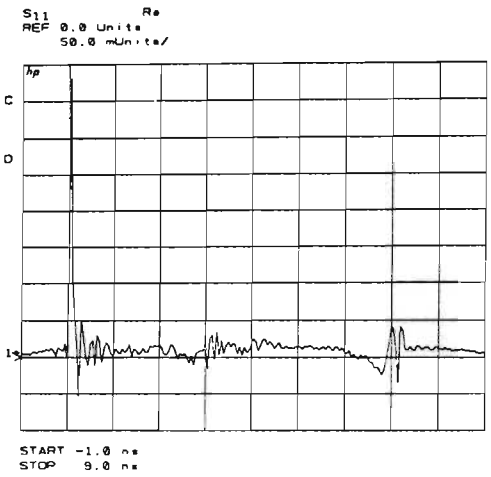

(a) Match of TWT LP8

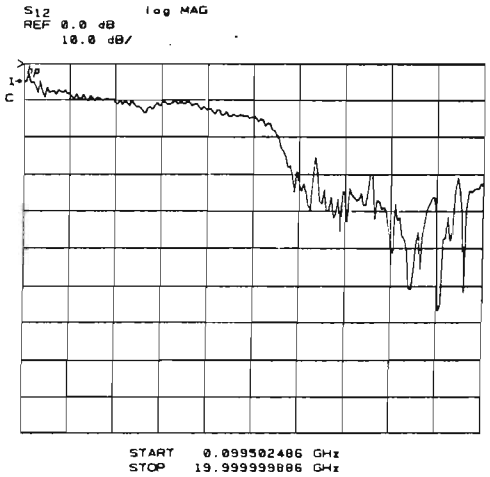

(b) Loss Through TWT LP8

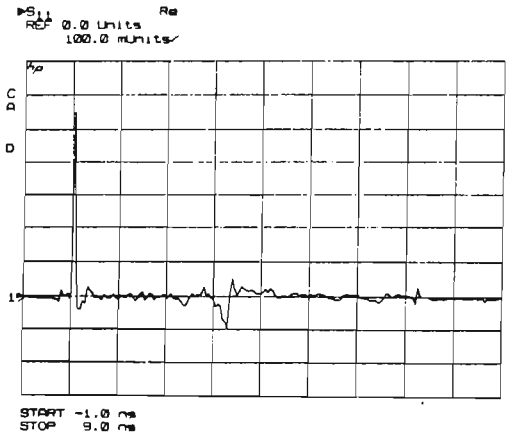

(c) Match of TWT LP10

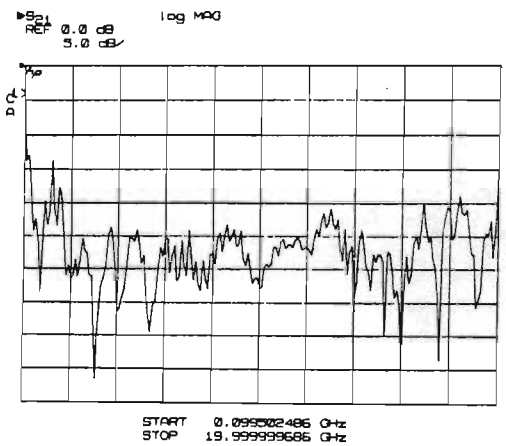

(d) Loss Through TWT LP10

Figure 3.15 Matching and Transmission Characteristics of Molybdenum Film Attenuators

To determine the effects of the TWT processing conditions, three rods with films of 39, 25 and 22 Ω minimum two-point resistances were heated to 950°C inside a molybdenum tube in the vacuum furnace. Heating the rods caused the minimum two-point resistance

of all three films to drop to about 3 Ω. The reason for this was not investigated due to time constraints, the high cost and diminishing supply of alumina rods, and the running costs of the electron beam welder and the vacuum furnace. Recrystallisation of the films was suspected, but was unlikely since this takes two days at 950°C for molybdenum [22]. Another possible reason may have been the evaporation of the few oxides formed during manufacture.

Attenuation was reduced after films had been heated because the film conductivity that resulted in maximum loss had been exceeded. This was concluded after comparing the approximately 30 dB loss measured for the 40, 27 and 23 Ω minimum two-point resistance films of TWT LP10 with the approximately 45 dB loss due to lower conductivity 50, 46 and 39 Ω minimum two-point resistance rods of another, similar, vacuum-brazed structure. In addition to the reduced attenuation that resulted, the impedance matching was worsened by the more reactive films that were less effectively tapered.

By accounting for masking (discussed in Appendix B) by the input port reflection, the impedance matches of the attenuators of TWTs LP8 and LP10 were estimated as 28 and 17 dB from Figures 3.15 (a) and (c) respectively. Their respective losses were measured as 10 and 25 to 30 dB in the 4 to 8 GHz range.

After TWT LP10 was outgassed in a vacuum at 400°C and mounted on the vacuum pump, a measurement of the loss through the tube was made using the RF test circuit (see Section 8.3 of Chapter 8). The measured loss was approximately 15 dB, significantly lower than the 25 to 30 dB measured before outgassing.

TWT LP8 was not outgassed in the vacuum furnace before being mounted on the vacuum pump and RF test circuit measurements of its loss revealed no attenuation decay. Nor did a network analyzer measurement made one year after the measurement of Figure 3.15 (b).

The change in the attenuator of TWT LP10 was therefore attributed to the sensitivity of its molybdenum films to temperature and atmosphere during tube processing. It is recommended that either more consistent processing or more stable films are used in future work with thin film attenuators. Tantalum/aluminium sputtered films with a Ta/Al

ratio of 70/30 atomic per cent are highly stable and a suggested alternative to molybdenum films [23].

The 10 and 15 dB losses due to the attenuators of TWTs LP8 and LP10 were not sufficient to ensure TWT stability. This is discussed further in Chapter 8.

3.4.3 Conclusions

A method for coating the alumina helix support rods of a TWT with metal films has been developed by trial and error. A molybdenum pellet, heated by the electron beam of an electron beam welder, can be used as a molybdenum vapour source. If the vacuum pressure is low enough to prevent oxidation of the atomically clean surfaces, good adhesion of the molybdenum onto the alumina is easily achieved. The films are however not stable in air or when heated after being exposed to air.

Good matching and attenuation were achieved if the conductivity of the films was correct but this was not achieved for a brazed TWT structure because of the sensitivity of the films to processing conditions. Further work is therefore necessary to determine the film thickness and processing conditions that are required for optimum attenuation and matching.

REFERENCES

[1] J.F. Gittins, *Power Travelling-Wave Tubes*, The English Universities Press Ltd, Chapter 7, 1965.

[2] C.K. Birdsall and C.C. Johnson, "Travelling-Wave Tube Efficiency Degradation Due to Power Absorbed in an Attenuator", *IRE Transactions on Electron devices*, Vol. ED-6, pp. 6 to 9, January 1959.

[3] J.R. Pierce, *Traveling-Wave Tubes*, D. Van Nostrand Company, Inc., p. 140, 1950.

[4] J.S. Cook, R. Kompfner and H. Suhl, "Nonreciprocal Loss in Travelling-Wave Tubes Using Ferrite Attenuators", *Proceedings of the IRE*, Vol. 42, pp. 1188 to 1189, July 1954.

[5] D.J. Connolly, "Use of a Simple External Nonreciprocal Attenuator in Coupled-Cavity TWT's", *IEEE Transactions on Electron devices*, Vol. ED-24, No. 12, pp. 1351 to 1353, December 1977.

[6] Reference [1], pp. 237 to 240.

[7] J.P. Calame and W.G. Lawson, "A Modified Method for Producing Carbon-Loaded Vacuum-Compatible Microwave Absorbers from a Porous Ceramic", *IEEE Transactions on Electron devices*, Vol. 38, No. 6, pp. 1538 to 1543, June 1991.

[8] W. Espe, *Materials of High Vacuum Technology*, Vol. 1, Pergamon Press, pp. 623 to 660, 1966.

[9] Reference [1], p. 184.

[10] A.H. Iverson, "Precision Helix Winding and a Mechanism of Loss Variation", *IRE Transactions on Electron devices*, Vol. ED-3, pp. 205 to 206, October 1956.

[11] P.K. Jain and B.N. Basu, "A Theory of the Attenuator-Coated Helical Slow-Wave Structure of a Traveling-Wave Tube", *IEEE Transactions on Electron devices*, Vol. 35, No. 10, pp. 1750 to 1757, October 1988.

[12] Reference [3], pp. 47 to 48.

[13] Reference [1], p. 212.

[14] C.G. Reynolds, *The Analysis, Simulation and Testing of an Experimental Travelling-Wave Tube*, Ph.D. Thesis, Department of Electronic Engineering, University of Natal, 1994.

[15] B.C. Dann, *Microwave Terminations*, Final Year Thesis, Department of Electronic Engineering, University of Natal, 1987.

[16] E.W. Schumann, A.W. Stokes, D.M. Smith and H.L. Nattrass, "Development of an Experimental Travelling Wave Tube", *Proceedings of the Symposium on Antennas and Propagation and Microwave Theory and Techniques*, Somerset West, South Africa, pp. 157 to 164, August 1990.

[17] N. Vassilopoulos and H.L. Nattrass, "Further Developments in Travelling Wave Tube Design", *Proceedings of the Symposium on Antennas and Propagation and Microwave Theory and Techniques*, Durban, South Africa, pp. 171 to 178, September 1992.

[18] Personal consultation with Dr. H.C. Reader.

[19] B.N. Basu, "Equivalent Circuit Analysis of a Dielectric-Supported Helix in a Metal Shell", *Int. J. Electronics*, Vol. 47, No. 3, pp. 311 to 314, 1979.

[20] P.K. Jain, K.V.R. Murty, S.N. Joshi and B.N. Basu, "Effect of the Finite Thickness of the Helix Wire on the Characteristics of the Helical Slow-Wave Structure of a Traveling-Wave Tube", *IEEE Transactions on Electron devices*, Vol. ED-34, No. 5, pp. 1209 to 1213, May 1987.

[21] R.V. Stuart, *Vacuum Technology, Thin Films, and Sputtering*, Academic Press, Inc., pp. 9 to 22, 1983.

[22] Reference [8], pp. 77 to 118.

[23] J.F. Balicki, E.F. Cook, R.C. Heidt and V.E. Rutter, " The AR6A Single-Sideband Microwave Radio System: The Travelling-Wave-Tube Amplifier", *The Bell System Technical Journal*, Vol. 62, No. 5, pp. 3429 to 3445, December 1983.

CHAPTER 4

PPM FOCUSING SYSTEM

4.1 INTRODUCTION

A periodic permanent magnet (PPM) stack was designed, built and used for electron beam focusing of the low profile TWTs. This stack was adapted from the more simple, experimental PPM stack of Stokes [1]. Changes to his design were necessary to accommodate RF, mounting and support structures and to satisfy different focusing requirements. Since magnetic focusing theory and design are described in detail in Stokes' thesis, this chapter begins with only a brief coverage of these topics. Details of the design and manufacture of the PPM stack are presented in the next section. Then follows an account of the PPM stack magnetization procedure that was developed to determine the field strength required of the stack's individual magnets so that the magnetization profile of the assembled stack could be controlled. The chapter closes after beam focusing results have been discussed and conclusions have been made.

The unit of field strength used here is the gauss because it is more commonly used in the literature than the SI unit, the tesla (1 G = 10^{-4} T).

4.2 PPM FOCUSING

4.2.1 PPM Focusing Basics

An electron beam will diverge due to space charge [2] unless it is somehow confined. This beam focusing, as the confinement is commonly termed, can be achieved by electrostatic or magnetic fields. In this section, only the principles of magnetic focusing are discussed (electrostatic focusing [2], [3], [4], [5] is not discussed since it is not used in single helix TWTs). The review is brief but references to sources of more detailed coverage are made frequently.

Two types of beams are mentioned in the following paragraphs: ideal and real beams. Ideal beams are here defined as beams of constant current density and electron velocity in which all the electrons travel parallel to the beam axis. Real beams, on the other

hand, are non-ideal.

A uniform axial magnetic field, produced by a permanent magnet or a solenoid, can be used to focus a linear electron beam [4]. The field strength required for confinement is a function of the beam current density and velocity and the dynamics are such that the beams are scalloped [3]. The space charge forces of a particular ideal electron beam can be balanced almost exactly if it suddenly enters an axial magnetic field of a corresponding strength, the Brillouin field [6]. Optimum focusing, with minimum beam scalloping, is possible with such a field.

Periodic field focusing, with a series of magnetic electron lenses, is an alternative to uniform field focusing [4]. A single magnetic electron lens is illustrated in Figure 4.1. An electron beam will converge when passed through such a lens. Each lens in a series can cause a beam to converge by the same amount that it diverged, due to space charge, since the previous lens. This is portrayed in Figure 4.2. Both positive and negative fields can be used since the convergent force on an electron beam is a function of the square of the magnetic field in which it is immersed [4]. Focusing is therefore possible using the alternating magnetic field of a stack of permanent magnets in which the magnets are assembled with like poles on adjacent faces. Such a stack results in an axial field that varies periodically with axial position and is called a periodic permanent magnet (PPM) stack.

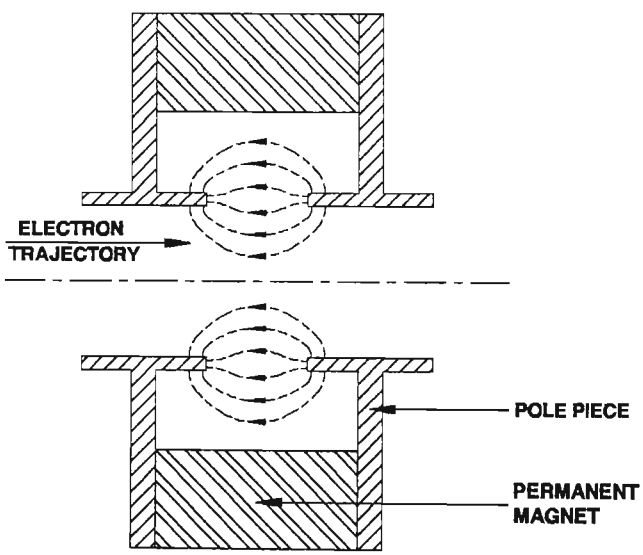

Figure 4.1 A Magnetic Electron Lens

(After J.W. Gewartowski and H.A. Watson, *Principles of Electron Tubes*, D. Van Nostrand Company, Inc., 1965.)

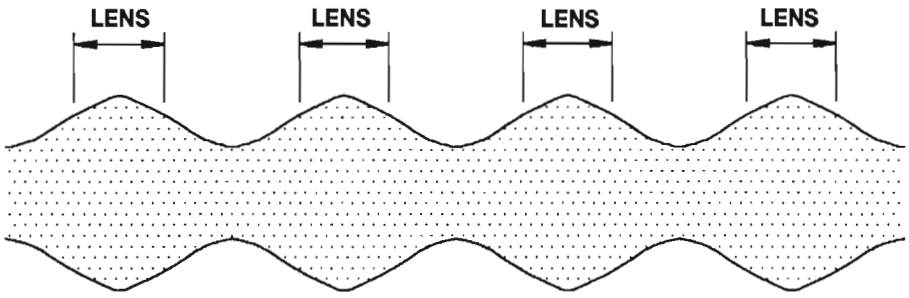

Figure 4.2 The Focusing Action of a Series of Equally Spaced Lenses

(After J.W. Gewartowski and H.A. Watson, *Principles of Electron Tubes*, D. Van Nostrand Company, Inc., 1965.)

Periodic focusing systems have been shown to be approximately equivalent to uniform field systems if the rms value of a PPM stack's field is equal to the uniform field it is replacing [7]. The main advantage of periodic focusing is that a PPM stack of N lenses is between N and N^2 times lighter than its uniform field equivalent. For example, Mendel *et al* reported that a certain uniform field permanent magnet, which produced an axial field of 450 G over a length of 9 inches (230 mm), weighed 38 pounds (17 kg) but that the equivalent periodic magnet stack weighed only 1 pound and 5 ounces (0.6 kg) [8]. Less magnetic material is required to produce a particular periodic axial field because PPM structures have lower external leakage fields than permanent magnet uniform field structures. Leakage free structures can also be made, resulting in further weight reductions, but these are costly [9], [10]. Where a solenoid is being replaced, a power saving advantage is added to the PPM stack's weight saving advantage.

4.2.2 Field Entrance Conditions

For minimum beam ripple to be achieved, certain conditions have to be met where a beam enters a magnetic focusing field. The beam is required to be ideal and this is best approximated at the beam minimum of a well designed convergent gun. The introduction of a Brillouin field over a short axial distance at the beam minimum will balance any space charge forces, thus maintaining the beam radius at its entry value.

Since a step change in flux is impossible in a PPM stack, ideal, cosinusoidal entrant conditions are not achievable. Practical fields look more sinusoidal than cosinusoidal but

Rawls *et al* have shown that an entrant field is equivalent to an ideal field if both fields have the same rms value [11]. True states that optimum results are obtained if the period of the first peak is equal to that of the rest of the stack and if its peak field is equal to the rms field of the rest of the stack [12]. Such a field, depicted in Figure 4.3, satisfies the condition of Rawls *et al* if it is assumed that the field shape is sinusoidal (other shapes can be used for focusing [13]). True suggests that the beam minimum should then be positioned at the point where the field has risen to $1/\sqrt{2}$ times the first peak. This practically determined beam minimum position is not the same as that suggested by Rawls *et al*.

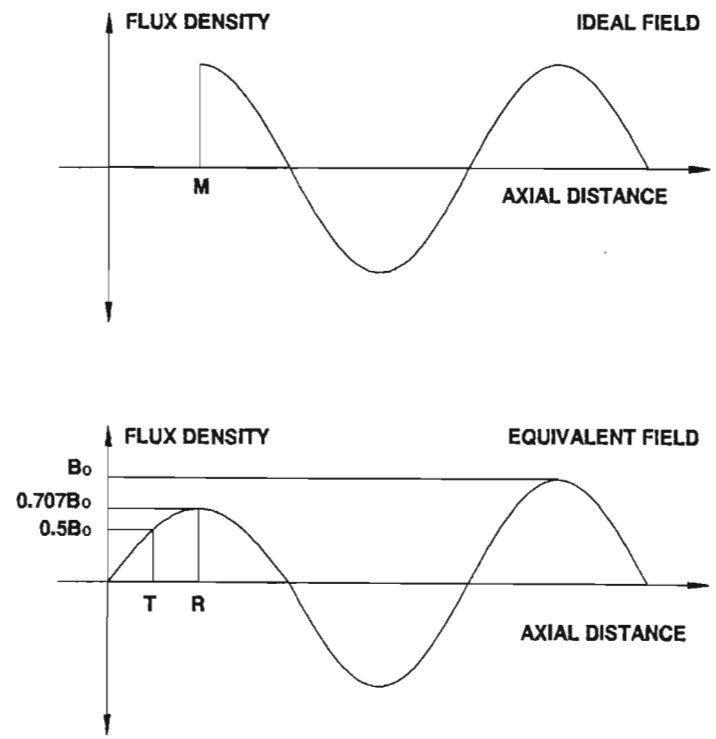

Figure 4.3 Ideal and Equivalent Entrance Fields and Suggested Beam Minimum Position (M is Ideal Position, T is Due to True [12] and R is Due to Rawls *et al* [11])

If a beam enters a field with a radius that is smaller than optimum, it will not be sufficiently confined and larger than minimum ripple will result. On the other hand, beams that are too wide will be overfocused and scalloping will also occur. This is demonstrated in Figure 4.4 in which simulated beams (see Appendix C) of different radius have entered the same field.

If a beam with nonzero radial velocity enters a Brillouin field it will also be scalloped more than an ideal beam. Figure 4.5 shows the simulated effect of initially converging

and diverging beams entering a field.

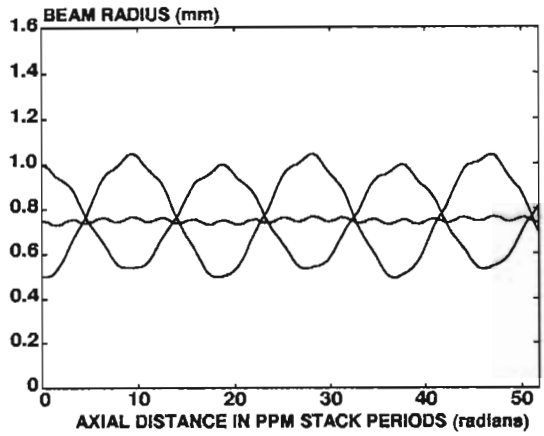

Figure 4.4 Simulated Scalloping Due to Beams of Small, Large and Correct Diameter Entering a Brillouin Stack

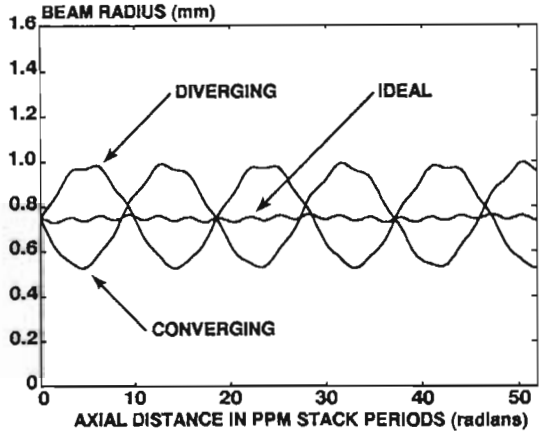

Figure 4.5 Simulated Scalloping Due to Converging, Diverging and Ideal Beams Entering a Brillouin Stack (Radial Velocities are 0.1 Times Axial Velocity)

4.2.3 Field Strength Conditions

Fields that are weaker than the Brillouin field will not balance the beam's space charge forces and scalloping of the beam will occur with an average beam radius that is larger than the entry radius. Stronger fields, on the other hand, will more than balance the beam's space charge forces and scalloping of the beam will occur with an average beam radius that is smaller than the entry radius. Simulated beam scalloping (see Appendix C) for each of these two cases is illustrated in Figure 4.6.

In practice, focusing fields that are 50 to 100 per cent stronger than the Brillouin field are used to ensure sufficient confinement of the real, space-charge modulated beams in the output sections of TWTs [8], [14]. These field strengths result in the simulated beam scalloping of Figure 4.7. This scalloping can be greatly reduced by using confined flow, in which magnetic flux threads the cathode [2], [11], [15], [16]. However, many designers (those on the University of Natal TWT Demonstrator Project team included) avoid the more difficult design of a gun that is not magnetically shielded. Beams from shielded guns are therefore operated into stronger fields with beam smoothness being sacrificed for increased beam stiffness [3]. This is however not an optimum solution since the reduced average beam radius results in less beam interaction with the slow wave structure. Neutralization of space charge by ion entrapment can further reduce the beam radius and the RF interaction [2], [16].

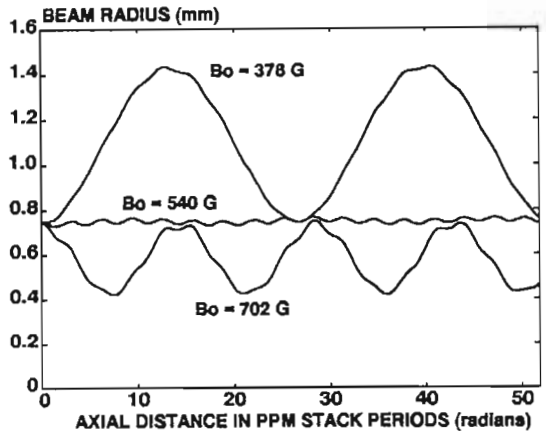

Figure 4.6 Simulated Scalloping Due to Fields 30 % Weaker than, 30 % Stronger than, and Equal to the Brillouin Field

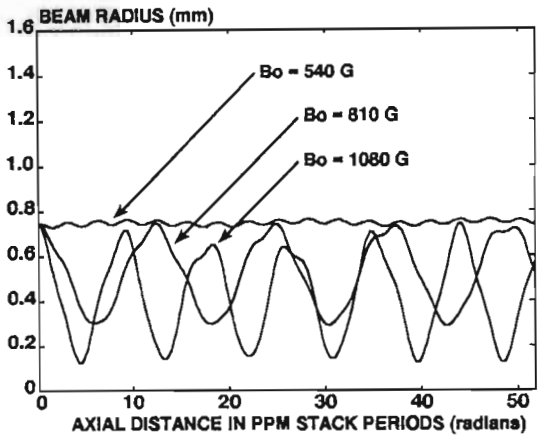

Figure 4.7 Simulated Scalloping Due to Fields 50 and 100 % Stronger than and Equal to the Brillouin Field

4.3 THE STACK GEOMETRY

Many PPM stack configurations are possible for producing a desired focusing field (examples can be found in [8], [17], [18], [3], [19], [10], [9]). Some important factors in choosing a configuration are the strength and shape of the permanent magnets that are available, the details of the TWT's design, and the cost effectiveness of the stack design.

The configuration of the PPM stack that was designed for the low profile TWTs is presented in Figures 4.8 and 1.1. It was adapted from the experimental PPM focusing stack of Stokes [1]. His stack was designed for confinement of a similar, 4500 V, 80 mA, 1.5 mm diameter electron beam but needed to be modified to accommodate the RF, mounting and support structures that would allow it to be used with the low profile TWTs. In addition to being structurally different, the new stack was also magnetized differently to that of Stokes.

The stack in Figure 4.8 consisted of seventeen ring magnets between eighteen flux-guiding pole pieces. Of the stack's components, the 1.5 mm wide pole pieces in its middle; the brass hubs that were used to coaxially align the 12 mm inner diameter Alnico 8 magnets on a 9 mm diameter molybdenum tube; and the magnets themselves are due to Stokes. The details of the stack's magnetic circuit design are presented in his thesis [1] and are therefore not repeated here.

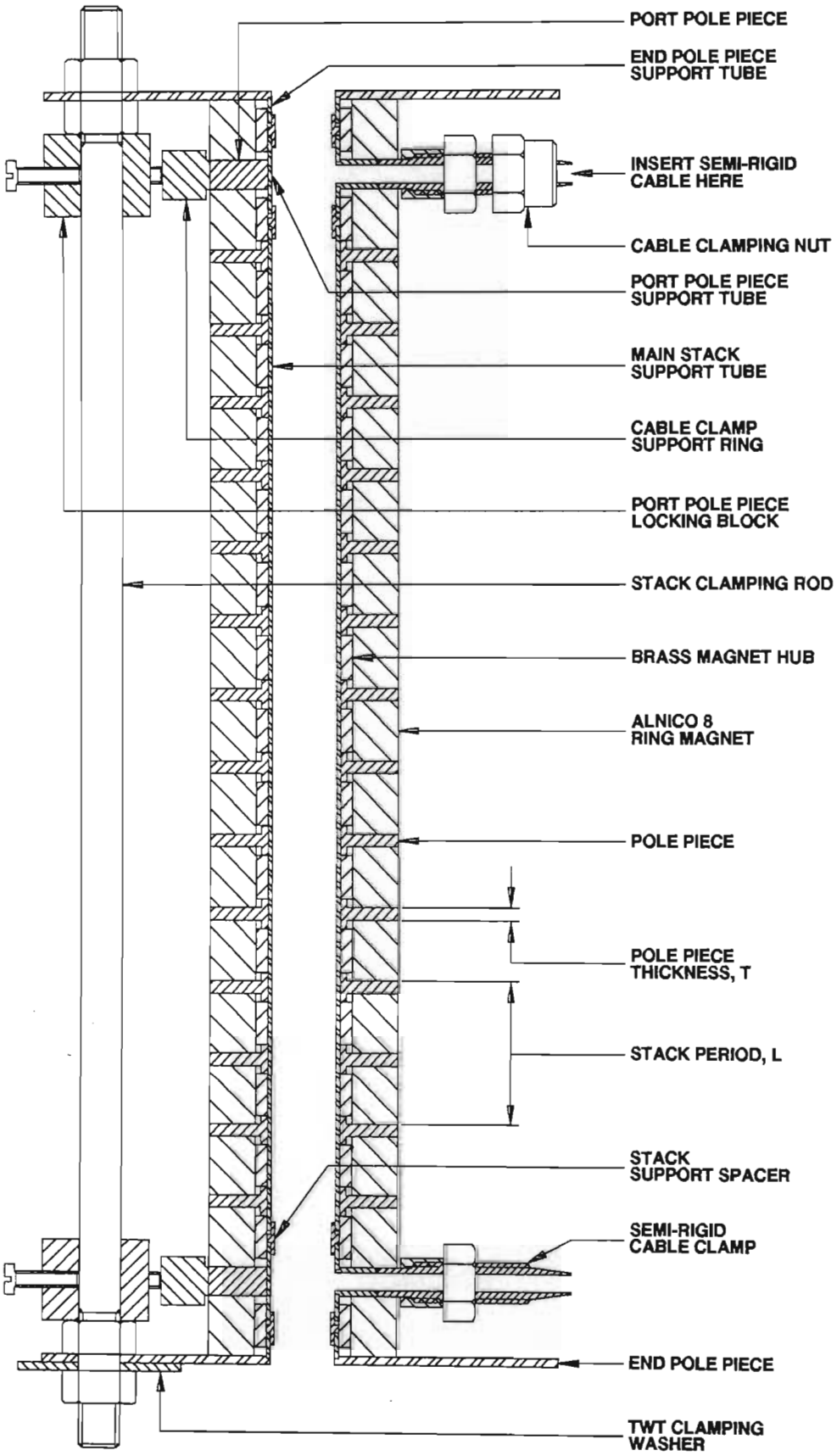

Figure 4.8 The PPM Stack of the Low Profile TWTs

All of the stack components, except the Alnico 8 ceramic magnets (and the standard metric nuts and bolts), were hand made at the University of Natal from pieces of rod, tube and plate. The magnetic materials that were used were mild steel and kovar. The nonmagnetic materials were stainless steel, molybdenum and brass. The mild steel pole pieces were cadmium plated to prevent them from rusting but the other parts were untreated. Slight oxidation of the molybdenum and kovar parts therefore occurred but this was acceptable on an experimental structure.

The end pole pieces of the PPM focusing stack were part of the stack support structure shown in Figure 4.9. They were made from 1 mm thick kovar plate and each was then brazed to a short molybdenum support tube. Figure 4.10 illustrates how nuts and washers were used to clamp the stack to a TWT. Since the two TWT plates that the stack butted against were also made from kovar, they acted as part of the first "pole piece". The stack was assembled onto a TWT when required, as shown in Figure 4.11. Although a TWT could be plugged into and unplugged from the stack, this was not done for TWTs on the pump as they were in an awkward position and could have been broken. The stack had an inside diameter of 8 mm and was supported on the 7 mm diameter vacuum envelope by four stainless steel spacers, two of which are shown in the "exploded view" of the stack support structure in Figure 4.12.

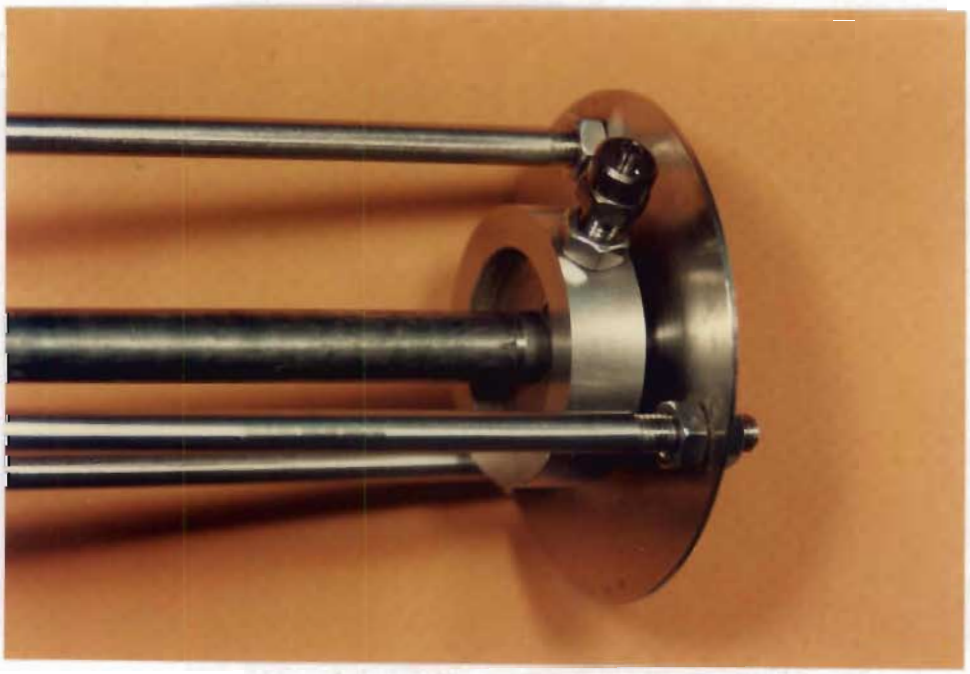

Figure 4.9 The Stack Support Structure

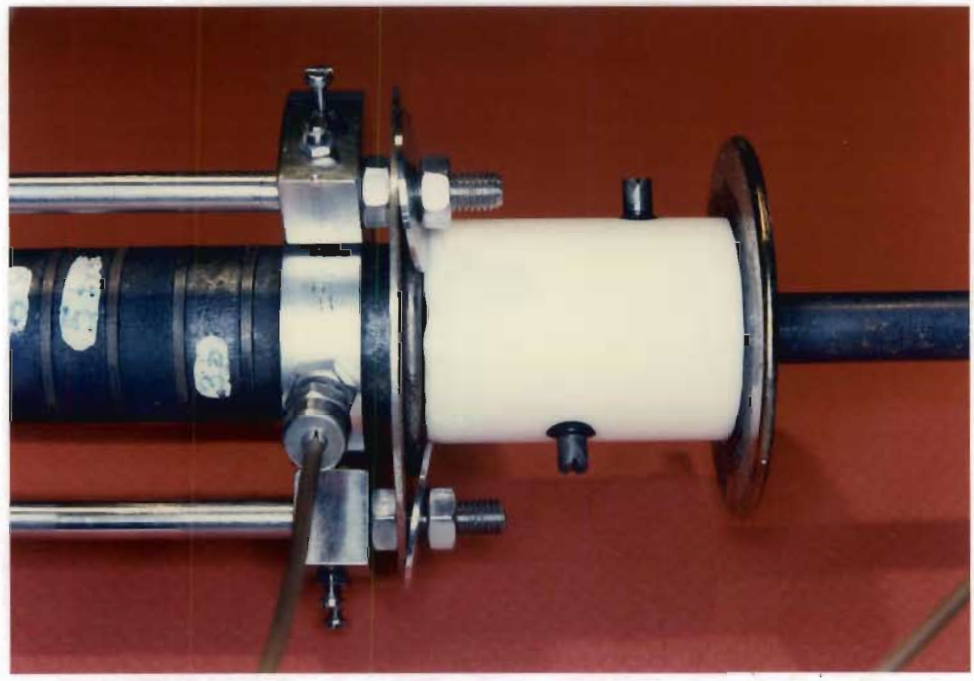

Figure 4.10 The Clamping of the Stack to the Anode Plate

Figure 4.11 The Stack Being Assembled onto a TWT by the Author

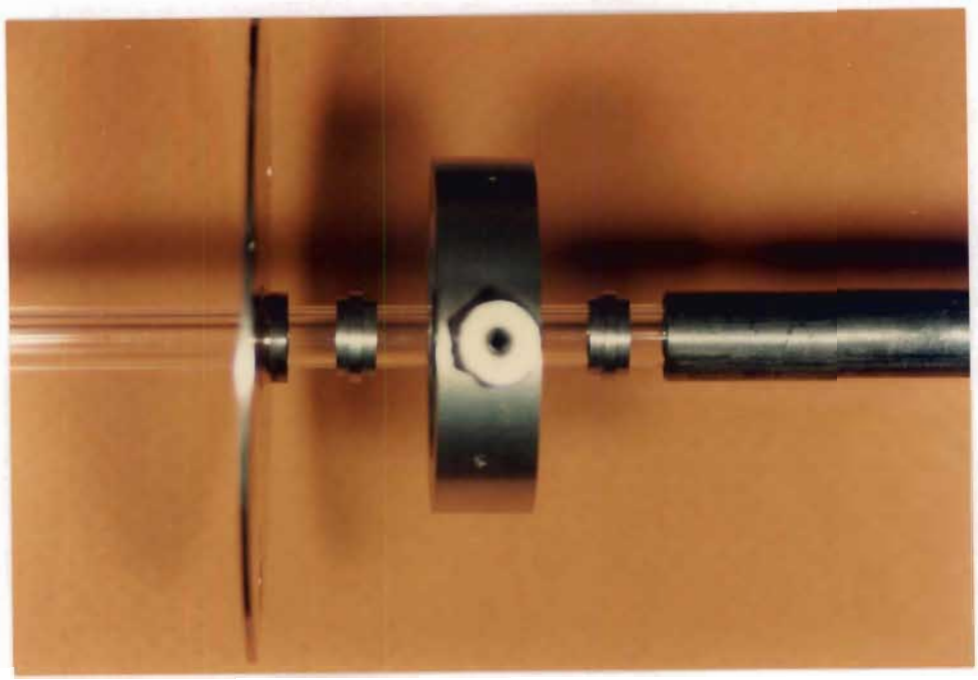

Figure 4.12 Two Stack Support Spacers, the Main Stack Support Tube, a Port Pole Piece Assembly and an End Pole Piece

The second and seventeenth pole pieces were positioned over the helix transitions. These pole pieces were 3.5 mm wide and had radial holes in them to provide space for a TWT's input and output cables. Pole pieces with such holes in them had no measurable undesirable transverse fields associated with them. They were however 2 mm thicker than the pole pieces in the centre of the stack and, together with the thinner end pole pieces, they altered the magnetic period of the stack (L in Figure 4.8).

To keep the period constant, the magnets on either side of a pole piece of normal thickness would have needed to be grooved [17] or the RF transitions would have needed to be accessed via slotted magnets [18]. Simulations (described in Appendix C) were done to determine whether these measures were necessary.

Simulated focusing results for stacks of 540 and 700 G peak are depicted in Figure 4.13. Two curves, corresponding to a constant period and the actual stack period, are plotted for each field strength. The effect of period variations was small, with neither the phase nor the amplitude of the beam ripple being significantly altered. This confirmed Moats' findings that small period irregularities have little effect on beam focusing [20] but contradicted Mendel's earlier warning against period changes [21]. No great benefit would therefore arise from taking the extra trouble to maintain a constant period.

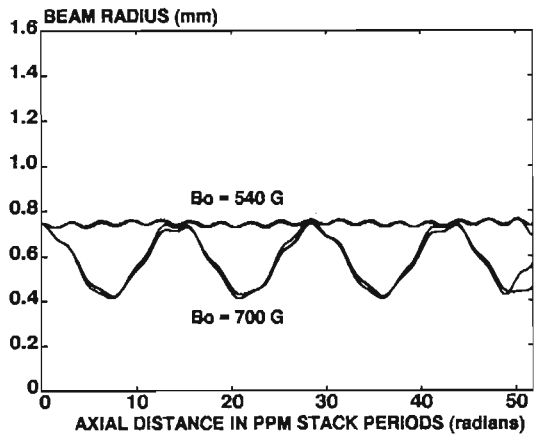

Figure 4.13 The Effect on Simulated Beams of the Period Changes Introduced By the Four Different Pole Pieces

The port pole pieces could be rotated about the beam axis to align their holes with the TWT input and output ports. After alignment they were locked in place to prevent misalignment during the stack adjustment process in which magnets were rotated (see Section 4.4.3). Alignment of the RF transitions and the port pole pieces was achieved visually. A kovar plate was used to reflect light down a pole piece hole while the transition's plug was viewed through a hole in the plate. An alternative method was possible with test structures that had neither collectors nor electron guns. Light from a 50 W halogen lamp was shone into the ceramic tubes of the transitions. Their plugs would then appear as dark spots in the translucent alumina when viewed through the pole piece holes.

Most of the pole pieces in the centre of the stack had the 1.5 mm thickness (T in Figure 4.8) specified by Stokes but some 1.7 mm thick pole pieces were also used to lengthen the stack slightly. Small possible variations in the stack length were useful in reducing the tolerances on the vacuum envelope components. The distance from the input to the output transition of each TWT was specified to be 0.5 mm too long for the unlengthened stack so that thinner pole pieces were not also required.

The stack was originally designed for the electron guns of Smith [22]. The beam minimum of these guns was 4.0±1 mm in front of the kovar plates to which their anodes were joined. This position was about 1 mm in front of the PPM stack's first flux peak, as depicted in Figure 4.14.

The electron guns that the stack was finally tested with were designed by Foulis [23]. These guns offered control of the electron beam and are described in Chapter 5. The position of their beam minimum was 4.6±0.25 mm in front of the anode plate for optimum gun focusing. At the expense of a reduction in beam laminarity, this position could be adjusted by up to 2 mm either way, as shown in Figures 4.14 and 5.2 (b). Adjustments of the gun focus would simultaneously alter the beam radius, as illustrated in Figure 5.2 (a). Easy optimization of the stack entry conditions was thus possible.

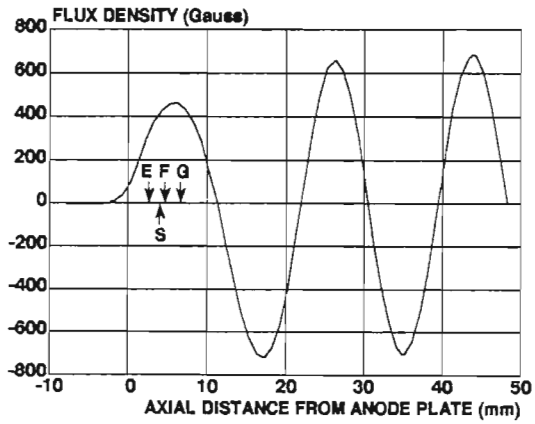

Figure 4.14 S is the Position in the Magnetic Field of the Beam Minimum of Smith's Gun [22] and EFG is the Range Over which that of Foulis' Gun can be Adjusted [23]

4.4 PPM STACK MAGNETIZATION

4.4.1 The "End Effect"

The magnetization of the stack to a particular peak axial flux for each half period of the stack profile proved to be non trivial. All the magnets in a stack contribute to the field in any cell (here defined as a magnet and its pair of half pole pieces) and these contributions are not symmetrical at the ends of the stack. This "end effect" [24] results in the peak field of the end cells being lower, and that of their adjacent cells being higher, than that in the cells of the centre of the stack. Figure 4.15 shows the resulting peak axial field for each cell of the stack when assembled from magnets that had been magnetized individually to a peak axial flux of B_{air} = 430±3 G in air. The "end effect", in which the peak axial field of B_{stack} = 687±13 G in the centre of the stack falls to B_{stack} = 464 and 489 G at the ends of the stack, can clearly be seen.

4.4.2 Reducing the "End Effect"

The "end effect" needs to be reduced for applications that require PPM stacks with a constant peak axial flux for all cells. Since the "end effect" is a function of the stack geometry and magnetization, these can both be manipulated to reduce it or its effects on beam focusing. Methods that were encountered to do this include: magnetizing the stack to a value 20 per cent higher than that required [25]; using an optimum geometry in which contributions from neighbouring cells are minimized [24]; ensuring that the outer diameter of the pole pieces is equal to that of the magnets [25]; using larger diameter magnets at the ends of the stack [25]; using stronger, smaller inside diameter magnets at the ends of the stack and alternating these with weaker, larger inside diameter magnets further into the stack [18]; undercutting pole pieces [18]; and assembling the stack from magnets that have each been magnetized to a different value [25].

Magnetizing the stack's magnets to different strengths was chosen but a published account of how to do this was not found. An empirical approach was therefore decided upon to determine the required values.

Using the method that was developed for reducing the "end effect" [26], a stack can be magnetized to a wanted profile. Besides a reduction in the "end effect", desired entry field strengths can be achieved and the "programming" of fields is simplified. In "programming", the magnetic field of a PPM stack is increased along the stack to provide stronger focusing as the beam is increasingly bunched by high RF drive [14].

In the method that was developed, all seventeen of the stack's magnets were magnetized to the same peak axial value in air and the assembled stack profile was measured. Various magnets were then replaced with ones of different strength and the effects on the stack profile were noted. The replacement magnets were approximately 50 per cent stronger or weaker than the rest. Two magnets, at equal distances from the end of the stack, were replaced at a time (for example: magnets number 2 and 16 were both replaced first by stronger magnets, then by weaker magnets). The magnitudes of the relative changes in the field strength of each cell position for the stronger and the weaker case were then averaged. Effects on pairs of cells equidistant from the ends of the stack were also averaged. Using the simplification that the effects were linear, and ignoring effects further than four magnets away, a coefficient matrix $[\,C\,]$ was calculated

such that:

$$[\ C\ ][\ B_{air}\ ] = [\ B_{stack}\ ] \tag{4.1}$$

where $[\ B_{air}\ ]$ and $[\ B_{stack}\ ]$ respectively are vectors containing the peak flux magnitudes of the magnets in air and of the cells in the assembled stack.

The $[\ B_{air}'\ ]$ required to produce a wanted $[\ B_{stack}'\ ]$ was calculated using MATLAB (a numeric computation software package by The MathWorks, Inc.) from:

$$[\ B'_{air}\ ] = [\ C\ ]^{-1}[\ B'_{stack}\ ] \tag{4.2}$$

The magnets were remagnetized to these calculated values and the assembled stack profile was measured. The simplification of linear effects resulted in errors of up to 10 per cent between the wanted and measured values. An error vector $[\ E\ ]$ was calculated yielding:

$$[\ C\ ][\ B''_{air}\ ] = [\ E\ ][\ B'_{stack}\ ] \tag{4.3}$$

Solution of equation (4.3) for $[\ B_{air}''\ ]$ resulted in an improved stack profile and a further iteration produced the stack profile of Figure 4.16. No further iterations were done because the axial flux of each field was within 5 per cent of the 700 G target value and this has been reported to be adequate by some authors [8], [18] although not by others [20]. The first and last magnets were required to operate at saturation to achieve this. If a stronger field had been required, a different method, such as using the larger diameter Alnico 8 magnets available, would have been required to reduce the "end effect".

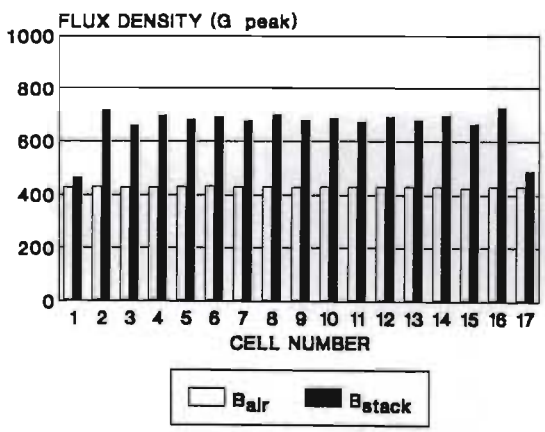

Figure 4.15 Peak Axial Magnetic Field of the PPM Magnets and the Resultant Peak Axial Stack Fields

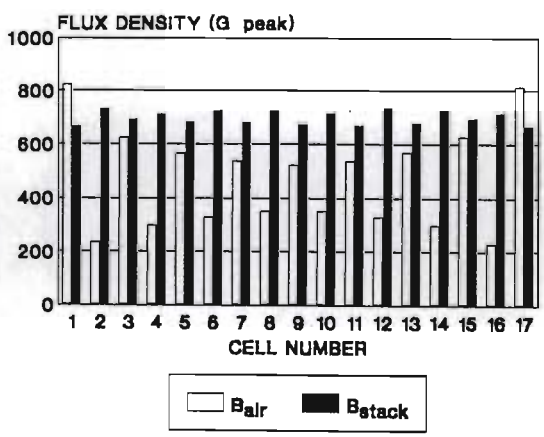

Figure 4.16 Peak Axial Magnetic Field of the PPM Magnets and the Resultant Peak Axial Stack Fields

4.4.3 Adjusting the Stack

Final adjustment of a PPM stack is achieved on a working tube. Magnetic shunts are placed externally across cells whilst the tube parameters are monitored. The shunts reduce the reluctance of the external leakage flux path and an increase in leakage flux results, causing a corresponding decrease of the cells' peak axial fields. Neighbouring cells are also affected though. For example: shunting a cell to reduce its peak axial flux from 740 to 698 G, a 5.7 per cent reduction, resulted in a 0.86 and 0.87 per cent reduction of the flux in the adjacent cells.

During adjustment, the beam transmission and TWT gain are optimized. Weaker fields result in more gain, due to the wider beam interacting more strongly with the closer helix, but also result in more interception of the high power beam by the helix. In addition to the shunting of cells, magnets are also rotated, making use of magnet-imperfection-related transverse fields to optimize the beam and stack alignment.

Adjustment costs can exceed 10 per cent of the total cost of each TWT [20]. PPM stack testing and adjustment is simpler and cheaper for field replaceable TWTs than it is for packaged tubes. Since the stacks of field replaceable TWTs are not integral parts of the tubes, their fields can easily be measured. This allows automated screening of stacks, prior to final adjustment on a TWT, which can eliminate costly attempts to adjust defective stacks [27]. Viable stacks can then be adjusted with well-characterized electron guns.

4.5 FOCUSING RESULTS

4.5.1 Simulated Results

The Brillouin field for a 4500 V, 80 mA electron beam of 1.5 mm diameter was calculated as 540 G peak [1]. In order to satisfy practical requirements, a peak axial field of 700 G was used for TWT LP8, the first operational low profile TWT. A field that is 50 to 100 per cent stronger than the Brillouin field was recommended in Section 4.2.3 but 30 per cent was considered to be sufficient here since the 3 mm helix inside diameter was twice the minimum beam diameter.

The field profile of the 700 G stack that was used is shown in Figure 4.16. In the author's haste to reduce the stack's "end effect", its entry field (see Section 4.2.2) was inadvertently made too strong. It turned out that the original stack profile, shown in Figure 4.15, had almost the correct entry field strength. The results of PPM focusing simulations (see Appendix C) for both stack profiles appear in Figure 4.17. Because the incorrect entry field was used, both the peak beam radius and the amplitude of the beam ripple were larger for the stack of Figure 4.16 than for the stack of Figure 4.15. Nevertheless, a low beam interception is suggested for both stacks by the relatively large distance from the beam edges to the helix.

A peak axial field of 1000 G was used for TWT LP10, the second operational low profile TWT. A field 85 per cent stronger than the Brillouin field was considered necessary for this tube because the helix inside diameter had been reduced from 3 to 2 mm while the beam minimum radius had remained unchanged.

PPM focusing simulations were also conducted for the 1000 G stack. The simulated results are presented in Figure 4.18 and the stack's field profile is depicted in Figure 4.19. The simulations showed the penalty of large beam ripple that is incurred when confined flow is not used with relatively strong fields (see Section 4.2.3). Beam interception in TWT LP10 was expected to be higher than for TWT LP8 because its simulated beam edge was closer to the helix.

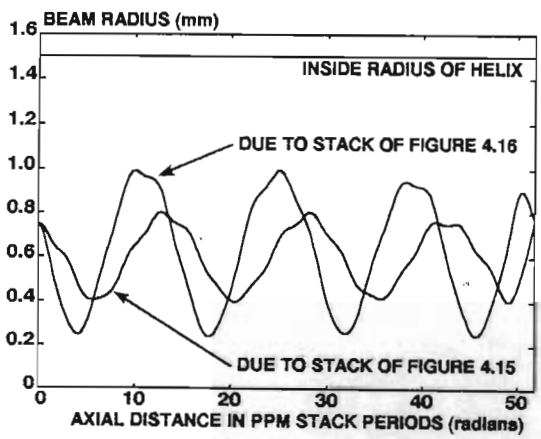

Figure 4.17 Simulated Beam Scalloping for the two 700 G Stacks

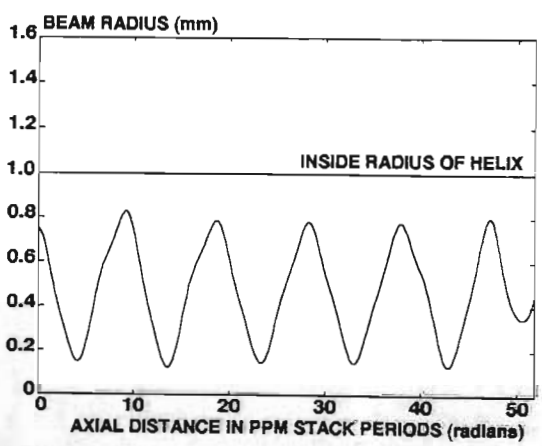

Figure 4.18 Simulated Beam Scalloping for the 1000 G Stack

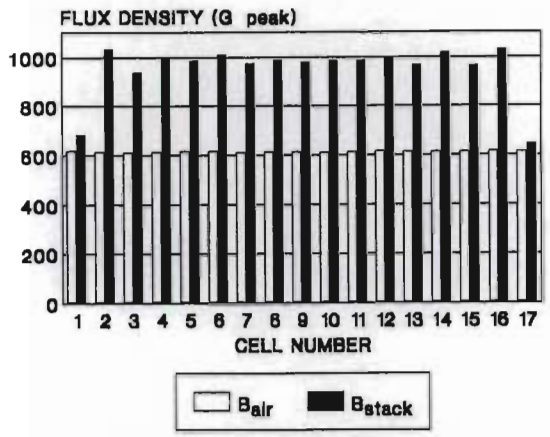

Figure 4.19 Peak Axial Magnetic Field of the PPM Magnets and the Resultant Peak Axial Stack Fields

4.5.2 Measured Results

The measured transmission of a 4600 V, 80 mA beam of 1.5 mm diameter, down a 134 mm long helix of 3 mm inside diameter, by the 700 G stack was good. With the gun optimized for maximum beam transmission, a low helix interception of 0.9 mA was obtained for a beam current of 79.5 mA even before the stack was adjusted. This translates to an anode to collector transmission of just less than 99 per cent. A reduction of this interception to 0.5 mA, for the same beam current, was achieved by adjusting the stack. Adjustment was simple, the rotation of individual magnets about the beam axis being all that was required to achieve just over 99 per cent transmission. Optimizing the gun focus for maximum TWT gain reduced the transmission to just over 98 per cent. When the TWT was driven into saturation, as shown in Figure 8.2, the increased space charge modulation of the beam resulted in reduced transmission. Transmission at saturation was nevertheless better than 96 per cent.

Due to the anode to cathode transmissions of over 98 per cent, the helix interception of about 5 Watts was low enough to allow for continuous small signal operation of TWT LP8.

The measured transmission of a 4500 V, 80 mA beam, down a 134 mm long helix of 2 mm inside diameter, by the 1000 G stack was also good. With the gun optimized for maximum beam transmission, a helix interception of 13.2 mA was obtained for a beam

current of 76.6 mA before the stack was adjusted. This represents an anode to collector transmission of only 82.8 per cent. A reduced interception of 3.3 mA, for an 84.1 mA beam current, was achieved by adjusting the stack. Again, adjustment was simple, the rotation of individual magnets about the beam axis being all that was required to achieve just over 96 per cent transmission at saturation (43.3 dBm output power at 5.1 GHz). TWT LP10 was unstable though (see Chapter 8) and transmission measurements for an unmodulated beam were not possible for a 4500 V beam voltage.

4.5.3 Discussion of Results

The helix interception of each TWT could easily be optimized by manipulation of the gun focusing (see Chapter 5). This was due to the combined optimization of the beam characteristics and of the stack entrance conditions. It is possible that this optimization resulted in partial compensation for the excessive entrance field strength of the 700 G stack.

Adjustment of each stack was easily accomplished by rotation of some of its individual magnets. Repeatable results were obtained after readjusting the 1000 G stack that was removed from, and then reassembled back onto TWT LP10.

TWT LP10 was more sensitive to the adjustment of its 1000 G stack than TWT LP8 was to the adjustment of its 700 G stack. This was because the beam filling factor (the ratio of the beam radius at the beam minimum to the helix inner radius) of TWT LP8 was 0.5 while that of TWT LP10 was 0.75.

Since the simulated beam edges of Figures 4.17 and 4.18 were some distance from the helices, the simulations suggested that the beams of both TWTs would be confined. They did not suggest how well the beams would be confined but that was not their purpose. The numerical solution of the paraxial ray equation was intended to determine only the sensitivity of the beam focusing to certain variables and whether any large errors had been made.

One question that the simulations helped to answer was whether the magnetic period irregularities introduced by the four customized pole pieces of the stack would

significantly affect the beam focusing. Since the simulated beam profiles due to constant and irregular magnetic periods were similar, it was concluded that the effects of the period irregularities would be small. Large interception currents were therefore not expected for the stacks. The measured beam transmissions were good, confirming this expectation.

4.6 CONCLUSIONS

PPM focusing of electron beams down two helices of different inside diameter has been demonstrated by two removable, and hence reusable, magnet stacks. The design procedures that were followed resulted in good confinement of the beams of the two operational TWTs and beam transmissions of over 96 per cent were achieved even during saturated operation of the TWTs. The field strengths and shapes chosen for the two structurally similar PPM stacks may not have been optimum but they were nevertheless adequate.

The effective magnetization of a PPM stack requires a procedure for determining the magnetization of individual magnets in such a way that "end effects" are reduced and an acceptable stack profile is achieved. The empirical technique developed produced the required results.

REFERENCES

[1] A.W. Stokes, *Magnetic Focusing of Electron Beams for Linear Beam Tubes*, M.Sc. Thesis, Department of Electronic Engineering, University of Natal, July 1990.

[2] J.R. Pierce, *Theory and Design of Electron Beams*, Second Edition, D. Van Nostrand Company, Inc., Chapters 9 and 11, 1954.

[3] J.F. Gittins, *Power Travelling-Wave Tubes*, The English Universities Press Ltd, Chapter 4, 1965.

[4] J.W. Gewartowski and H.A. Watson, *Principles of Electron Tubes*, D. Van Nostrand Company, Inc., Chapter 3, 1965.

[5] P.B. Priestland and H.L. Hartnagel, "Theory of Periodic Electrostatic Focusing of Electron Beams", *IEEE Transactions on Electron Devices*, Vol. ED-15, No. 11, pp. 915 to 935, November 1968.

[6] L. Brillouin, *Physics Rev.*, Vol. 67, p. 260, 1945.

[7] K. Ura and M. Terada, "Equivalence of Periodic Magnetic Field to Uniform Magnetic Field in Electron Beam Focusing", *IEEE Transactions on Electron Devices*, Vol. ED-13, No. 12, pp. 930 to 934, December 1966.

[8] J.T. Mendel, C.F. Quate and W.H. Yocom, "Electron Beam Focusing with Periodic Permanent Magnet Fields", *IRE Proc.*, Vol. 42, pp. 800 to 810, May 1954.

[9] H.A. Leupold, "Bulk Reduction and Field Enhancement in Periodic Permanent-Magnet Structures", *IEEE Transactions on Electron Devices*, Vol. ED-34, No. 8, pp. 1868 to 1872, August 1987.

[10] A. Tauber, H.A. Leupold and F. Rothwarf, "Application of Rare Earth Permanent Magnets to Electron Beam Devices", *Proceedings of the 8th International*

Workshop on Rare Earth Magnets and Their Applications, Dayton, Ohio, pp. 103 to 121, May 1985.

[11] J.L. Rawls, J.R. Ashley and W.P. Kolb, "PPM Focusing of Convergent Beams Emerging from Partially Shielded Cathodes", *IEEE Transactions on Electron Devices*, Vol. ED-14, No. 6, pp. 301 to 305, June 1967.

[12] R. True, "Emmittance and the Design of Beam Formation, Transport, and Collection Systems in Periodically Focussed TWT's", *IEEE Transactions on Electron Devices*, Vol. ED-34, No. 2, pp. 473 to 485, February 1987.

[13] D.C. Buck, "Stability of a Cylindrical Electron Beam in Nonsinusoidal Periodic Magnetic-Focusing Fields", *IRE Transactions on Electron Devices*, Vol. ED-4, pp. 44 to 49, January 1957.

[14] J.R.M. Vaughan, "Electron Trajectories in the PPM-Focused Coupled-Cavity TWT", *IEEE Transactions on Electron Devices*, Vol. ED-24, No. 1, pp. 67 to 68, January 1977.

[15] W.R Ayers, G.A. Kalkanis, A.L. Nordquist and R.W. Vranas, "Rf Beam Spread in PPM Confined-Flow TWTs", *IEDM*, pp. 357 to 360, 1985.

[16] A.S. Gilmour, *Microwave Tubes*, Artech House, pp. 176 to 189, 1986.

[17] F. Sterzer and W.W. Siekanowicz, "The Design of Permanent Magnets for Focusing of Electron Beams", *RCA Review*, Vol. 28, pp. 39 to 59, March 1957.

[18] J.E. Sterrett and H. Heffner, "The Design of Periodic Magnetic Focusing Structures", *IRE Transactions on Electron Devices*, Vol. ED-5, pp. 35 to 42, January 1958.

[19] R. Wolfram, "Application of Cobalt-REPM in Focusing of TWT's", *Proceedings of the 6th International Workshop on Rare Earth Magnets and Their Applications*, Baden/Vienna, Austria, pp. 143 to 146, August/September 1982.

[20] R.R. Moats, "Calculations of Beam Trajectories Under Non-Ideal Conditions of PPM Focusing", *IEDM*, pp. 515 to 519, 1976.

[21] J.T. Mendel, "Magnetic Focusing of Electron Beams", *IRE Proc.*, Vol. 43, pp. 327 to 331, March 1955.

[22] D.M. Smith, *The Theoretical and Practical Analysis of Low Perveance Pierce Electron Guns*, M.Sc. Thesis, Department of Electronic Engineering, University of Natal, January 1990.

[23] B.D. Foulis, *A Gridless, Variable Perveance, Pierce Electron Gun*, Ph.D. Thesis, Department of Electronic Engineering, University of Natal, 1994.

[24] M.J. Schindler, "The Magnetic Field and Flux Distributions in a Periodic Focusing Stack for Traveling-Wave Tubes", *RCA Review*, Vol. 21, pp. 414 to 436, September 1960.

[25] M.J. Schindler, "An Improved Procedure for the Design of Periodic-Permanent-Magnet Assemblies for Traveling-Wave Tubes", *IEEE Transactions on Electron Devices*, Vol. ED-13, No. 12, pp. 942 to 949, December 1966.

[26] N. Vassilopoulos and H.L. Nattrass, "Further Developments in Travelling Wave Tube Design", *Proceedings of the Symposium on Antennas and Propagation and Microwave Theory and Techniques*, Durban, South Africa, pp. 171 to 178, September 1992.

[27] D. Burnham, G.R. Ralston and F. Wohlman, Jr, "Communications TWT Magnet Stack Measurement Station", *Proceedings of the 8th International Workshop on Rare Earth Magnets and Their Applications*, Dayton, Ohio, pp. 137 to 148, May 1985.

CHAPTER 5

MODIFICATIONS TO AN EXISTING ELECTRON GUN DESIGN [1]

5.1 INTRODUCTION

The electron gun referred to here was designed by Foulis and is described in detail in his own thesis [1]. One objective of this chapter is to provide a short description of the gun features that allowed the PPM focusing and RF results of the low profile TWTs to be optimised. The other objective is to report on the author's work towards improving the reliability of the gun.

5.2 BASIC DESCRIPTION OF ELECTRON GUN OPERATION [1]

The electron gun of Foulis is presented in the schematic of Figure 5.1. The gun was designed to operate with its anode at ground potential and its cathode at -4500 V. At this voltage, it could produce a switchable beam of 80 mA with a minimum radius of 0.75 mm occurring at a distance of 19.8 mm from the centre of the cathode surface.

This gun is essentially a convergent Pierce electron gun into which an open aperture switching electrode has been incorporated [1], [2]. The gun behaved as a conventional Pierce gun if the switching electrode was biased at the same proportion of cathode-to-anode potential that an equipotential in a Pierce gun would have in the same position. If that proportion, say ξ, was reduced to zero by biasing the electrode at cathode potential, the electron beam was "pinched off". In this state, the cathode current was low and only a small fraction of emitted electrons passed through the anode aperture. The switching electrode did not intercept any beam current. It could therefore be biased with a simple resistor divider but, in order to increase experimental flexibility, a variable voltage power supply was used instead.

The beam focusing was altered by the switching electrode if ξ was varied by a small amount under beam "on" conditions. Both the radius and the position of the beam minimum could be changed by varying ξ but a tradeoff, illustrated in Figures 5.2 (a) and (b), had to be made with the beam laminarity. The variable focusing facility had several advantages. Tolerance effects in the gun and imperfections in the entrant field to the

magnetic focusing stack could be compensated for, as could slightly different focusing conditions under pulsed or CW operation.

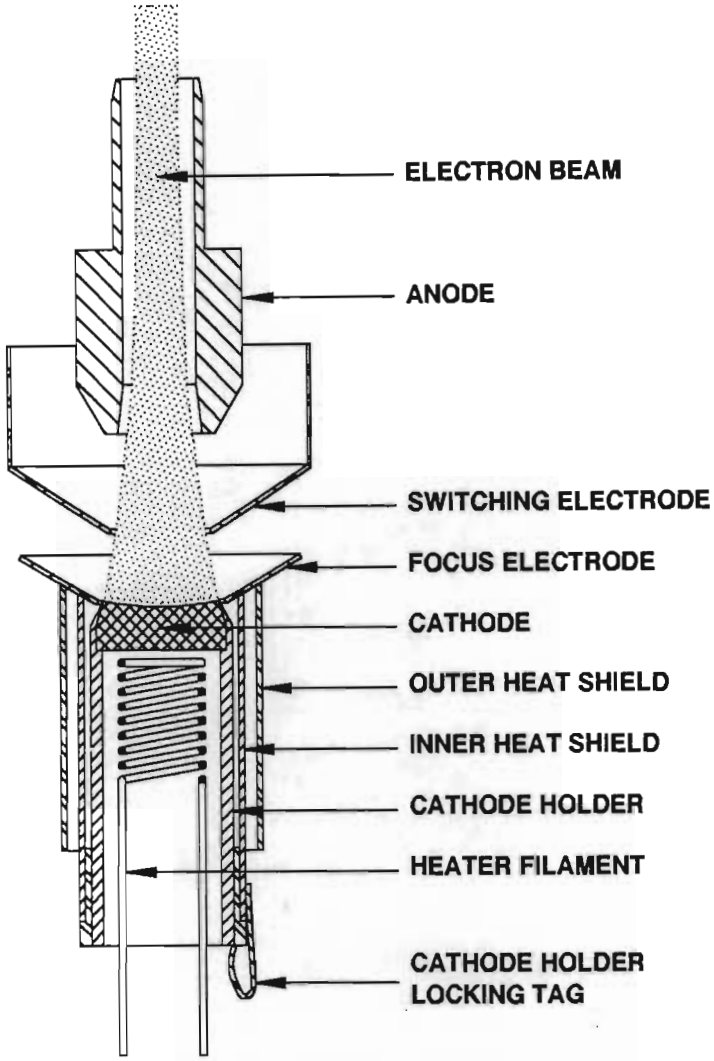

Figure 5.1 Electron Gun Schematic Showing Switching Electrode

(After B.D. Foulis, *A Gridless, Variable Perveance, Pierce Electron Gun*, Ph.D. Thesis, University of Natal, 1994.)

The perveance ($P=I/V^{3/2}$) of an electron gun is usually dependent on the gun geometry and is therefore fixed. By varying the value of ξ, as shown in Figure 5.2 (c), different values of perveance could be obtained for the gun.

In addition, use of the switching electrode resulted in an improved current density profile that was flatter than that of a conventional Pierce gun. This is illustrated in Figure 5.2 (d).

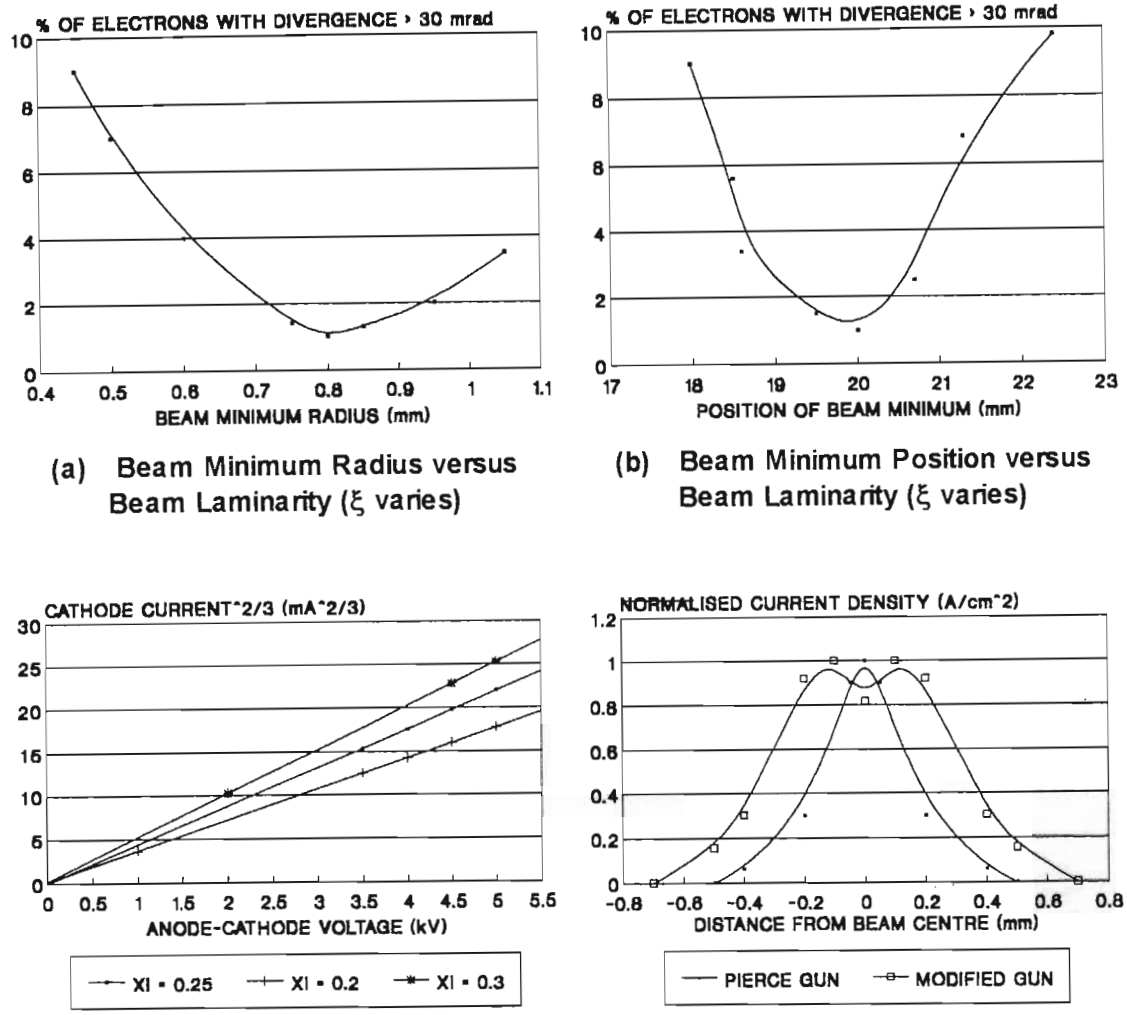

(a) Beam Minimum Radius versus Beam Laminarity (ξ varies)

(b) Beam Minimum Position versus Beam Laminarity (ξ varies)

(c) Variable Perveance of Gun

(d) Current Density Profiles

Figure 5.2 Simulated Electron Gun Results

(After B.D. Foulis, "A Gridless, Variable Perveance, Pierce Electron Gun", Ph.D. Thesis, University of Natal, 1994.)

5.3 ELECTRON GUN CONSTRUCTION [1]

Figure 5.3 is a photograph of the electron gun vacuum envelope. Active solder, described in Chapter 6, was used to braze a kovar plate onto each end of a 30 mm diameter alumina ceramic cylinder. These plates were later electron beam welded to plates of similar diameter on the TWT and pump port structures. Electrical connections to the gun electrodes were via four molybdenum pins that were active brazed into holes in the 2.5 mm thick wall of the ceramic cylinder.

Figure 5.3 Electron Gun Vacuum Envelope

(After B.D. Foulis, *A Gridless, Variable Perveance, Pierce Electron Gun*, Ph.D. Thesis, University of Natal, 1994.)

The electron gun module is shown in Figure 5.4. The switching electrode and the anode and cathode structures were supported on three 3 mm diameter alumina rods by molybdenum wires. These wires were resistance welded to the electrode structures and active brazed to the support rods. Resistance welding the molybdenum support wires to the molybdenum outer heat shield was made possible by sandwiching pieces of nickel between the parts to be joined. Ferry wires were later resistance welded to the electrode support wires to connect them electrically to the molybdenum pins of the vacuum/air transitions.

Figure 5.5 is a photograph of the cathode in its holder, adjacent to the rest of the cathode structure. The two molybdenum heat shields were joined to the ferry focus

electrode by ferry tags that had been resistance welded between them. After being impregnated, the "S" type tungsten matrix dispenser cathode was crimped into the cathode holder that was then pushed into the inner heat shield as illustrated in cross section in Figure 5.1. The three ferry tags at the heater filament end of the cathode structure of Figure 5.5 were later folded over, as in Figures 5.4 and 5.1, and used to lock the cathode holder in place.

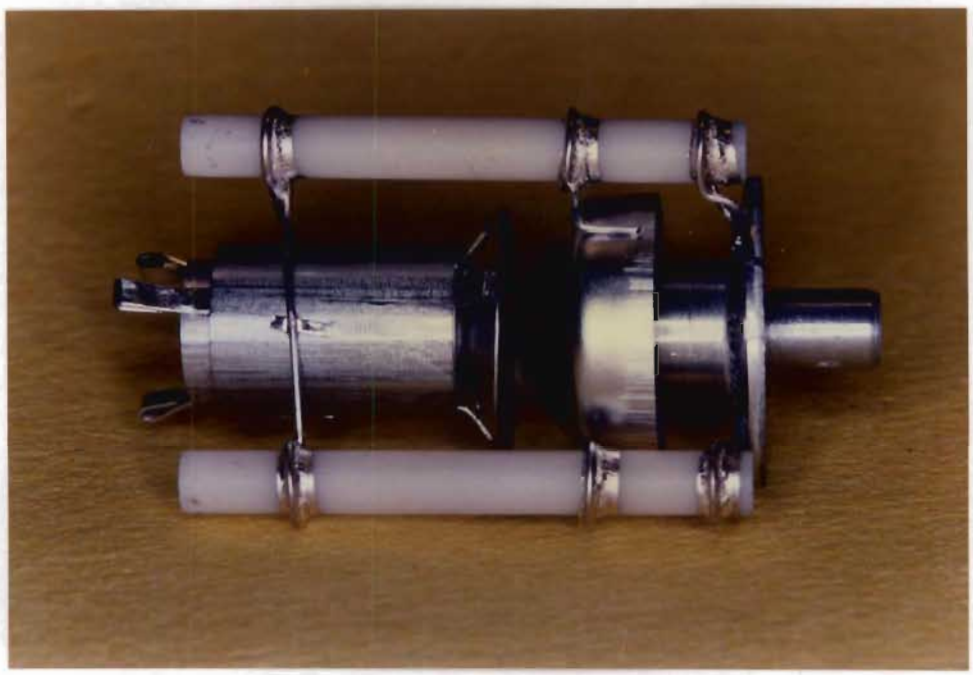

Figure 5.4 Electron Gun Module

(After B.D. Foulis, *A Gridless, Variable Perveance, Pierce Electron Gun*, Ph.D. Thesis, University of Natal, 1994.)

The switching electrode, deep drawn from ferry sheet, was resistance welded directly to its support wires. A kovar plate was brazed to the molybdenum anode using "PALCO" (a 1230°C solidus/1235°C liquidus, palladium/cobalt alloy from the Western Gold and Platinum Co., Belmont California) and the anode support wires were resistance welded to this plate. The gun module was later joined to the rest of the TWT by resistance welding the anode plate to the gun-mounting plate of the TWT.

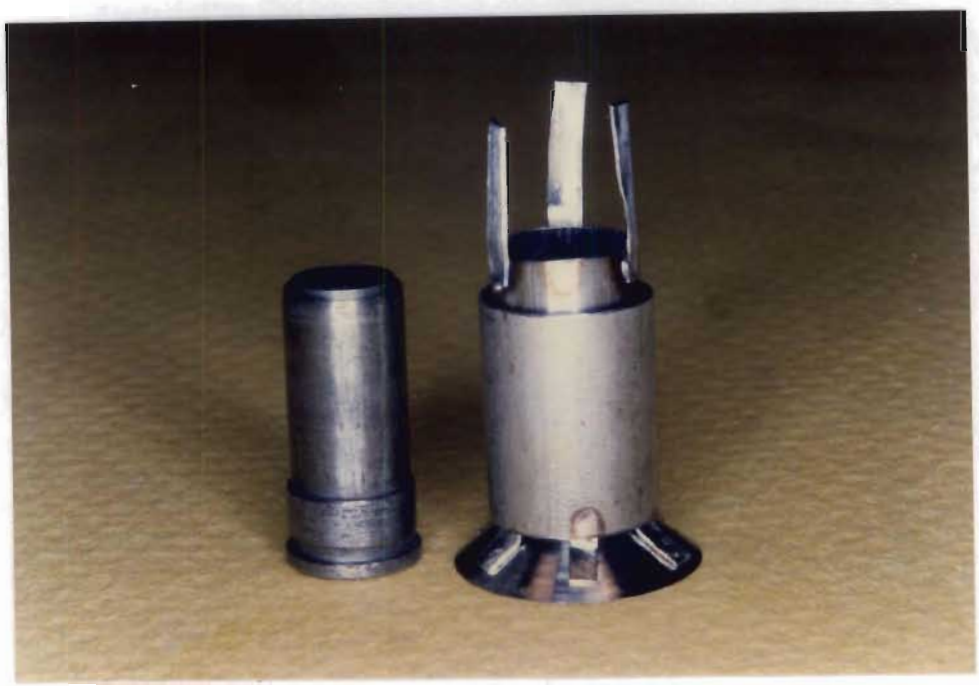

Figure 5.5 Cathode in Holder Adjacent to Rest of Cathode Structure

(After B.D. Foulis, *A Gridless, Variable Perveance, Pierce Electron Gun*, Ph.D. Thesis, University of Natal, 1994.)

5.4 PROBLEMS

Several problems were encountered when the author attempted to use the gun that he had built for the ninth low profile TWT (TWT LP9) according to the design of Foulis [1]. The author's difficulties, due to his lack of experience with the guns, brought attention to some aspects of their mechanical design which could be improved.

The author's troubles began when, during the endeavour to activate the gun's cathode, its emission peaked at only 4.1 mA whereafter it declined. The degradation began at filament powers of less than 30 W and could not be reversed, even by short spells at heater powers of 40 to 50 W that were intended to accelerate cathode formation.

Failure to achieve full emission was attributed to unsatisfactory cathode impregnation and it was decided that the cathode be replaced. The pump port structure was therefore parted from the gun envelope using a lathe. A look inside revealed that the ferry tags that had held the cathode holder in place had melted. Since the gun had been directed

upwards, the cathode holder had fallen back until the cathode rested on the heater filament. The cathode had also shifted off axis and the gun alignment was ruined.

Abnormal operation of the gun of TWT LP9 was first noticed when the heater power was increased to 26.3 W, a previously normal level. It is possible that the ferry tags melted at this power because they were bent too far towards the gun axis, and were therefore illuminated by the heater filament. Evaporated copper (ferry contains 53 to 55 per cent copper and 46 to 44 per cent nickel) might then have poisoned the cathode and prevented activation. It is more probable however that the low emission was due to a poorly impregnated cathode and that the ferry tags melted only when the heater power was pushed to almost twice the usual level.

The planned replacement of the cathode and its holder was not possible because the holder had been brazed into the inner heat shield by the ferry. The whole cathode structure therefore had to be replaced. The gun envelope was parted from the rest of the TWT, to provide easier access to the gun module, and a scalpel was used to prise the cathode structure loose from its support wires. Fortunately, the design of these wires was not as is shown in Figure 5.4. It had been changed by Foulis and was similar to that of the switching electrode support wires in Figure 5.4. It was therefore possible to manipulate the cathode structure out of the gun module.

A new cathode structure was built. Ferry tags (with solidus and liquidus temperatures of 1220 and 1290°C respectively) were again used to join the heat shields and the focus electrode together but not to lock the cathode holder in position. Nickel tags (with a melting point of 1453°C) were used instead. These were not folded, as in the case of the ferry tags, but were just long enough to be resistance welded to both the inner heat shield and the cathode holder.

This new cathode structure was resistance welded back into the gun module. Another cathode was then impregnated, this time more carefully than before. It and a fresh heater filament were fitted to the gun and a second attempt was made to shoot a useful beam down the helix of TWT LP9. Good emission was measured for the cathode but the anode interception suddenly increased to about half the cathode current after one hour of operation. The heater filament power had not exceeded 31 W when this happened.

Testing of the repaired gun was hindered by conductive films that had been deposited onto the electrode support rods during the first cathode activation attempt. These copper tinted films had not been cleaned off during the repair of the gun and they resulted in leakage currents flowing between the gun electrodes, making the measurement of the electrode currents difficult and stressing the power supplies.

The conductive films were prone to thermal runaway. Resistive heating resulted in a decrease in film resistance and the current increased until its leakage path was vaporized, raising the vacuum pressure. Unfortunately, the amount of film vaporized was not sufficient to prevent the process from repeating itself. Each burst of vapour poisoned the cathode, reducing its emission.

The repaired gun was opened after its heater filament fused. The nickel tags were found to have melted but the cathode holder had not shifted relative to the inner heat shield. The gun was nevertheless misaligned, explaining the high anode currents. It was misaligned because the ferry tags that connected the inner heat shield to the focus electrode had partially melted and because the resistance welded joint between one of the three molybdenum support wires and the outer heat shield had broken. This joint had been weak because it was made over the old joint that had been broken when prising the first cathode structure out of the gun. As a result of the cathode holder's movement, the inner heat shield had pushed against the tungsten heater filament, distorting it, shorting out its bifilar windings, and causing it to fuse.

5.5 SOLUTIONS

To avoid the recurrence of the above problems, modification of the gun design of Foulis [1] was decided upon. The objectives were to avoid low melting point materials near the hot parts of the cathode structure; to strengthen the joints between the cathode structure and its support wires; and to prevent the deposition of conductive paths onto the electrode insulators. The structures shown in Figures 5.6 and 5.7 resulted.

A solid molybdenum focus electrode/heat shield, brazed to a molybdenum outer heat shield with palladium (having a melting point of 1553°C), was used instead of three separate structures, tagged together with ferry. To prevent another resistance welded

joint failure, palladium was also used to braze the molybdenum support wire onto the outer heat shield.

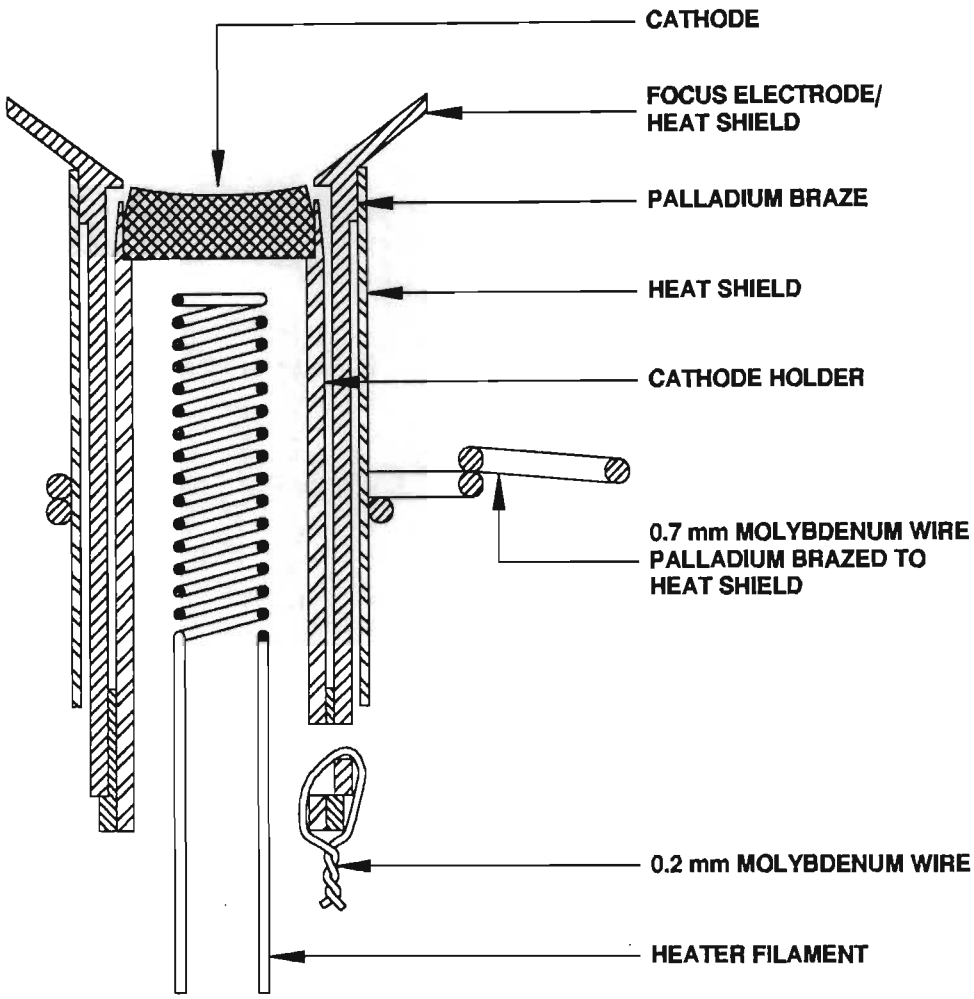

Figure 5.6 A Schematic of the New Cathode Structure

The cathode holders of Foulis were made by separately machining two pieces of molybdenum tube and then plasmajet micro-welding them together. Alignment of the two parts was difficult and discolouration of the structure occurred due to the insufficient protection offered by the welding unit's argon shield. Both problems were avoided in the redesigned cathode holder by first using the electron beam welder to spot weld two molybdenum cylinders together, and then accurately machining them to produce the final, shiny product.

Three holes were drilled into both the cathode holder and the inner heat shield. The holder was tied into place by 0.2 mm diameter molybdenum wires that were threaded through these holes as depicted in Figure 5.8. These wires were far less likely to melt

than the folded ferry tags that had previously locked the holder in place. If a new cathode was required, the wires could easily be cut and the cathode holder replaced.

Figure 5.7 Cathode in New Holder Adjacent to Rest of New Cathode Structure

Figure 5.8 New Cathode Holder Tied into New Inner Heat Shield

Figure 5.9 is a cross section of the whole gun and Figure 5.10 is a photograph of the new gun module. The cathode structure provided good shielding of the lower parts of the alumina support rods from barium that would evaporate off the cathode. The position of

the active brazed joints between the switching electrode support wires and the rods was moved into the shadow of the cathode structure. This reduced the likelihood of surface tracking along the rods. In addition, it made the ratio of the distances between the electrode support wire joints more like that of the voltages between them.

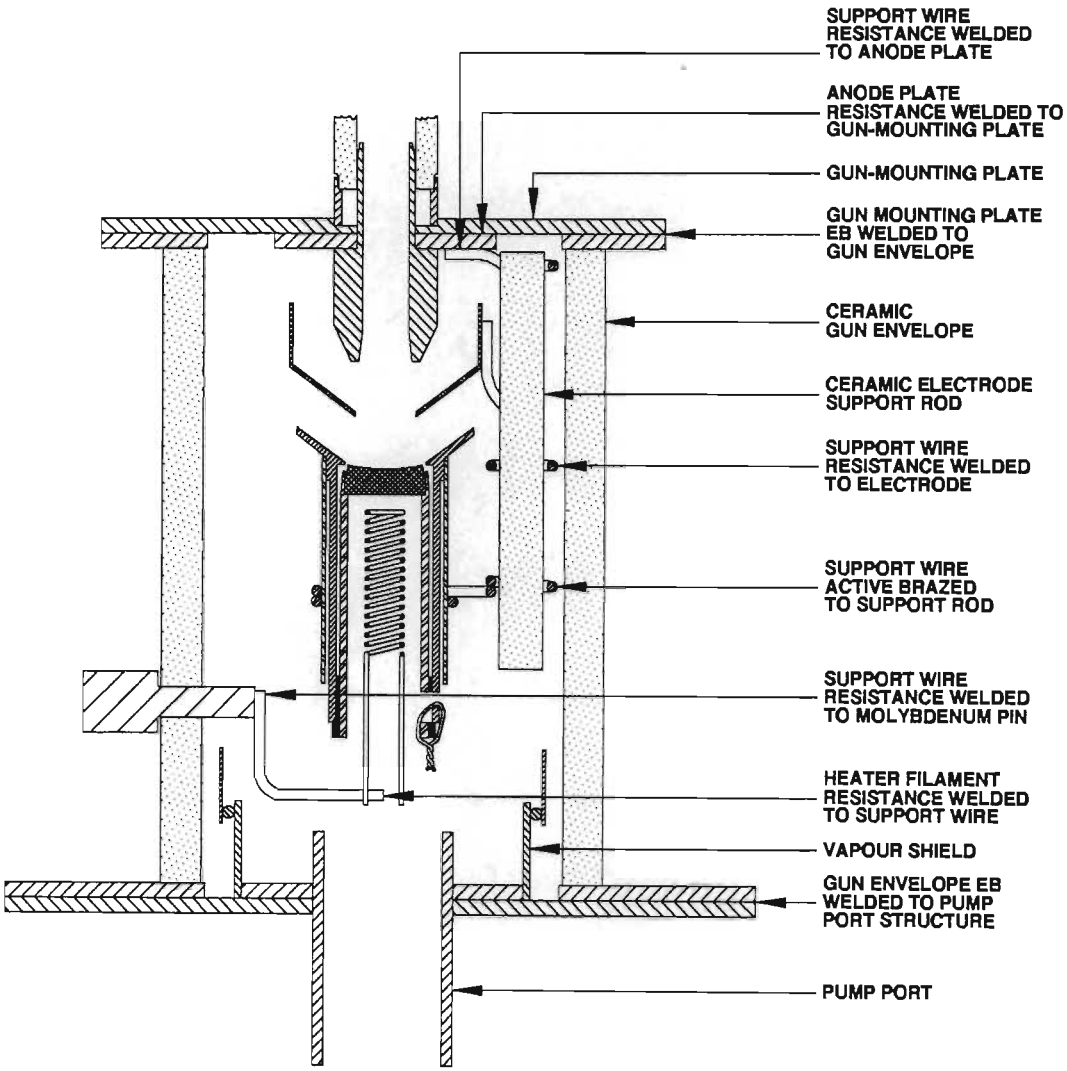

Figure 5.9 The Electron Gun of Altered Mechanical Design

The new gun was used successfully in the second operational low profile TWT (TWT LP10). In addition to being structurally more robust, it had superior thermal characteristics to the gun of TWT LP8. Space-charge limited operation was therefore possible at a heater filament power of 21 W, over 20 per cent less than the 27 W of Foulis's gun.

The cathode structure may have been more expensive to manufacture than that of

Foulis, but this was of little concern as it was an experimental and not a production device.

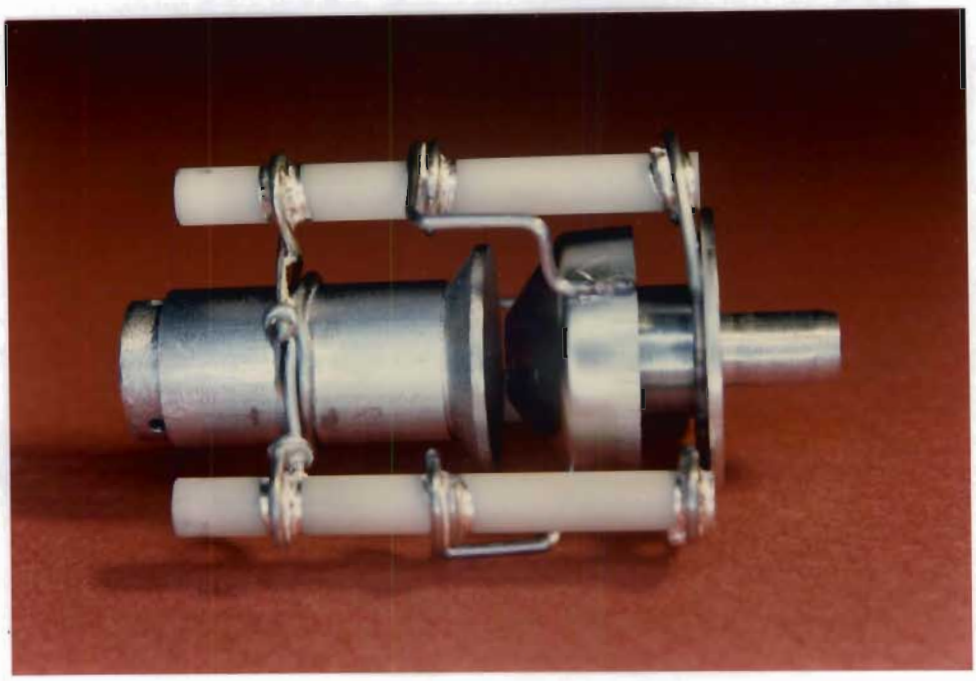

Figure 5.10 The Electron Gun Module of Altered Mechanical Design

5.6 CONCLUSIONS

The author's lack of experience in making and operating the electron guns and cathodes of Foulis [1] resulted in a destroyed TWT. The mechanical design of the gun was improved to reduce the likelihood of a repeated failure. The new gun was built and successfully used.

REFERENCES

[1] B.D. Foulis, *A Gridless, Variable Perveance, Pierce Electron Gun*, Ph.D. Thesis, University of Natal, 1994.

[2] J.R. Pierce, *Theory and Design of Electron Beams*, 2nd Edition, D. Van Nostrand Company Inc., 1954.

CHAPTER 6

TWT CONSTRUCTION

6.1 INTRODUCTION

Much time was spent by the author in overcoming the difficulties associated with the manufacture of the prototype low profile TWTs. If the lengths of the chapters of this thesis were proportional to the time and effort spent on the work they report on, this chapter would be several times longer. Fortunately, the products of skills gained by years of practical experience are very much easier to describe than how the skills were gained.

6.2 ACTIVE BRAZING

Metal/ceramic joining technology is described in many papers and some books, for example [1], [2], [3], [4], [5], [6]. In addition, it has been the subject of an investigation by Hensley in the Materials Science Laboratory of the University of Natal [7]. Of the active solders tested by Hensley, Degussa's CH 4 was found to be the most suitable for making vacuum-tight metal/alumina joints. CH 4 was therefore the sole active brazing alloy used in the manufacture the low profile TWTs and the following discussion is limited to metal/alumina joints brazed with it.

CH 4 comprises 70.5, 26.5 and 3 per cent silver, copper and titanium respectively. The solder melts from 780 to 805°C and can be used for brazing many ceramics, including Al_2O_3, ZrO_2 and Si_3N_4 [6]. The wetting mechanism is well known [4], [6]: Titanium, an active metal with a high affinity for oxygen, diffuses into the ceramic forming titanium oxides and suboxides. A reaction layer results at the interface to the ceramic and after the reaction is complete, no titanium is left in the filler as it is all at the ceramic surface [6], [7]. The copper/silver alloy that remains is ductile and therefore relieves thermal stresses in joints between different materials. The strength of the bond, maximized by a thin oxide layer [7], is often greater than that of the ceramic [4], [6], [7]. In the 850 to 950°C wetting range, higher temperatures result in stronger joints with less scatter in strengths [3], [6]. This is because a more complete reaction occurs at higher temperatures.

No O_2, H_2, N_2, CO, CO_2 or H_2O must be present during brazing. They all react with titanium and a weak bond results from the reduction in both the alloy ductility and the amount of titanium available for bonding [1], [3], [6]. Therefore only an atmosphere of pure inert gas, such as argon, or a vacuum of less than 10^{-4} torr is suitable for brazing. Furthermore, it is important that metal oxides are removed and that the materials to be joined are cleaned and outgassed before brazing.

Even though the filler metal is ductile, metals and ceramics that are joined should have similar coefficients of thermal expansion. Good joints are possible between unmatched materials if thin, ductile metal parts are used and if joints are designed to put ceramics under compression rather than tension. In addition, the surfaces to be joined should be very flat, smooth and without cracks [7], [2], [1].

Degussa state that the wetting properties of their active solders alter when the solders are required to flow. Since capillary action is limited, it is recommended that the solder is always inserted into the joint gap and it is therefore supplied in tape form [8].

Many joints were made and tested by Hensley [7]. The solder was placed between the metal and alumina parts and a pressure of 2500 kg/m^2 was applied during brazing. His results were as follows: kovar and tantalum produced excellent joints; molybdenum produced good joints if properly cleaned, deoxidized and smooth; but copper, ferry and monel produced porous joints.

Molybdenum and kovar were readily available and were therefore used in all the metal/alumina joints of the low profile TWTs. Although molybdenum deteriorates at high ambient temperatures in air and kovar rusts, no protective measures were taken since the tubes were merely experimental and therefore not designed for long life.

6.3 LOW PROFILE TWT ASSEMBLY AND CONSTRUCTION

Figure 6.1 is a cross section of the second operational TWT (TWT LP10) without its gun or magnet stack. The gun is shown in Figure 5.9, the stack in Figure 4.8 and a cross section of the complete TWT assembly in Figure 1.1.

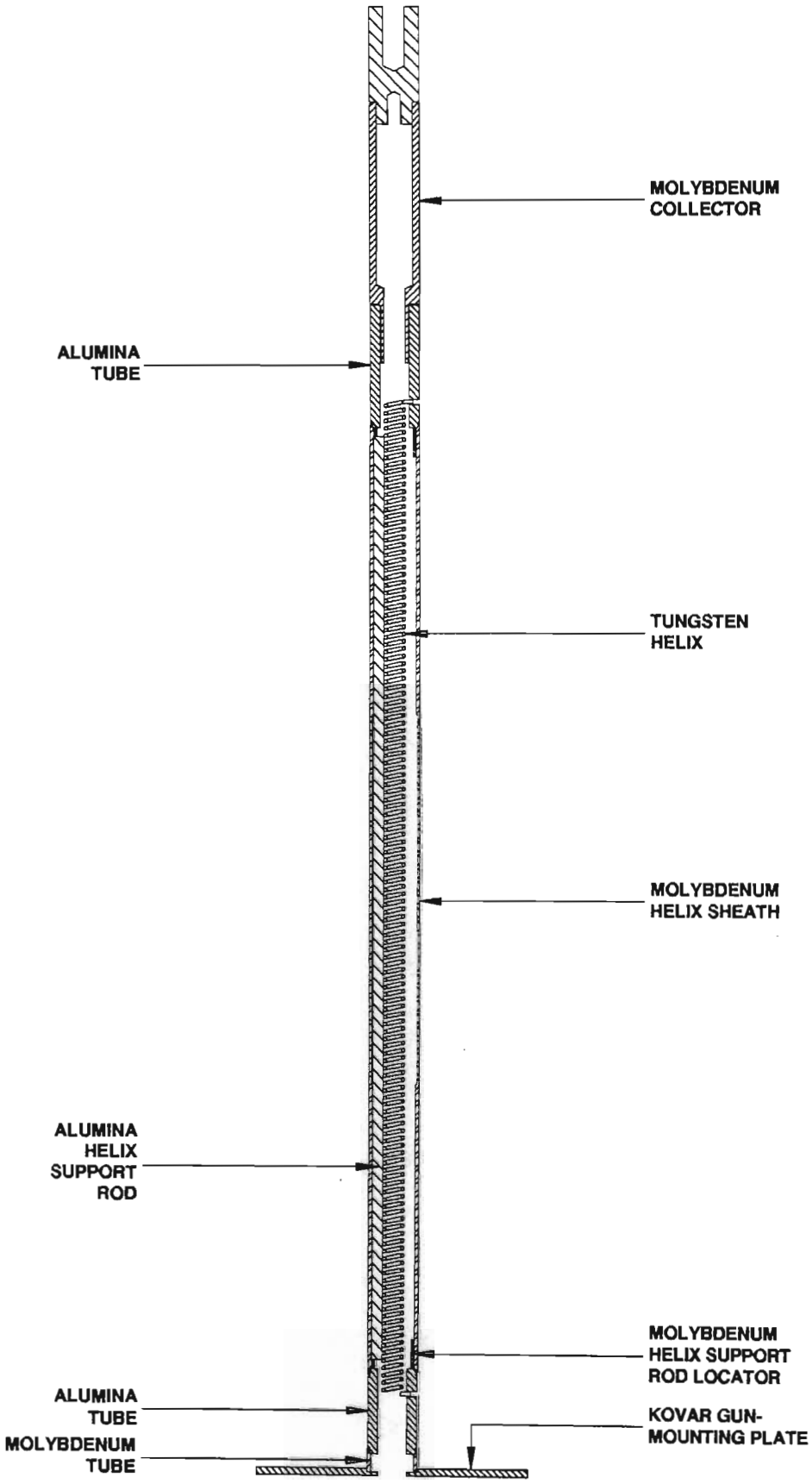

Figure 6.1 A Cross Section of the RF and Collector Structures of TWT LP10

A number of parts needed to be joined to make this structure. Those of TWT LP3, an earlier structure, are displayed in Figure 6.2. The helix was made by winding 0.5 mm tungsten wire onto a 3 mm molybdenum mandrel and then heating both to about 1600°C for a few minutes to recrystallize the tungsten. This prevented the helix from unwinding when the mandrel was later removed. The CH 4 washers were punched out of 0.2 mm foil and the other metal parts were machined to shape. The alumina parts were cut by diamond wheel and drilled ultrasonically. Only Degussit AL-23 ceramic was used.

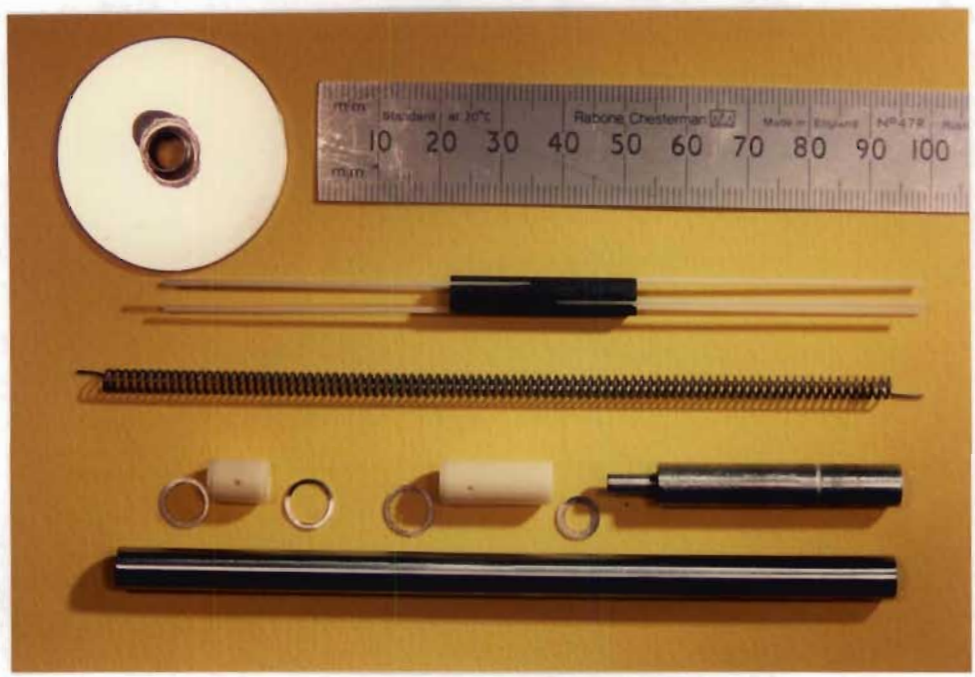

Figure 6.2 The Components of the RF and Collector Structures of TWT LP3

The two parts of the molybdenum collector were induction brazed together using "PALCO" (a 1230°C solidus/1235°C liquidus, palladium/cobalt alloy from the Western Gold and Platinum Co., Belmont California). The tapped hole in the back of the collector was used for jigging a TWT during assembly. Since the collector was insulated from the rest of the TWT, it could be operated at a potential lower than that of the helix.

Depressed potential operation of a collector increases TWT efficiency by slowing down the electron beam before it is collected. Less kinetic energy is wasted and the problem of cooling the collector is simplified. The collector was made in two parts because an increase in diameter was wanted past its entrance. This step would intercept secondary or reflected electrons returning from the collector and prevent them from bombarding the helix.

The collector extended 8 mm into the ceramic tube that it was joined to. This was done to screen the insulator and prevent it from charging as a result of electron bombardment. The unshielded part of the ceramic tube had a larger diameter than the nearby metal parts and would therefore not have charged. Similar screening was provided at the other end of the tube by the anode, as shown in Figure 1.1.

Copper was used to vacuum braze the kovar gun-mounting plate to the short molybdenum tube. The parts were self jigging. The tube rested in the machined recess in the plate and no weight was used during brazing. Good joints were made by fitting a ring of copper wire inside the bottom end of the molybdenum tube. If placed on the outside, the copper would often flow only on the kovar plate. This did not occur if gold wire was used instead of copper wire.

If gold wire was used, good joints, with a fillet both on the outside and on the inside of the tube, resulted. However, a thin coating of gold was left all over the approximately 3 mm long molybdenum tube. This film altered the flow properties of the active solder of the joint that was later made between the molybdenum tube and a ceramic tube. As a result, most of the active solder flowed out of the joint and over the molybdenum tube, ruining the joint.

The TWT parts were assembled in a brazing jig, as shown in Figure 6.3, after being ultrasonically cleaned. The cleaning solvent was changed four times, alternating between deionized water and acetone. As a final step in the pre-braze cleaning process, the jigged structure was rinsed in a freon degreasing plant. Its metal/ceramic joints were then brazed simultaneously in a vacuum furnace.

A vacuum of better than 10^{-3} torr was used and the variation of furnace temperature with time was as plotted in Figure 6.4. The temperature was increased from ambient to 750°C in 20 minutes, kept constant for a 15 minute outgassing period and then increased to the 950°C brazing temperature in 10 minutes. A 100 minute long cooling period followed after 5 minutes.

The 5 minute brazing time was considered sufficient because similar solders were reported to be molten and quiescent after 1 or 2 minutes above 900°C and their sessile drop contact angles were reported to be constant after 2 or 3 minutes at the brazing

temperature [2]. More than 5 minutes were not used because the evaporation of silver from the CH 4 needed to be minimized so that conductive coatings would not be deposited onto the ceramic insulators.

Hensley warns that active solder seals should not be reheated beyond 850°C [7]. This advice was ignored on a few occasions when TWTs were repaired by reheating to 950°C. One structure was even reheated twice. Success was limited. Only some repaired joints were vacuum tight and leaks sometimes resulted in joints that had been good before reheating.

Figure 6.3 The Jigged RF and Collector Structures of TWT LP8

After brazing, each structure was tested for leaks on a mass spectrometer type of leak detector that was tuned to helium. Measurements were then made with an HP8510B network analyzer to determine the cold RF characteristics of the tube. Thereafter, it was stored in a vacuum bell jar until its electron gun was ready to be fitted.

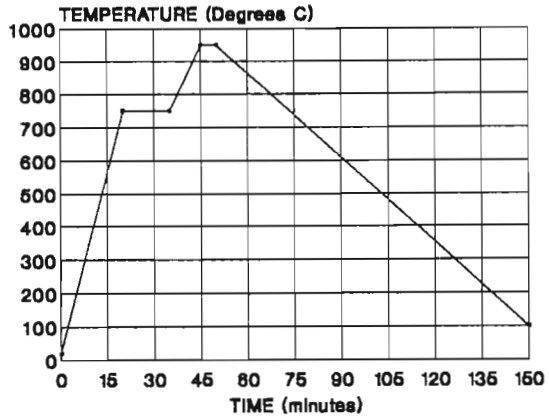

Figure 6.4 The Active Brazing Time/Temperature Profile

In fitting the electron gun, the first operation was to resistance weld the gun module (Figures 5.4 and 5.10) to the gun-mounting plate. Afterwards, the gun envelope (Figure 5.3) was electron beam welded to the plate.

The electron gun envelopes and gun modules were vacuum brazed in similar processes to that described above [9]. In a few of the electron gun envelopes, some active solder flowed to the outer edge of one or both kovar plates. If the gun envelope was welded to the gun-mounting plate or pump port structure without first removing the solder from the edge of the envelope's plates, stress corrosion cracking of the weld occurred due to intergranular penetration by silver.

The next operation in fitting a gun to a TWT was to impregnate a cathode [9]. An impregnated dispenser cathode should not be breathed on, nor should it be exposed to air for much longer than an hour. The cathode was therefore crimped into a cathode holder and fitted to the gun immediately after impregnation. Without delay, a cathode heater filament was then resistance welded in place and the pump port structure was electron beam welded to the gun envelope.

The TWT was then outgassed in a vacuum furnace for an hour at 400°C. Although heat cycling of active brazed joints can result in failure due to the exchange of O_2 and the different molar volumes of the resulting oxides [1], joints to Degussit AL-23 alumina are thermally stable and unaffected by aging at 400°C [4]. After removal from the furnace, the TWT was mounted on a vacuum pumping station and evacuated. While being evacuated to a pressure of 10^{-8} torr, the TWT was periodically heated to about 100°C to speed up the desorption of water from its internal surfaces.

6.3.1 The Joints Between the Alumina Ceramic and Molybdenum Tubes

In the structure of Figure 6.1, three joints were between 7 mm outer diameter alumina and molybdenum tubes of 1.5 and 0.5 mm wall thickness respectively. Besides being strong and vacuum tight, these joints were required to be self jigging and to have a low profile. Constraints were: the wall of the molybdenum tube was too thin to provide sufficient surface area for a reliable butt joint to the ceramic tube; the edge of the diamond cutting wheel that was available for cutting the alumina tubes was round; and the flow of CH 4 is limited (see Section 6.2).

One reason for the limited capillary action of active solders is that no further wetting can occur once the available titanium has reacted at the ceramic/solder interface. It was found that if there is sufficient active solder to provide the titanium necessary for wetting, the solder can flow about 1 mm along an alumina surface. It can also flow about 0.5 mm into 20 to 100 μm wide gaps between molybdenum and alumina surfaces.

This flow was sufficient to make the joint of Figures 6.5 and 6.6. The solder for joining the 7 mm tubes came from 6.4 by 8 mm diameter CH 4 washers of 0.2 mm thickness. It made no visible difference if the joint was brazed with the ceramic tube above or below the molybdenum one. Although each TWT was brazed in a vertical position, one test structure was brazed on its side to determine whether the effect of gravity would be noticeable. Its two joints were successful although a small bulge in the solder on the underside of each was observable.

The author believes that this annular joint design is original. Since it was not a butt joint, made under pressure, between polished parts and since it relied on capillary action, it was made by ignoring many of the recommended rules for making metal/ceramic joints with active solder. Other rules were not ignored: The coefficients of thermal expansion of molybdenum and alumina are similar and the molybdenum tube was thin enough to have some ductility. The joint was vacuum tight and strong enough to break in the ceramic and not at the metal/ceramic interface.

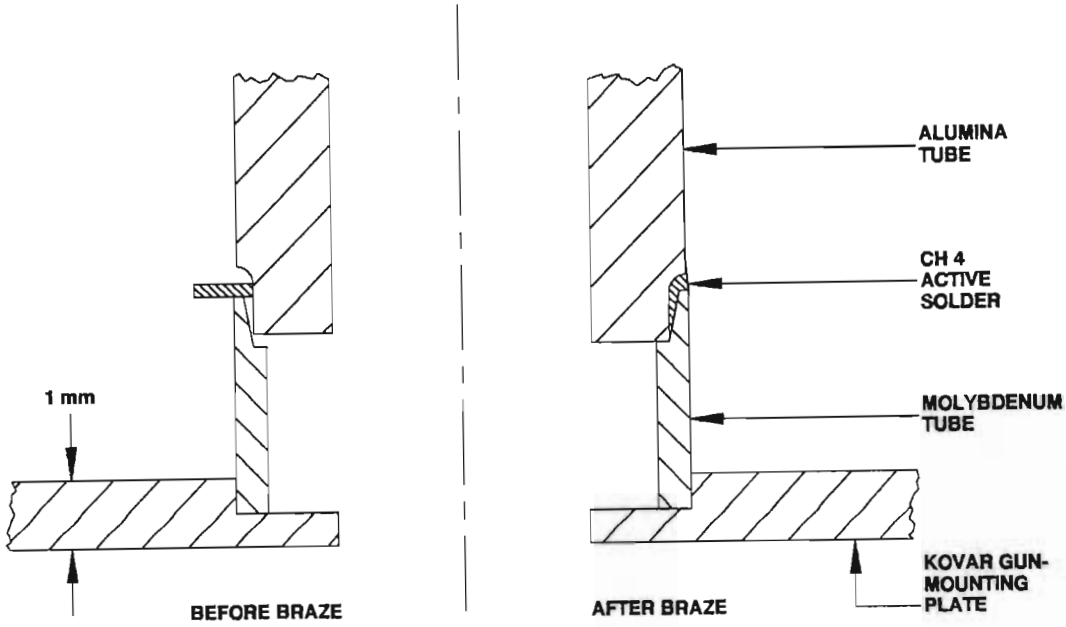

Figure 6.5 Cross Sections of the Joint between the Alumina and Molybdenum Tubes

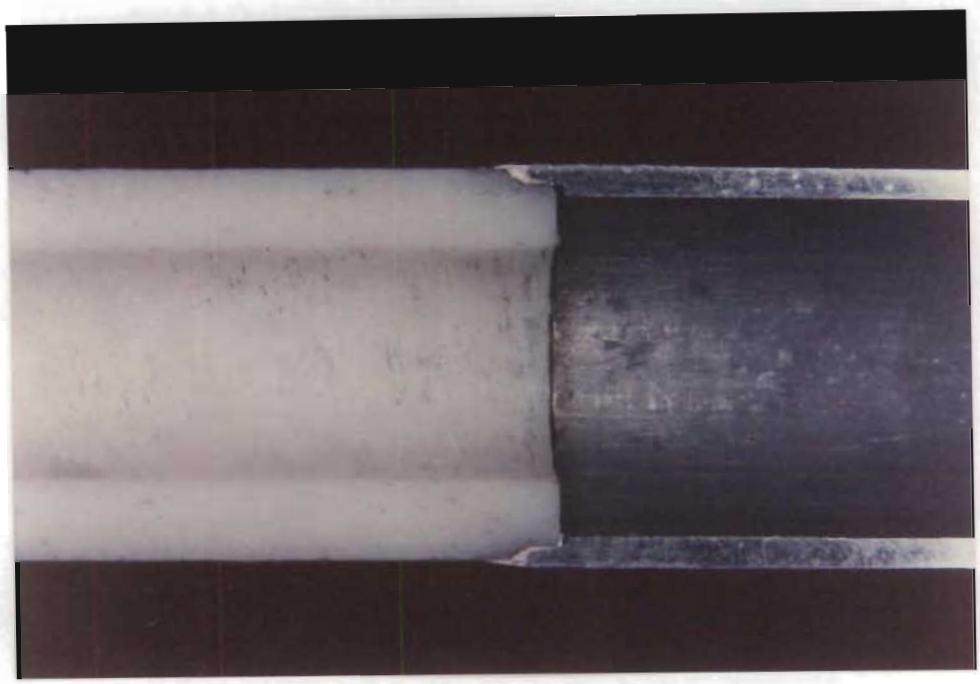

Figure 6.6 A Joint between an Alumina and a Molybdenum Tube

6.3.2 The Joint Between the Collector and a Ceramic Tube

A self jigging butt joint, illustrated in Figure 6.7, was used to join the molybdenum collector to a 4 by 7 mm diameter alumina tube. One step in the collector aligned the

collector's axis with that of the alumina tube. Another prevented the joint from closing when the active solder melted. If the joint was allowed to close, the filler layer became too thin and was not ductile enough to prevent leaks due to the thermal expansion mismatch between the non ductile parts. As in the joint between the alumina ceramic and the molybdenum tubes, this joint was not made under pressure and its parts were not lapped smooth.

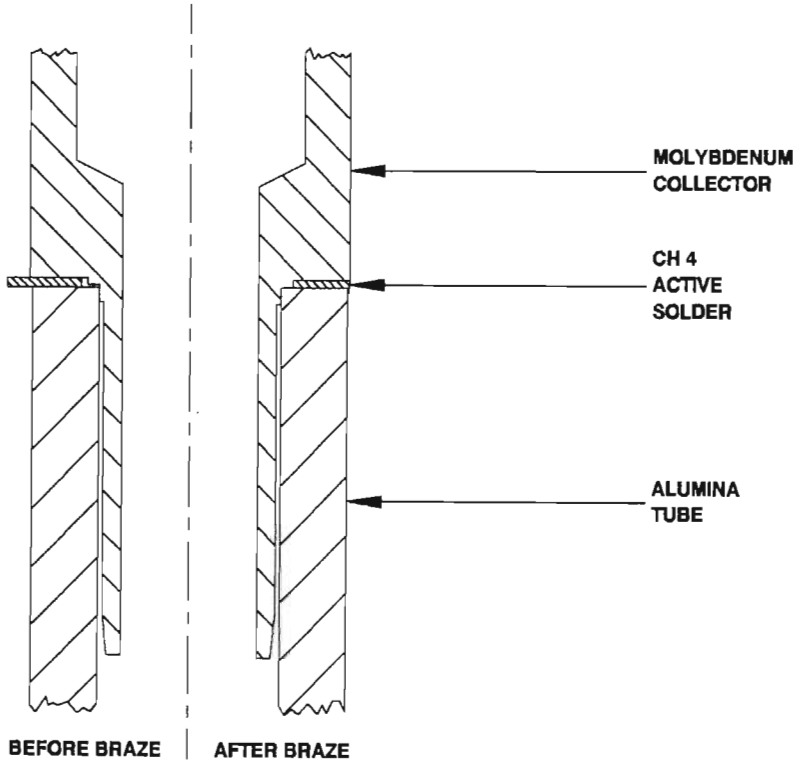

Figure 6.7 Cross Sections of the Collector/Alumina Tube Joint

6.3.3 The Ring of the Ring Transition

Cross sections of this molybdenum/alumina joint are shown in Figure 2.5. The joint was similar to the collector/alumina joint in that it was self jigging and it was prevented from closing by a step in the molybdenum ring.

6.3.4 The Plugs of the Plug Transitions

Each plug plugged a hole drilled through a ceramic tube in the vacuum envelope of a

TWT and provided a DC connection to the helix inside. Figures 6.8 and 6.9 show how the plugs of the first of three designs were made. Both figures depict joints before brazing.

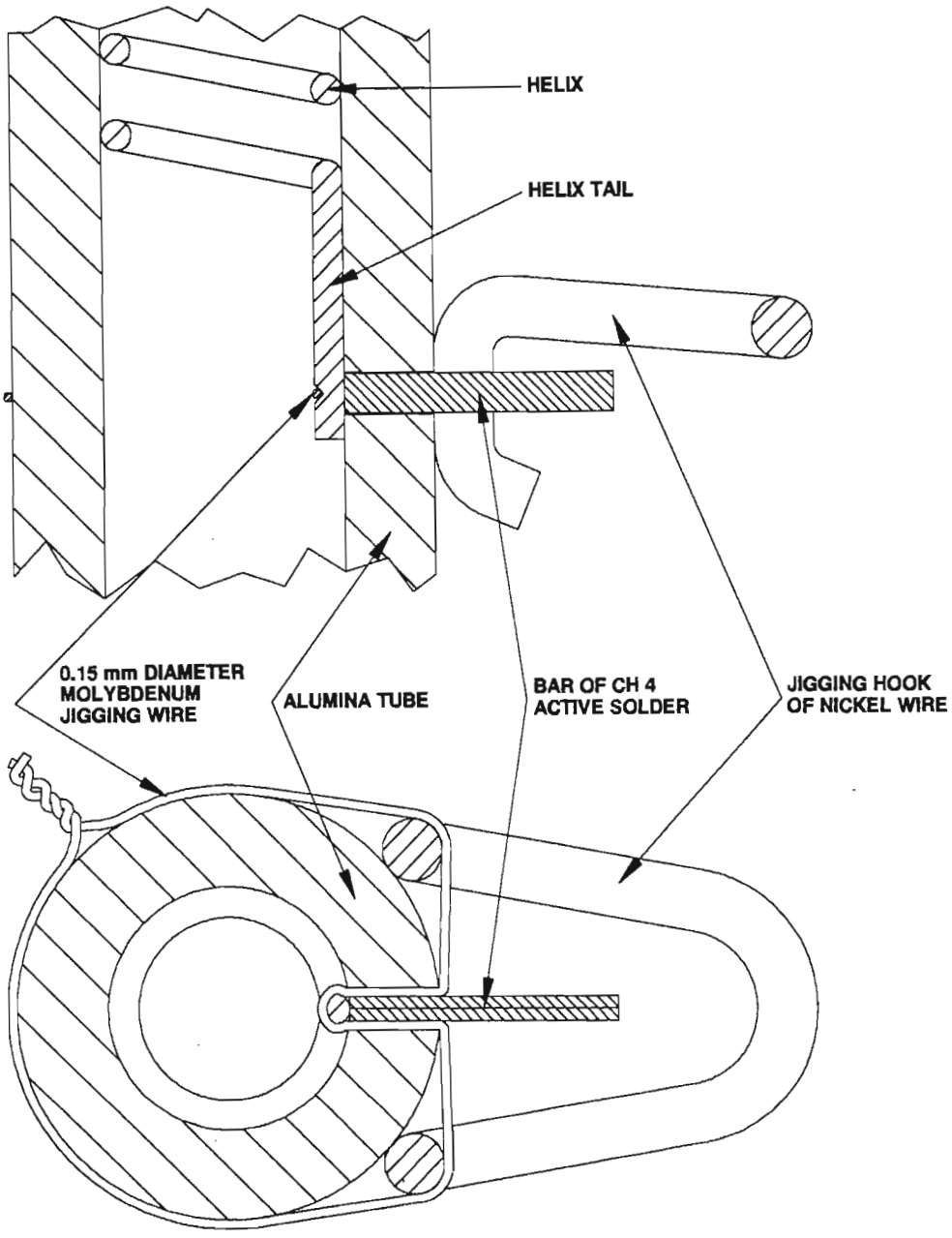

Figure 6.8 Cross Sections of a Plug Before Being Brazed

To make each plug, a folded piece of 0.15 mm diameter molybdenum wire was pushed through a 0.7 mm diameter hole that had been ultrasonically drilled through the 1.5 mm thick wall of an alumina tube. The tail of a helix was then put into the fold in the wire and the wire was pulled tight and tied around the ceramic tube. The purpose of the 0.15 mm

diameter molybdenum wire was to jig the tail in position under the hole. A notch in the tail prevented it from slipping out of the fold during TWT assembly.

A bar of CH 4 active solder was then pushed into the hole. Each bar was 4.5 mm long, 0.4 mm thick and 0.7 mm wide. It was made by resistance welding two, 0.2 mm thick, CH 4 foils together and then cutting them to size with a blade. During brazing, the bar melted, plugging the hole in the ceramic and brazing the helix tail in place. A hook of nickel wire was used to raise the molybdenum jigging wire off the outside surface of the ceramic tube and thereby prevent the active solder from sticking it to this surface.

It would have been more elegant to avoid using the jigging wire by bending the end of the tail up into the hole. Attempts to do this were however unsuccessful because the required bend in the tail was too sharp and the tungsten wire kept breaking at the bend.

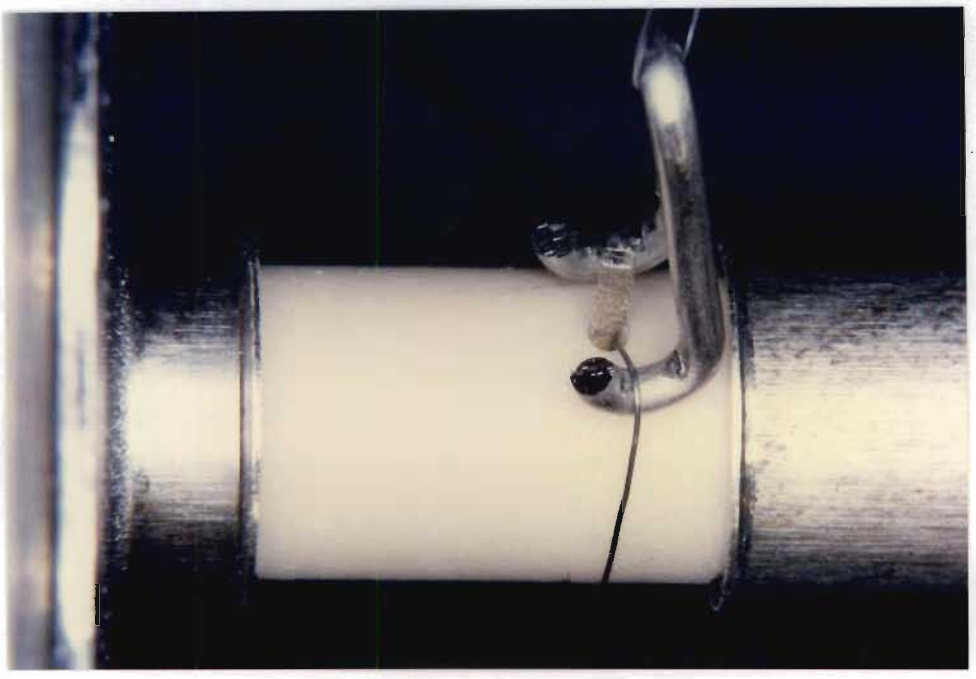

Figure 6.9 A Plug Before Being Brazed

After brazing, the hook was removed and the excess solder and protruding 0.15 mm wires were filed off with a diamond file. Each plug was filed to the contour of the ceramic tube. A magnet stack could therefore easily be slipped onto a TWT over the low profile plugs.

The joint to the helix tail was stronger than the helix but the plugs were prone to leaking.

This leaking problem was investigated by building four test structures, with 27 plugs between them. In the most successful test structure, four out of ten plugs were vacuum tight both before and after being filed.

One objective of the tests was to determine the optimum length of the CH 4 bars. Lengths that ranged from 3 to 5 mm, in 0.5 mm increments, were tried. A smaller proportion of the plugs made with longer bars leaked than of those made with shorter bars. This was because the shorter bars did not provide sufficient material to fill the holes properly. The 5 mm long bars had no advantage over the 4.5 mm bars though and a length of 4.5 mm was therefore chosen for subsequent bars.

The plugs were less prone to leaking if an outgassing period at constant temperature was included in the brazing profile (as in Figure 6.4). This reduced the amount of undesirable gases that the titanium in the solder could react with and resulted in a better joint at the solder/ceramic interface. In addition, better results were obtained for structures that were properly vented to prevent a significant difference between their internal pressure and that of the vacuum furnace. If this was not done, gases resulting from the outgassing of the inner surfaces of the structures contaminated the inner surfaces of the plugs which went black and did not wet the helix tails.

Due to thermal shock, plugs that were cooled faster after being brazed were more likely to leak. Also, more plugs leaked after being filed than before. This was due to the excess solder on the outside of an unfiled plug forming a patch over it and covering any defects.

All the leaks were at or near the solder/ceramic interface of the plugs. This was determined by leak testing with a very fine spray of helium from a long, narrow, glass capillary. The leaks were due to the mismatch in the thermal expansion coefficients of the CH 4 and the alumina. CH 4 contains 70.5 and 26.5 per cent silver and copper with three and two times the expansion coefficient of alumina respectively. The solder/ceramic interface was therefore put under tension when each joint cooled. Microcracks occurred if any part of the joint could not bear the stress. In about 90 per cent of the leaks, failure was between a 0.15 mm molybdenum wire and the wall of the hole in the ceramic tube.

The plug illustrated in Figure 6.10 was designed to increase the reliability of the joints.

Its 0.7 mm diameter hole was countersunk to a diameter of 1.3 mm and a depth of 0.5 mm. A ring of 0.3 mm diameter molybdenum wire was then inserted into the top of the hole. Molybdenum has a similar thermal expansion coefficient to alumina and the purpose of the ring was to prevent the active solder near it from pulling away from the ceramic. However, since three out of five plugs in a test structure leaked after being filed, this design was no better than the previous one.

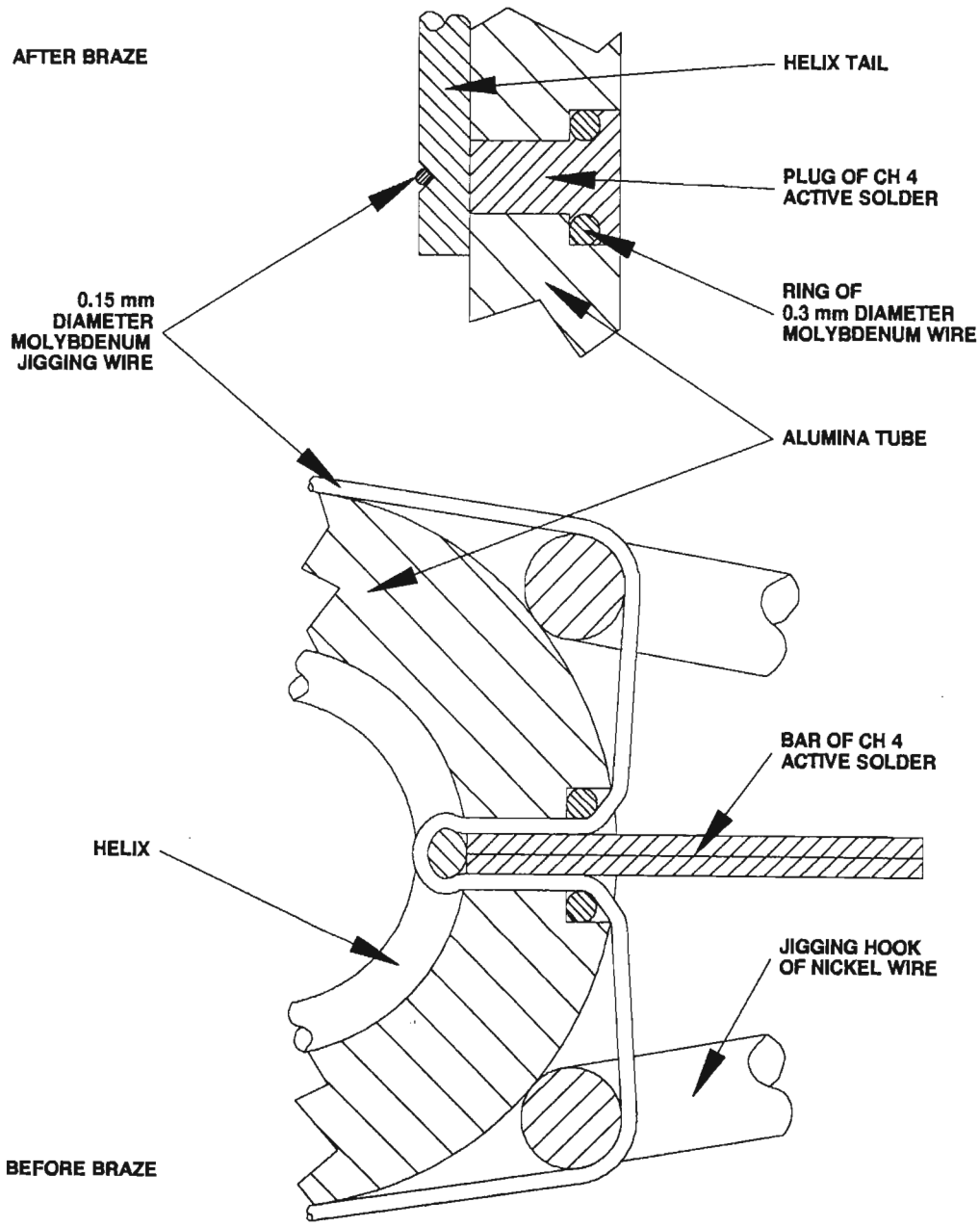

Figure 6.10 Cross Sections of a Plug in a Countersunk Hole

Two cross sections of the third plug design that was built are shown in Figure 2.11.

Helices of 2 mm inner diameter were used in this design. The ends of these helices protruded into the hole in the ceramic tube and the 0.15 mm diameter molybdenum jigging wire was therefore not needed.

Each helix end protruded 0.5 mm into a hole. The CH 4 bar that was used to make these plugs was therefore 0.5 mm shorter than in the two earlier designs. This bar was pushed 1 mm into the hole until it touched the end of the helix. A 4.5 mm long sliver of CH 4 was then pushed alongside and past the bar until its end protruded into the ceramic tube. This end was then bent against the end of the helix. The sliver had three functions: it helped to jam the bar of CH 4 in the hole; it ensured that the bar would wet the end of the helix; and it provided more filler material with which to plug the hole. Figure 6.11 shows one of these plugs after being brazed but before being filed. Although there was no molybdenum wire to weaken the solder/ceramic joint, this design did not result in a reliable vacuum seal and only one of the four plugs that were made did not leak after being filed.

Figure 6.11 A Plug Made without Molybdenum Jigging Wire

Further research is needed to develop plugs that are more consistently vacuum tight than those of the three designs discussed here. Fortunately, this research was not a prerequisite for the building and testing of the experimental low profile TWTs. Their evacuation to pressures of the order of 10^{-8} torr was possible by painting any such small

leaks with a commercial leak sealing compound that was available.

6.4 CONCLUSIONS

The limited flow of CH 4 active solder can be relied upon to make a joint as long as the solder is not required to flow more than 1 mm along an alumina ceramic surface and more than 0.5 mm into a 20 to 100 μm wide gap between molybdenum and alumina surfaces. This limited flow requires sufficient active solder to be present to provide the titanium necessary for reaction at the solder/alumina interface.

It was not necessary that molybdenum/alumina joints made with CH 4 active solder be made under pressure. Vacuum-tight joints were possible as long as the active solder was in contact with both the metal and the ceramic part.

It was difficult to make vacuum-tight plugs in holes in alumina ceramic using only CH 4 active solder as the plug. The coefficient of thermal expansion of the solder was higher than that of the ceramic and the CH 4 pulled away from the ceramic upon cooling.

Although some leaks resulted, a TWT could be reheated to beyond the melting point of the CH 4 active solder that it was joined with and still be strong enough to withstand the stresses resulting from the fitting of its magnet stack and water-cooling system.

Gold flows readily on molybdenum and constituents of CH 4 active solder flow more readily along the surface of gold plated molybdenum than pure molybdenum. This can result in poor or even ruined molybdenum/alumina joints.

Stress corrosion cracking of welded kovar parts can result from contamination of the kovar parts by the silver from an active-brazed joint. These cracks can result in a large leak in a vacuum system.

REFERENCES

[1] W.H. Kohl, *Materials and Techniques for Electron Tubes*, Reinhold Publishing Corporation, Chapter 14, 1960.

[2] M.G. Nicholas, T.M. Valentine and M.J. Waite, "The Wetting of Alumina by Copper Alloyed with Titanium and Other Elements", *Journal of Materials Science*, Vol. 15, pp. 2197 to 2206, 1980.

[3] W. Weise, W. Malikowski and W. Böhm, "Verbinden von Keramik mit Keramik oder Metall durch Aktivlöten unter Argon oder Vakuum", *Degussa Aktuell*, Hanau, FRG, 1986.

[4] A.J. Moorhead and M.L. Santella, "The Effect of Interfacial Reactions on the Mechanical Properties of Oxide Ceramic Brazements", *Proceedings of the BABS 5th International Conference on High Technology Joining*, Brighton, Paper No. 22, November 1987.

[5] E. Lugscheider and M. Boretius, "Active Brazing of Silicon-Carbide and Silicon-Nitride to Steel Using a Thermal-Stress Reducing Metallic Interlayer", *Proceedings of the 3rd International Conference on Joining Ceramics, Glass and Metal*, Bad Nauheim (FRG), April 1989.

[6] W. Weise, W. Malikowski and H. Krappitz, "Wetting and Strength Properties of Ceramic to Metal Joints Brazed with Active Filler Metals Depending on Brazing Conditions and Joint Geometry", *Proceedings of the 3rd International Conference on Joining Ceramics, Glass and Metal*, Bad Nauheim (FRG), April 1989.

[7] N.P. Hensley, *The Construction and Testing of an Experimental Travelling Wave Tube Amplifier*, M.Sc. Thesis, Department of Electronic Engineering, University of Natal, January 1990.

[8] *Degussa sets the standards. For example: active Solders*, Two-page advertising pamphlet from Degussa AG, Date unknown.

[9] B.D. Foulis, *A Gridless, Variable Perveance, Pierce Electron Gun*, Ph.D. Thesis, University of Natal, 1994.

CHAPTER 7

AUTOMATED TESTING OF TWTs

7.1 INTRODUCTION

Several variables were required to be measured while testing an experimental TWT. Many of these variables then had to be processed to make them more meaningful. Furthermore, the measured data often needed to be recorded for subsequent analysis. These tasks were carried out quickly and repeatedly by a personal computer that collected data from several Hewlett-Packard instruments via HP-IB interfaces. The measured variables were displayed simultaneously on the computer's monitor, allowing the operation of the TWT being tested to be assessed easily.

Either of two circuit configurations could be used to measure RF characteristics of TWTs. In the open loop configuration, the input signal of the TWT was from an oscillator. In the closed loop configuration, the input signal of the TWT came from its output. In this configuration, both the gain and the saturated output power of the oscillating amplifier could be measured by controlling the frequency and amplitude of the feedback signal. The RF test circuit therefore included a tuned resonator, adjusted by stepper motor, and programmable step attenuators.

7.2 SYSTEM OVERVIEW

The automated TWT test station that was built is shown in Figure 7.1. A TWT is mounted above the 520 mm diameter stainless steel plate that is near the centre of the photograph. This plate is part of the Materials Science Laboratory's main pumping station that could evacuate a tube to a pressure of 10^{-8} torr. To the left of the vacuum plant is an HP8690B sweep oscillator, used to provide open loop TWT input signals. An HP8566B spectrum analyzer, on the trolley in front of the oscillator, was used to examine the output spectrum of a TWT. Semi-rigid coaxial cables connected the spectrum analyzer's input, the sweep oscillator's output and the input and output ports of the TWT to the RF test circuit assembly, mounted above the oscillator. The test station was controlled from the console in the right hand half of Figure 7.1.

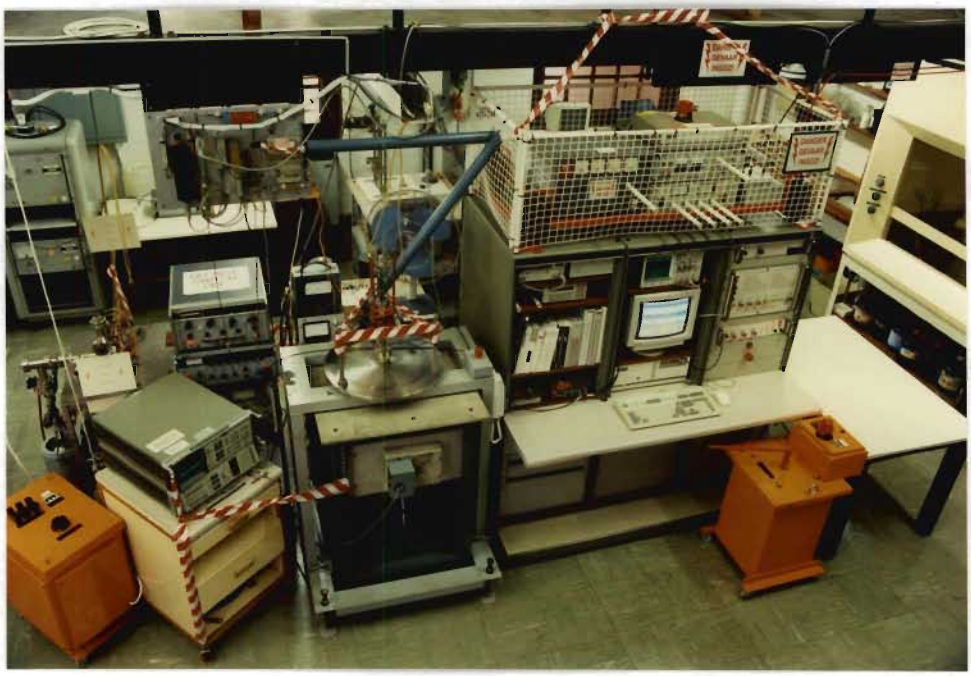

Figure 7.1 The Automated Test Station

The console was housed in a wheeled cabinet of three 19 inch racks, each supplied by a different mains phase and cooled by a 9 inch fan. An insulated platform was built on top of the cabinet. Any power supplies or instruments that were required to float at cathode potential were put onto this platform and were powered by a mains isolation transformer that was insulated to 30 kV and mounted inside the cabinet. Manual adjustment of the power supply control potentiometers was by insulated knobs made from 250 mm lengths of PVC conduit.

A block diagram of the measurement system is presented in Figure 7.2. Automated control was by a 33 MHz, 80486 personal computer (PC) that was mounted in the middle of the console. Control was through both an HP-IB interface and a PC-30 analogue to digital and digital to analogue conversion card. The control code was written using the software packages "Hewlett-Packard Interactive Test Generator II" and "Hewlett-Packard Instrument BASIC for Windows". A 213 MByte hard drive was fitted to the PC. This provided ample memory for program and data storage.

The spectrum analyzer and the following instruments were connected directly to the computer's HP-IB interface: an HP437B power meter, used to measure average TWT output power; an HP54601A four channel oscilloscope, used to measure several

voltages; an HP3478A multimeter, used to measure average collector current; and an HP37203A HP-IB extender. The extender was connected by fibre-optics to another HP37203A on the insulated platform. The HP-IB extenders formed a transparent link between the computer, at ground potential, and an HP3421A data acquisition/control unit at cathode potential.

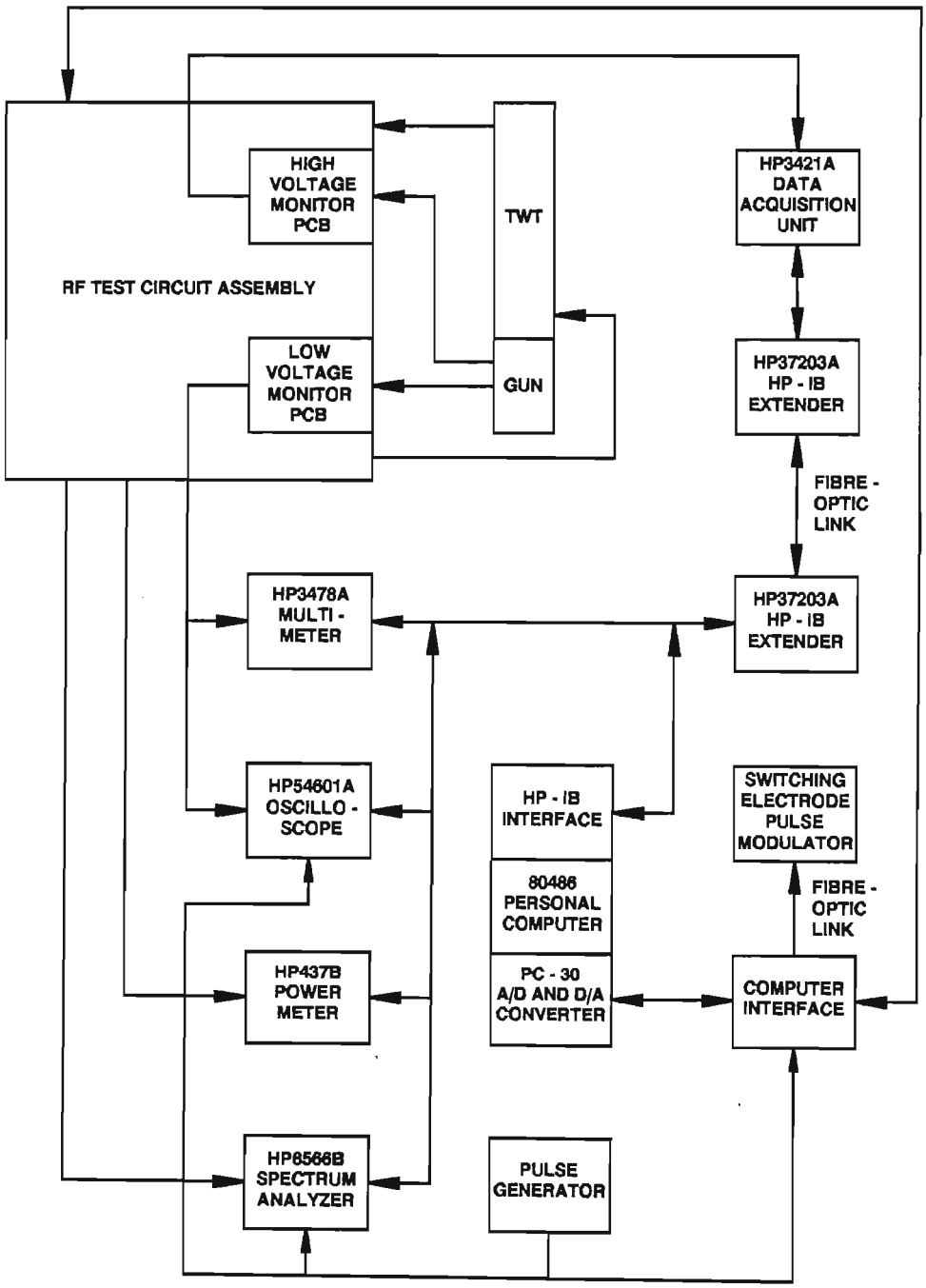

Figure 7.2 A Block Diagram of the Measurement System

The HP3421A measured several voltages and currents that had been converted to

voltages suitable for the instrument by a printed circuit board (PCB) mounted on insulating posts on the RF test circuit assembly. The oscilloscope and multimeter measured voltages that had been similarly converted on another PCB at ground potential.

The relays and stepper motor of the RF test circuit assembly were computer-driven via the PC-30 and a custom-built computer interface [1]. This interface was also used to control the open/closed loop microwave switch of the RF test circuit. In addition, it controlled the switching electrode pulse modulator via fibre-optics (this modulator was designed together with Reynolds and is described in his thesis [1]). The pulse modulator could be used to operate the TWT in either pulsed, continuous or cut-off mode.

7.3 DC MEASUREMENTS

A schematic of the TWT test circuit is shown in Figure 7.3. The cathode power supply consisted of a step-up transformer and a rectifier. The three phase ripple on the rectified voltage was reduced by a 6.5 μF capacitor bank. Damaging capacitor discharges into a TWT during any possible arcs in its gun were prevented by a 200 W, 10 kΩ resistor that was connected in series with the cathode power supply. The rectifier voltage could be adjusted from 0 to 20 kV by the orange-painted variac on the right hand side of Figure 7.1 but TWT test voltages were not required to exceed 6000 V. The typical cathode voltage was 4500 V below anode potential.

Two series-connected power supplies, with maximum output voltages of 2000 and 300 V respectively, were used to provide the switching electrode bias of typically 1125 V above cathode potential. The 300 V supply was needed because the other was only adjustable in 200 V steps.

The heater filament was held at cathode potential by a 1000 Ω resistor and not by a direct connection. If a poorly aligned heater filament touched the cathode structure, this resistor would prevent part of the filament from being shorted out.

The heater filament voltage was measured directly by the HP3421A data acquisition/control unit but a pair of frequency-compensated 1000:1 attenuators [1] were

used to step down the cathode and switching electrode voltages for measurement. Current monitoring was by measurement of the voltages across one 0.1 Ω and several 100 Ω series resistors.

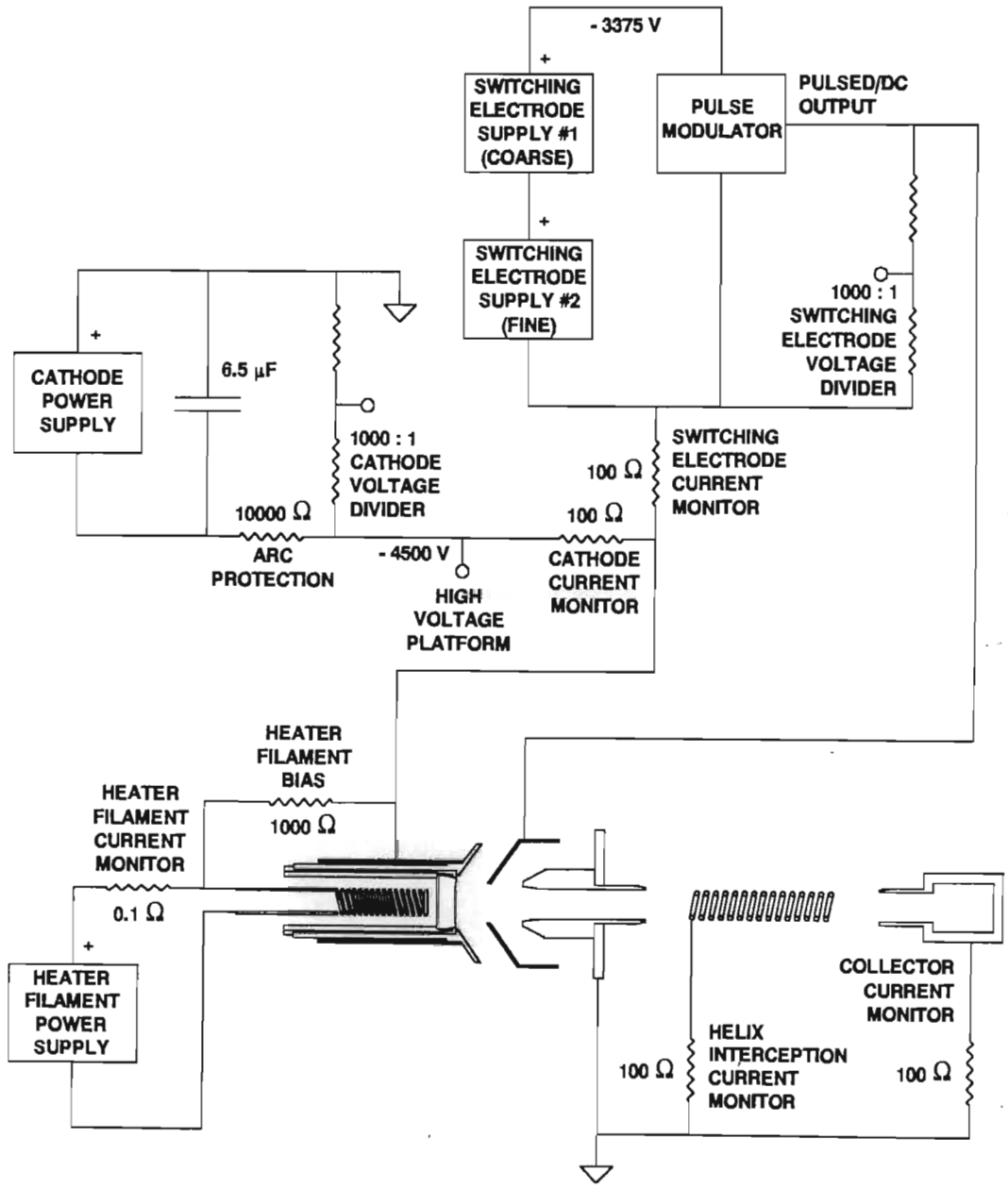

Figure 7.3 A Schematic of the TWT Test Circuit

7.4 RF MEASUREMENTS

Most of the components of the RF test circuit were mounted on the aluminium plate shown in Figure 7.4. This plate was positioned near the TWT being tested to reduce the

length of the RF cables that connected it to the TWT. A block diagram of the RF test circuit is shown in Figure 7.5.

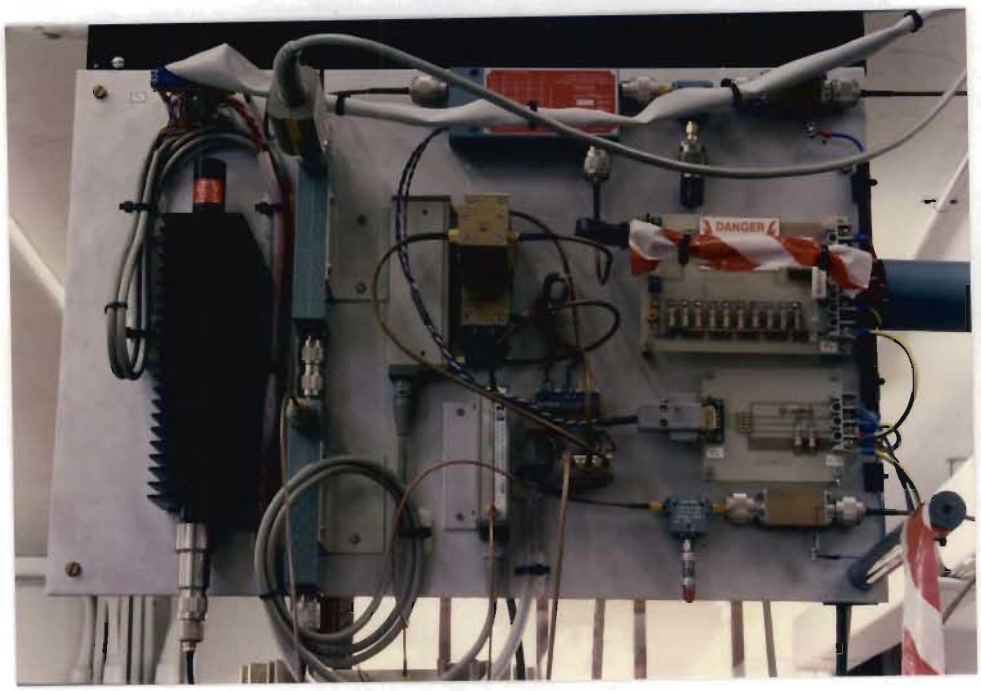

Figure 7.4 The RF Test Circuit Assembly

The TWT input and output cables were each connected to the test circuit through a bias tee [1]. The function of the two bias tees was to protect the RF test equipment from any DC offset on the helix and to allow the helix current to be monitored. The bias tees were mounted in the right hand corners of the test circuit assembly, as shown in Figure 7.4. Return losses of better than 17 dB, over a 4 to 8 GHz band, were measured for the bias tees [1].

A ferrite circulator, with a 4 to 8 GHz bandwidth, was connected to each bias tee. The signal paths through each circulator were from ports 1 to 2, 2 to 3 and 3 to 1. The function of each circulator was to direct reflected signals into a matched load.

After passing through a bias tee and a circulator, the output signal of a TWT was conducted into a high-power matched load via three directional couplers. Each coupler had a 4 to 10 GHz bandwidth. Two 30 dB couplers tapped off signals for the spectrum analyzer and the power meter and a 10 dB coupler provided the feedback signal needed for closed loop operation of a TWT.

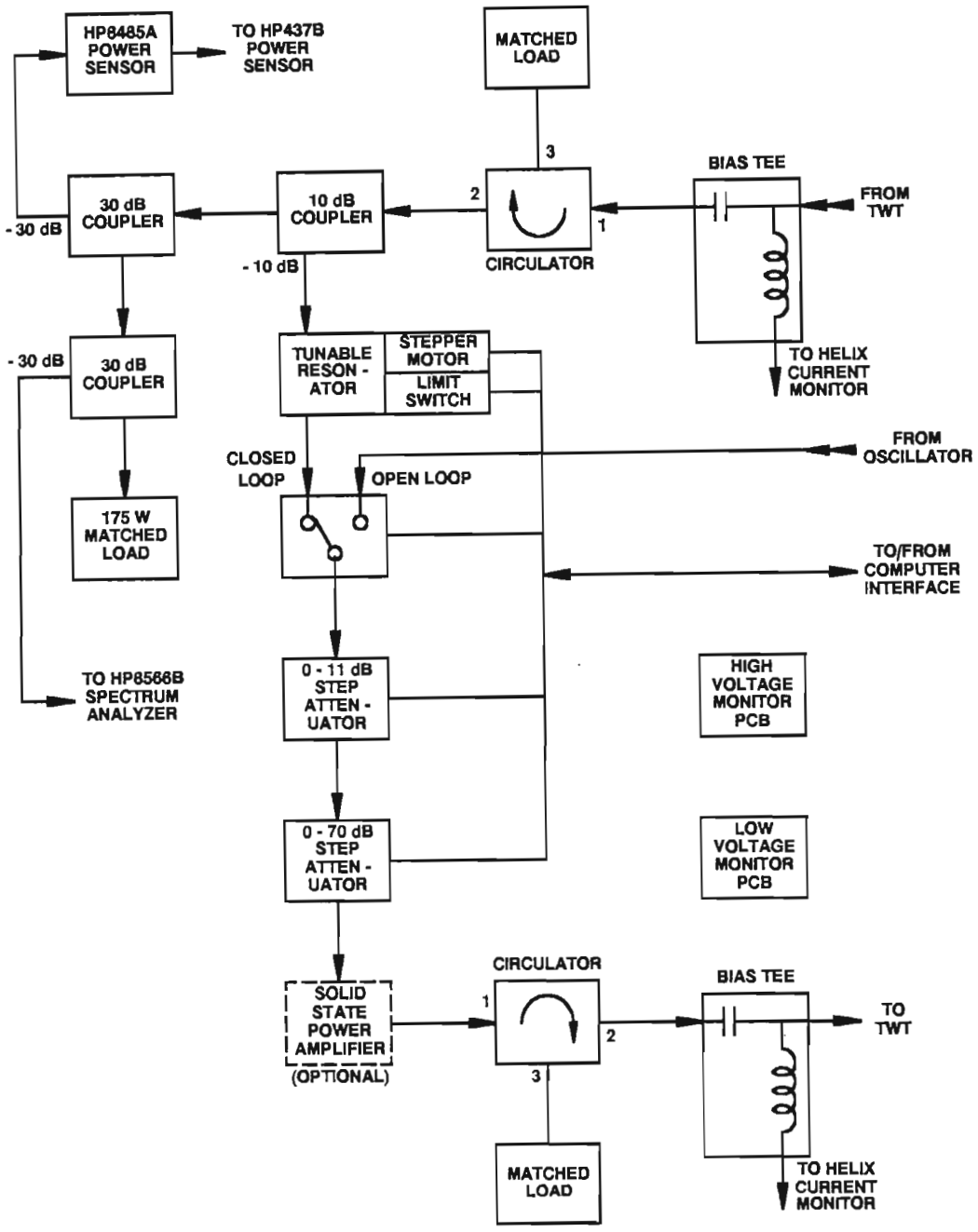

Figure 7.5 A Block Diagram of the RF Test Circuit

Frequency selection of the feedback signal was by the tunable half-wave resonator described in Section 7.4.1. Tuning was by stepper motor adjustment of the resonant cavity length. A limit switch was used to provide a zero reference for the stepper motor.

After passing through the resonator, the feedback signal passed through a microwave switch and into a pair of programmable step attenuators that could be adjusted from 0 to 81 dB in 1 dB steps. The frequency- and amplitude-controlled feedback signal then

passed through a circulator and a bias tee before going to the TWT input. Since the loop gain of an oscillator circuit is unity, the gain of an oscillating TWT was equal to the loss in its feedback circuit path.

The closed loop could be broken by the microwave switch to allow open loop signals to be inserted. The signals were provided by either an HP8690B sweep generator, which could produce an 11 to 16 dBm signal and was tunable from 3.8 to 7.8 GHz, or a dielectric resonator that produced a 7.1 GHz signal at 13.5 dBm. An optional solid state power amplifier could be used to increase the amplitude of the TWT input signal and saturate the TWT. In the closed loop configuration the power amplifier allowed for low TWT gains or passive device losses to be measured.

7.4.1 The Tunable Half-Wave Resonator

The tunable half-wave resonator, shown in Figure 7.6, was mounted in the centre of the RF test circuit assembly. A cross section of the RF portion of the resonator is shown in Figure 7.7. Tuning of the coaxial resonant cavity was by variation of its length. One end was short circuited by a fixed short, the other by a sliding short. Both shorts are shown in Figure 7.8. The fixed short was soldered to the centre conductor and used six sprung fingers to make a low leakage RF short circuit between the centre conductor and the cavity wall. The sliding short had two sets of such fingers. The fingers were used for two reasons: their springiness ensured good electrical contact; and their length put the points of electrical contact some distance away from the ends of the cavity and hence in a region of lower RF current.

The fundamental, half-wave resonance could be tuned from 4 to 10 GHz and its transmission through the resonator was as shown in Figure 7.9. The full-wave resonance harmonic was transmitted more strongly through the resonator but was attenuated in the RF test circuit by the circulators and the 10 dB coupler that had upper band limits of 8 and 10 GHz respectively.

When the brass resonator parts were polished smooth, the cavity had a quality factor (Q) of 200 to 400. The parts were silver plated with the aim of increasing the Q but were polished back down to brass when the opposite effect was observed. Each electric field

probe protruded into the cavity by the same amount. This depth, determined experimentally, yielded both a good Q and good transmission. Inserting the probes deeper increased transmission but reduced the Q. Any withdrawal of the probes reduced transmission without significantly increasing the Q.

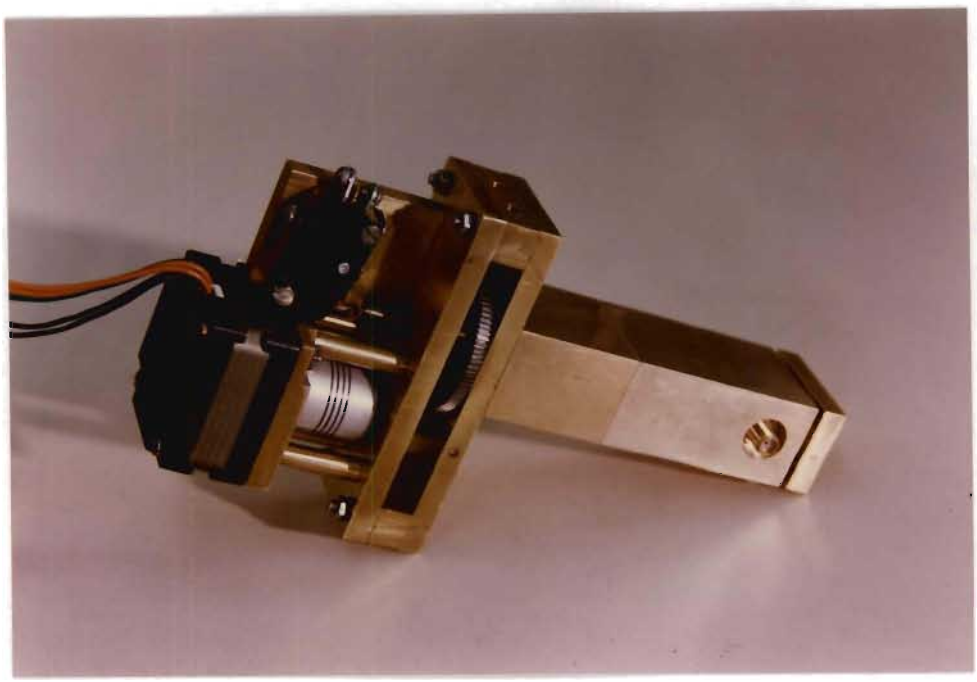

Figure 7.6 The Tunable Coaxial Cavity Resonator

If its sprung fingers pressed against the cavity surfaces with too much force, the sliding short would become increasingly more difficult to push into and pull out of the cavity. This was due to brass filings that were produced by friction. If the fingers were bent to reduce their contact pressure, the problem was eliminated but a significant reduction in Q resulted. The stiffening was eliminated by carefully setting the pressure and by using some vacuum grease as a lubricant. Fortunately, the cavity Q was not reduced by the grease which had an unknown loss tangent.

Below 5 GHz, transmission was lower because the electric field probes were relatively far from the middle of the cavity where the electric field maximum of the fundamental mode occurred. In addition, transmission was less repeatable in this range because of a slight ripple in the cavity wall that resulted in poor electrical contact with the outer fingers of the sliding short.

The sliding short was driven by a stepper motor and a gearbox. Backlash was avoided

by always driving the short in same direction when tuning and a limit switch provided the zero reference from which the number of stepper motor steps were counted. The resonant frequency was related to the number of steps by an equation that was fitted to an empirically derived calibration table.

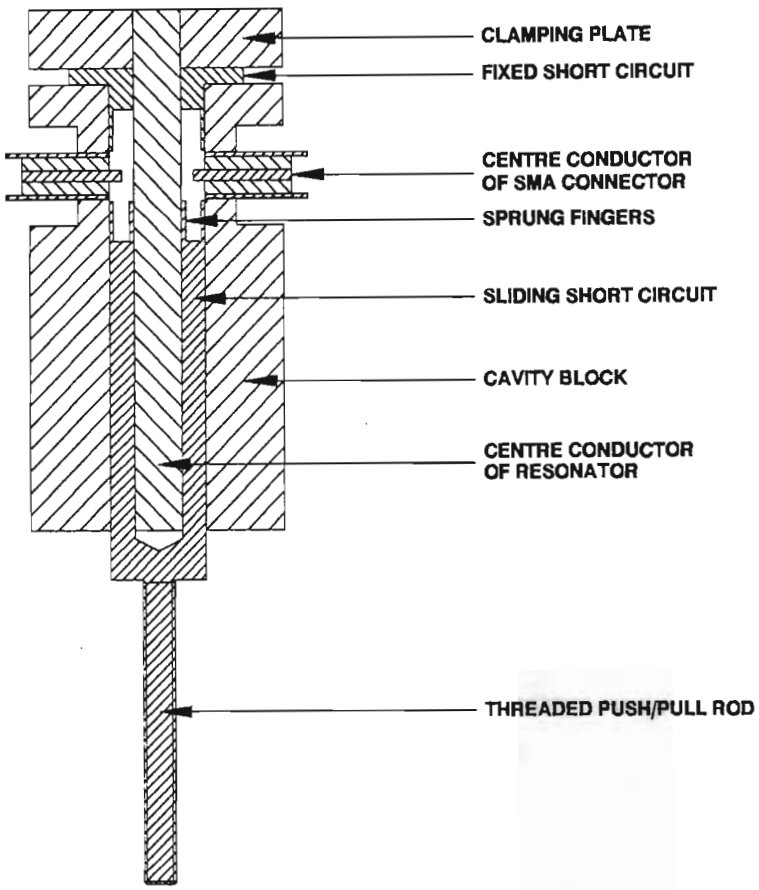

Figure 7.7 A Cross Sectional Schematic of the RF Section of the Coaxial Cavity Resonator

7.4.2 RF Test Circuit Calibration

Both the open and the closed loop calibration of the RF circuit was done using the HP8510B network analyzer. In addition, if the optional solid state amplifier was used, the closed loop circuit could calibrate itself. This was done by connecting the TWT input and output cables together and reducing the step attenuator setting until the circuit began to oscillate. A measurement was made every 50 MHz and the attenuator setting for each resonator frequency was then tabulated. The gain of a device under test (DUT) connected between the TWT input and output cables was easy to calculate. It was

simply the difference between its attenuator setting at the onset of oscillation and the tabulated value.

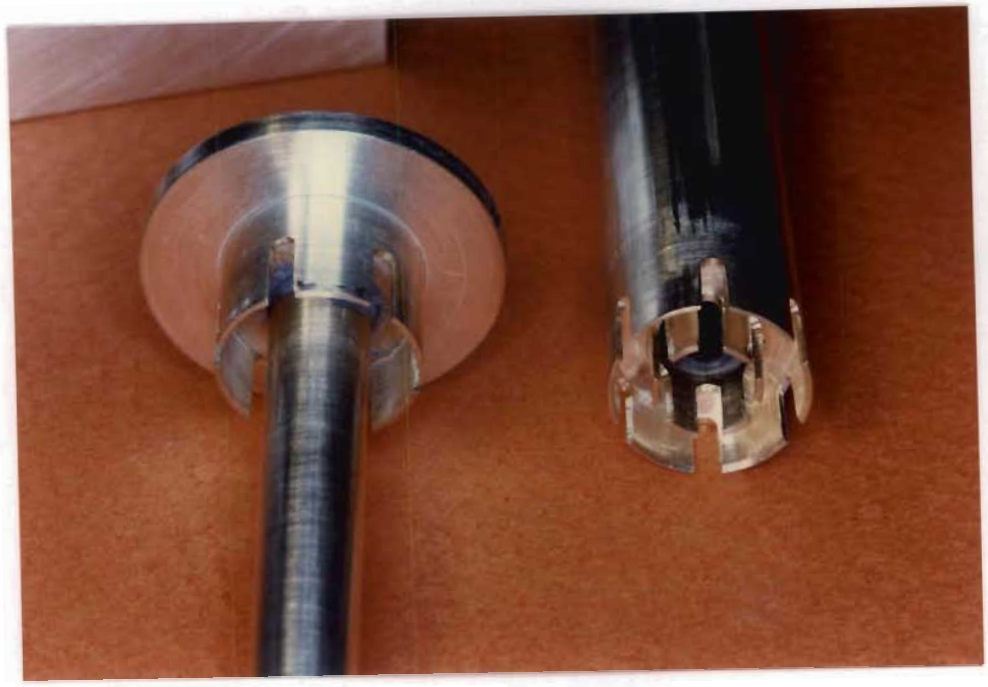

Figure 7.8 The Fixed and Sliding Short Circuits of the Resonator

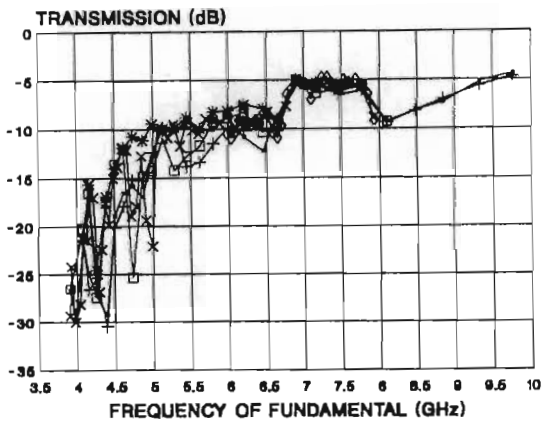

Figure 7.9 The Transmission of the Fundamental Frequency Through the Half-Wave Resonator

The closed loop calibration was checked by measuring the "gain" of a 5 dB attenuator. The average measured attenuation, plotted in Figure 7.10, was indeed 5 dB but an apparent attenuation ripple of 4 dB peak was also measured.

This ripple was due to the phase requirements for oscillation and the slope of the passband of the tunable half-wave resonator. The phase shift around the feedback loop

was a function of the DUT and of the step attenuator setting. At each resonator setting, the feedback frequency for which this phase shift was a multiple of 360° therefore varied for different DUTs. The loss around the feedback circuit depended on the difference between the feedback frequency and the resonator centre frequency and on the slope of the resonator's passband. Closed loop gain measurements were therefore not exact.

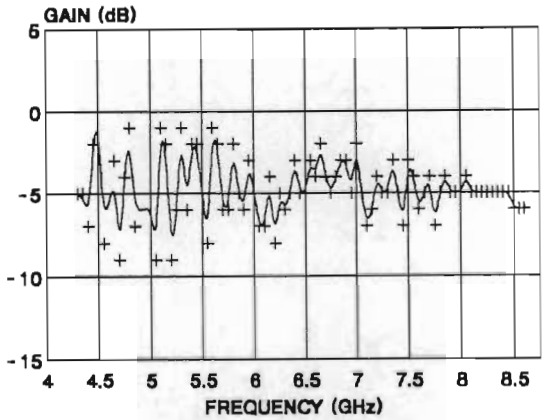

Figure 7.10 RF Test Circuit Calibration Check using a 5 dB Attenuator

7.5 SOFTWARE

The computer program that controlled the measurement system was developed with the software packages "Hewlett-Packard Interactive Test Generator II" (HP ITG II) and "Hewlett-Packard Instrument BASIC for Windows". HP ITG II is a powerful package that allows the quick generation of programs for controlling instruments and analyzing and displaying measured data. Customised, on-screen control panels of buttons, meters, bar graphs and other "widgets" are easily set up. HP ITG II contains an extensive library of Hewlett-Packard instruments for which it automatically writes the HP-IB code needed to control them. To write this code, the user simply uses a mouse to interact with the soft, on-screen, front panels of the instruments in the test system. The user then builds the rest of the test program around these commands.

HP ITG II can work with HP Instrument BASIC and Microsoft C, Quick C and Quick BASIC. HP Instrument BASIC was used. The advantage of using a BASIC interpreter is that BASIC programs can be run immediately after being edited and no time is wasted compiling them. Although BASIC programs run slowly when compared to compiled programs, they still run fast enough to have to spend much of their time waiting for the instruments of an automated test station such as the one described here.

A simple block diagram of the control program is presented in Figure 7.11. The program started by initializing the system hardware (HP-IB instruments, PC-30 card, PC-30 controlled hardware), the program variables and the computer monitor display (menus, analogue meters and digital readouts).

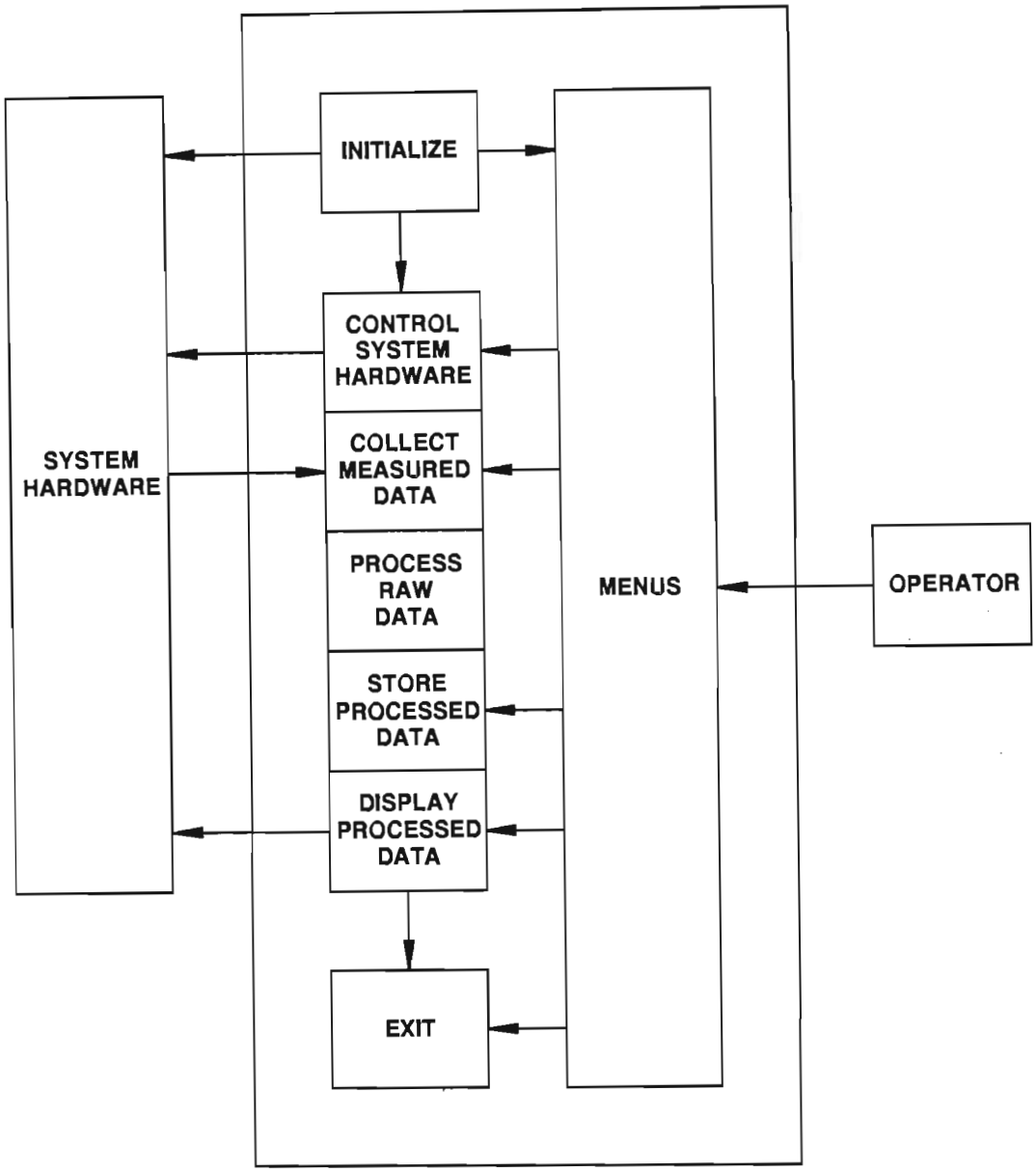

Figure 7.11 A Block Diagram of the Test Program

The main program loop controlled the system hardware and read the data it measured. It processed the raw data and temporarily or permanently stored the processed data. It also displayed processed data on the analogue meters and digital readouts on the computer's monitor. If maximum safe levels were exceeded, it sounded alarms.

The details of the above functions could be altered from menus that allowed control of the TWT, the test circuit and the measurements. Some of the things that could be controlled are: the data logging methods; the step attenuator range/setting; the resonator frequency range/setting; the electron gun mode (pulsed/CW/cut-off); and the test circuit configuration (open/closed loop).

7.6 SAFETY

Being electrically shocked by the high voltage power supplies used to test the low profile TWTs would probably have been lethal. Several safety measures were therefore taken to reduce the probability of such an accident.

Flashing red beacons were placed on the highest and most visible point on the high voltage platform and on the cathode power supply's variac as electrocution danger warnings. Several red-on-white danger decals, larger danger signs and barrier tapes were positioned where they could be seen immediately upon entering the Laboratory and upon approaching any live equipment.

The high voltage platform was behind a clearly visible PVC mesh and positioned relatively high-up on top of the cabinet to reduce the chances of it being accidentally touched. Well insulated high tension cables were used wherever possible and most high voltage cables were inside PVC pipes. In addition, a PVC guard was built around the electron gun to insulate the gun electrode pins. Operators were required to wear suitable footwear and were advised not to operate the system when alone.

In the event of an emergency, either one of two large, red, emergency-stop buttons could be pressed. One was located on a cabinet front panel on the computer operator's right-hand side and the other was on a portable unit which was normally situated on the right-hand side of the TWT under test. Pressing either button would switch two 3-phase relays, disconnecting the mains supply from the cathode supply's variac and from the switching electrode power supplies. A purpose-built high voltage relay would simultaneously discharge the cathode supply's capacitor bank through a 3 kΩ load. The relays would latch in this position until the depressed emergency-stop button was reset and a reset button was then pressed to unlatch the relays.

REFERENCES

[1] C.G. Reynolds, *The Analysis, Simulation and Testing of an Experimental Travelling-Wave Tube*, Ph.D. Thesis, Department of Electronic Engineering, University of Natal, 1994.

CHAPTER 8

RF PERFORMANCE OF OPERATIONAL LOW PROFILE TWTs

8.1 INTRODUCTION

The RF performance of the two low profile TWTs that were tested with fully operational electron guns is discussed. Since these tubes were merely prototype technology demonstrators, only their RF gain, output power and stability were investigated. Aspects such as efficiency, phase shift, noise, signal intermodulation or distortion were not examined (nor indeed were more general TWT attributes such as lifetime, reliability or ruggedness).

8.2 TWT LP8, THE FIRST OPERATIONAL LOW PROFILE TWT

Simulated and measured gain versus frequency curves for TWT LP8 [1] are presented in Figure 8.1. The simulation was made using Pierce's small-signal gain theory. To approximate the effect of the attenuator, a value of 6 dB [2] was subtracted from the gain that was calculated by the method in Section A.3. The non-optimized gain was measured at a beam current of 77 mA and fixed cathode-to-anode and cathode-to-switching electrode voltages of 4600 and 1200 V respectively. The gain was optimized at each test frequency by shifting the gun potentials about these values to adjust the beam synchronism and focusing.

Some gain optimization was also possible by adjustment of the mean radius of the beam. The beam radius, and therefore the helix interception, was increased by using magnetic shunts to reduce the axial field of the PPM stack. At six test frequencies, an average gain variation of 4 dB was measured as the helix interception was varied between 1 and 10 mA of a 77 mA beam. The optimum helix interception differed for each frequency however and no value of interception resulted in more gain at all the test frequencies. The minimum interception was therefore chosen.

The measured gain was 20 to 30 dB lower than that simulated. This difference is discussed in Section 8.4.

The simulated gain curve suggests that the TWT would have exhibited gain at frequencies lower than those in the octave measured. This was not confirmed by measurement since neither the HP8690B sweep oscillator, used to provide the TWT input signal, nor the RF test circuit was suitable for frequencies lower than 3.8 GHz.

Figure 8.2 shows the results of a saturation test that was made at 4.1 GHz. The maximum saturated RF output power was 42.3 dBm (17 W) and saturation, indicated by a reduction in gain, was evident for output powers greater than 35 dBm. Saturation results partly from intense bunching of a tube's electron beam. Since higher density electron bunches are more difficult to focus than those of lower density, the increased helix interception, shown in Figure 8.2, resulted during saturation.

TWT LP8 was on the verge of instability at and near a beam voltage of 4600 V. Particular accelerating voltages would result in up to about forty spectral lines across the tube's band, other voltages in none. This voltage dependence was a result of the sensitivity of the phase of a TWT's output signal to its beam voltage. As the phase of the output signals varied, so did the oscillation-determining phase of the internal feedback signals in the tube.

The total measured RF output power due to instability was usually between 20 and 30 dBm. If the matched load was removed from the output circulator in the TWT RF test circuit, more reflections of the output signal occurred and the TWT oscillated more heavily, producing about 38 dBm of RF power.

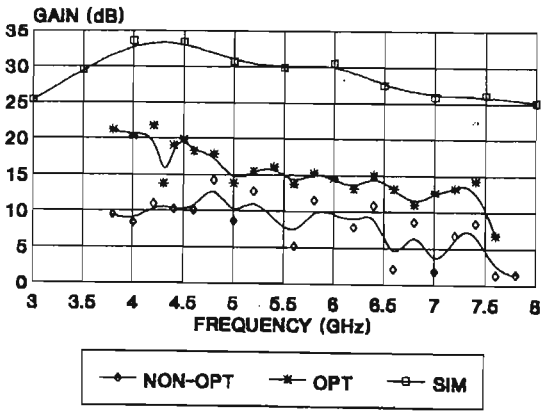

Figure 8.1 Measured (gun optimized and not optimized for maximum gain) and Simulated Gain

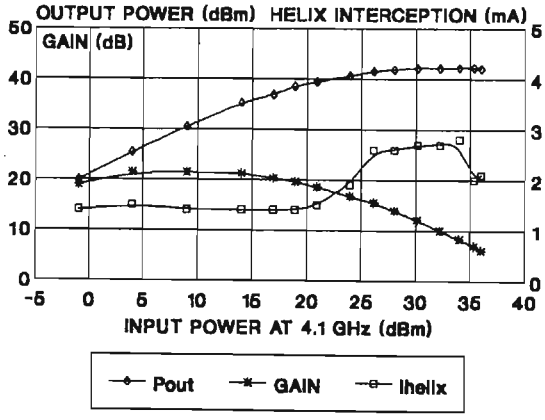

Figure 8.2 Saturation Test Results

TWT LP8 was unstable because its attenuator did not sufficiently attenuate reflections from its output transition that were fed back to its input. In the 2 to 8 GHz active band of the tube [3], the attenuator loss, depicted in Figure 3.15 (b), was only about 10 dB. The return losses of the tube's transitions varied between about 6 and 15 dB (as stated in Section 2.4.2). These return losses were measured in the absence of an electron beam and would have been slightly worse in the presence of one [4], [5]. Substitution of these attenuation and return loss values into the instability condition of equation (3.1) yields a maximum stable gain of less than 22 dB for TWT LP8, very close to the actual, maximum gain measured on the verge of instability.

TWT LP8 exhibited gain from 3.8 to 7.5 GHz. It was however not strictly a braodband amplifier because of the gain ripple and the falloff in gain with frequency. The gain ripple was due to reflections from the imperfectly matched RF transitions and attenuator. A superior attenuator would suppress both the reflected signals and the ripple in the gain/frequency curve. A solid state preamplifier with equalization could be used at the TWT's input to compensate for the falloff in gain with frequency but a more practical solution would be to design the helix circuit for flat gain across the band, as was done for TWTs LP9 and LP10 [3].

8.3 TWT LP10, THE SECOND OPERATIONAL LOW PROFILE TWT

TWT LP10 was designed [3] to operate at an electron beam voltage and current of 4500 V and 80 mA respectively. When such a beam was used, the TWT was very unstable. Its output spectrum consisted of many spectral lines of various amplitudes between about 750 MHz and 15 GHz and a total RF output power of between 38 and 42 dBm was measured. This apparent, measured power was however lower than the actual power because the circulators and couplers in the RF test circuit were band limited (see Section 7.4). Output signals at frequencies that were out of their pass bands therefore reached the power meter after being attenuated by more than the 33 dB of 4 to 8 GHz signals.

The TWT was unstable because its transitions were not well matched and its attenuator did not sufficiently attenuate the resultant reflections. In the band that oscillations were observed in, the transitions had a return loss of 3 to 5 dB (see Figure 2.17 (b)) and the

attenuator had a loss of about 15 dB (see Section 3.4.2). Substitution of these attenuation and return loss values into the instability condition of equation (3.1), yields a maximum stable gain of less than 21 dB for TWT LP10. Although this figure is similar to that for TWT LP8, TWT LP10 was more unstable because it was designed to have more gain [3].

At one particular closed loop feedback frequency, 5.1 GHz, the electron beam was modulated heavily enough to suppress the gain at other frequencies sufficiently for total stability to be achieved. This would only occur for beam voltages of between 4540 and 4640 V with beam currents of 83 to 89 mA. A saturated gain of 16 dB was measured at the maximum output power of 43.3 dBm. The gain increased to 22 dB as the input signal strength was reduced whereafter control of the beam was lost and the TWT oscillated at many frequencies again. This phenomenon was not observed at any other frequency. Gain measurements at other frequencies were therefore not possible at these beam voltages and currents.

To achieve stability at 4500 V, the beam current was decreased by reducing the heater filament power. This cooled the cathode until its emission was temperature limited rather than space-charge limited. Good focusing of the resulting, low-current-density electron beam was possible by increasing the cathode-to-switching electrode potential.

As the beam current was decreased, stability increased and less spectral lines were measured by the HP8566B spectrum analyzer. The last spectral line, at 4.15 GHz, disappeared when the current was reduced to below 38 mA. A gain measurement was then made at 35 mA.

Since the HP8690B sweep oscillator was not available for open loop gain measurements, closed loop testing was used. The optional solid state power amplifier needed to be included in the feedback loop because the TWT gain was too low to overcome the losses in the circuit.

The simulated and measured gains for TWT LP10, operating with a 4500 V and 35 mA electron beam, are plotted in Figure 8.3. The measured gain was less than about 5 dB and about 25 to 40 dB below the simulated gain (which was calculated using the same method that was used to yield the curve of Figure 8.1). Reasons for the gain reduction

are given in Section 8.4. If the ripple in the gain curve (due to internal reflections in the tube) is ignored, the gain can be described as independent of frequency in the octave measured, a desirable characteristic in a broadband amplifier.

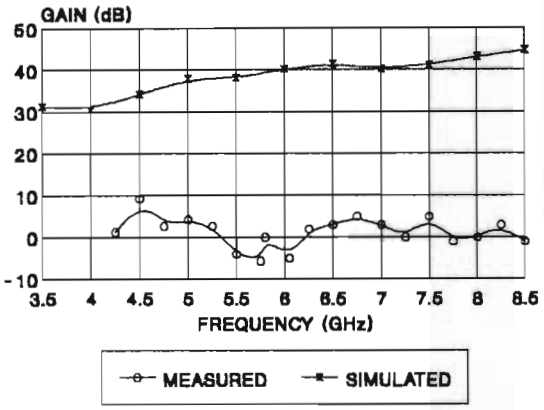

Figure 8.3 Measured and Simulated Gain at 4500 V and 35 mA

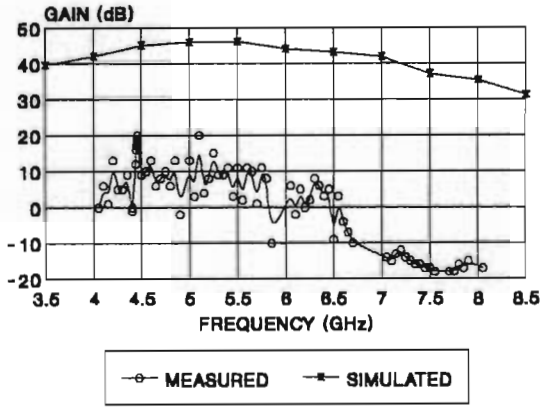

Figure 8.4 Measured and Simulated Gain at 5290 V and 89 mA

In addition to reducing its beam current at 4500 V, TWT LP10 could be made stable by increasing its beam voltage. This reduced the coupling between the beam and the helix circuit. The tube was just stable with a 5290 V, 89 mA beam, at which the gain measurement of Figure 8.4 was made. A gain of about 10 dB was measured between 4.5 and 5.5 GHz, about 35 dB less than that simulated (for the reasons discussed in Section 8.4). The simulation was made using the method in Section A.3, with modifications to account for a higher-than-synchronous beam voltage [3], [6]. The ripple in the measured gain was mainly due to the measurement method (see Section 7.4.2) and not the TWT. A negative slope, due to the higher-than-synchronous beam voltage, is present in the measured gain curve. TWT LP10 was therefore not at all active above 6.75 GHz, where the gain curve was the same as that for the cold TWT.

8.4 WHY WAS THE MEASURED GAIN LOWER THAN THE SIMULATED GAIN?

The measured gains of TWTs LP8 and LP10 were 20 to 40 dB lower than those simulated. An error in the calibration of the measurement system was suspected but checks found it to be accurate to better than 5 dB (see Section 7.4.2). The calculations of the simulation were also checked and found to be correct.

The simulation was simple and therefore did not properly account for effects due to the

attenuation and impedance mismatches of the attenuator, the impedance mismatches at the transitions, or the peculiarities of the electron beam and the helix. It is however unlikely that consideration of these effects would eliminate such a large difference between the measured and the simulated results [3]. The possibility is nevertheless under investigation by Reynolds [3].

If the problem lies neither with the simulations nor the measurement of the gain, it has to lie with the TWTs themselves. Both TWTs were unstable and the operation of both resulted in an increase in their internal pressure. Both these factors could have reduced the gain.

A reduction of gain can result from strong modulation of a tube's electron beam, as was demonstrated in the third paragraph of Section 8.3. Since TWTs LP8 and LP10 were both unstable, their gains could have been suppressed by strong oscillations of the electron beam at frequencies other than the input frequency. This was more likely to have occurred with TWT LP8, which was operated while not completely stable than with TWT LP10, which was made stable by reducing its beam current or increasing its beam voltage.

Since many gas molecules are present even at very low pressures, ions are continuously generated by electron collisions with some of the gas molecules in an operating tube. The concentration of ions in a beam depends on the pulse width and duty cycle of the beam, the gas pressure, the speed at which ions are drained towards a region of lower potential, and whether or not ions become trapped in a potential well. If high ionic concentrations result, the electron beam's space charge is neutralized. This neutralization may be significant. For example, a particular beam was reported [7] to have been about 14 per cent neutralized by ions at a pressure of 10^{-7} torr, about 50 per cent neutralized at 10^{-6} torr and almost fully neutralized at a few times 10^{-6} torr. Neutralization of space charge results in a reduction of the beam diameter (ion focussing) and a reduction of the gain and the output power of a TWT [8].

TWTs LP8 and LP10 were pumped to an ion pump pressure of 10^{-8} torr before operation but outgassing, due to elevated temperatures and electron bombardment, caused the pressure to rise during operation. The tubes therefore normally operated at ion pump pressures of between 10^{-8} and 10^{-6} torr. The actual pressure in the tubes' helix regions

could have been significantly higher than that in the ion pump. Gas molecules in these regions had to work their way through the hole in the anode, around the electrodes of the electron gun, through the pumping port and then travel via the pumping stem to the pump – a long, convoluted path (see Figure 1.1).

Although the gas pressure was high enough for significant ionic concentrations to have occurred, it has not been confirmed directly. Ionic buildup can be prevented if the beam is pulsed for short enough periods. The pulsing equipment that was available was however too slow to confirm any ionic effects in the tubes. These effects could also have been confirmed by high frequency oscillations of the electron beam but ionic oscillations were not noticed in the helix interception current, nor were "ion sidebands" clearly visible in the TWT output spectra. Only circumstantial evidence for ion focussing exists: the measured electron beam focusing of both tubes was good (see Section 4.5.2) and the TWT gain was lower than predicted.

The random, peak-to-peak helix pitch variations of 5 to 10 per cent were also investigated as a possible cause of gain reduction but these result in gain ripple, not gain reduction [9]. It has therefore been concluded that although approximations made in the calculations could account for part of the difference between the measured and the simulated gains, the gains had probably been reduced by ionic depression of space charge and/or oscillations at frequencies other than the input frequency.

8.5 CONCLUSIONS

TWT LP8, the first operational low profile TWT, exhibited a small-signal gain of over 10 dB from 3.8 to 7.5 GHz and delivered over 42 dBm of RF power when saturated at 4.1 GHz. The gain could be optimized by adjusting the beam voltage and focusing. TWT LP8 was not completely stable though due to its attenuator loss not being high enough to prevent internal feedback.

TWT LP10, the second operational low profile TWT, was unstable when a full beam current was used at the synchronous voltage. Its gain could be suppressed sufficiently to achieve stability by either reducing the beam current at a fixed voltage or by increasing the beam voltage until the electron beam and the circuit wave were no longer

strongly coupled. Operation at an increased voltage resulted in a reduction in gain with increasing frequency and in a narrower bandwidth than operation at a reduced current and synchronous voltage.

The gains measured for both TWT LP8 and LP10 were 20 to 40 dB lower than those simulated. Approximations made in the calculations could account for part of this difference but the gains had probably been reduced by ionic depression of space charge and/or oscillation at frequencies other than the input frequency.

Travelling wave interaction under PPM focusing, using low profile, TEM transitions has been demonstrated.

REFERENCES

[1] N. Vassilopoulos, B.D Foulis, C.G. Reynolds and H.L. Nattrass, "Description of an Operational Travelling Wave Tube Amplifier Employing PPM Focusing", *Proceedings of the Symposium on Antennas and Propagation and Microwave Theory and Techniques*, Kempton Park, South Africa, pp. 25-1 to 25-8, August 1993.

[2] J.R. Pierce, *Traveling-Wave Tubes*, D. Van Nostrand Company, Inc., Section 9.7, 1950.

[3] C.G. Reynolds, *The Analysis, Simulation and Testing of an Experimental Travelling-Wave Tube*, Ph.D. Thesis, Department of Electronic Engineering, University of Natal, 1994.

[4] S.O. Wallander, "Reflections and Gain Ripple in TWT's", *IEEE Transactions on Electron devices*, Vol. ED-19, No. 5, pp. 655 to 660, May 1972.

[5] A.J. Lichtenberg, "Prebunched Beam Traveling-Wave Tube Studies", *IRE Transactions on Electron Devices*, pp. 345 to 351, July 1962.

[6] Reference 2, Sections 3.1a, 3.1b and 8.2.

[7] M.E. Hines, G.W. Hoffman and J.A. Saloom, *Journal of Applied Physics*, Vol. 26, p. 1157, 1955.

[8] A.S. Gilmour, *Microwave Tubes*, Artech House, Section 7.4, 1986.

[9] J.P. Laico, H.L. McDowell and C.R. Moster, "A Medium Power Traveling-Wave Tube for 6,000-Mc Radio Relay", *The Bell System Technical Journal*, pp. 1285 to 1346, November 1956.

CHAPTER 9

CONCLUSIONS

Several, low profile TWTs with TEM transitions have been designed and made. TWT interaction has been demonstrated on two of them using an automated measurement station that was built. The low profile TWTs were removable from their PPM stacks and had TEM transitions. Some of these transitions were acceptably matched over a broad bandwidth. PPM focusing of electron beams has been demonstrated, as has the technological capability to make metal/ceramic TWTs. A method has been developed to make metal film TWT attenuators but some trial and error iterations are required before their correct film thickness is determined.

APPENDIX A

PIERCE'S SMALL-SIGNAL TWT GAIN THEORY [1], [2]

LIST OF SYMBOLS

a	helix radius
A	initial loss
b	velocity parameter
b	beam radius
B	increasing wave parameter
c	speed of light
C	gain parameter
d	loss parameter
G	gain
i	convection current
I	circuit current
I_0	beam current
J	displacement current
K	circuit impedance
ℓ	length of circuit
L	cold loss of circuit
L_w	total length of wire in helix
N	distance along circuit in wavelengths
Q	space charge parameter
R_0	beam impedance
u_0	average beam velocity
v	velocity of a wave on the cold circuit
V	circuit voltage
V_0	beam voltage
x	real part of incremental propagation constant
y	imaginary part of incremental propagation constant
α	gain reduction parameter
β_e	phase constant of a disturbance travelling with the electron beam
β_0	free space phase constant
γ_0	natural propagation constant of helix

Γ propagation constant

δ incremental propagation constant

λ free space wavelength

λ_g wavelength along helix axis

ω angular frequency of a disturbance travelling with the electron beam

ω_p angular frequency of plasma oscillations

A.1 INTRODUCTION

This appendix contains two parts. The first part is a summary of the small-signal TWT gain theory of Pierce [1]. The description is brief and is similar in outline to that of Gilmour [2]. The second part consists of Pierce's instructions for calculating the small-signal gain of a TWT.

A.2 AN OVERVIEW OF PIERCE'S THEORY

Pierce's simple theory of travelling wave interaction has become a classic since it was first published in 1947 [3]. Although his mathematics are not repeated here, some of Pierce's results are discussed.

Pierce's approach was to begin by modelling the RF circuit of a TWT as the transmission line shown in Figure A.1. In this model, the circuit voltage and current are ***V*** and ***I*** respectively and a convection current, ***i***, is assumed to pass very close to the circuit. A displacement current, ***J***, is induced onto the circuit by ***i*** and velocity modulation of the beam results from ***V***.

Using this model, an equation is derived for the circuit field caused by the induced current. An equation is also derived for the convection current produced by the field. These two equations are combined to determine the natural modes of propagation along the circuit/electron beam combination.

The resulting equation has four roots corresponding to four different propagation modes. The propagation constants are functions of many beam and circuit parameters such as

circuit phase velocity, cold circuit loss (the circuit is called cold when the beam is absent), and space charge.

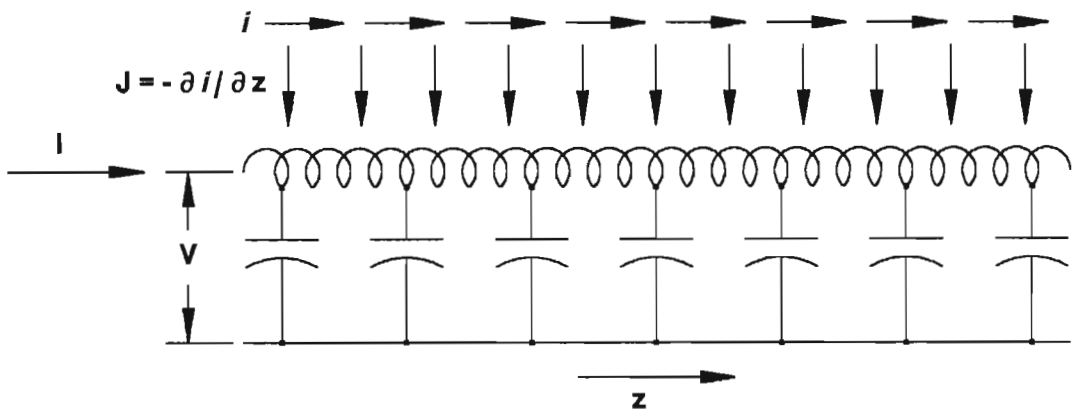

Figure A.1 Equivalent Circuit of a TWT

(After J.R. Pierce, *Traveling-Wave Tubes*, D. Van Nostrand Company, Inc., 1950.)

A simple synchronous case, in which the beam velocity equals the cold circuit phase velocity, is considered first. It is simple because the cold circuit loss and space charge effects are ignored. Modifications are then made to the synchronous solution to account for variations in circuit phase velocity, for losses and for space charge.

A.2.1 The Synchronous Case without Losses or Space Charge

In this case, the four propagation constants are:

$$-\Gamma(1) = -j\beta_e - j\frac{\beta_e C}{2} + \beta_e C\frac{\sqrt{3}}{2} \qquad (A.1)$$

$$-\Gamma(2) = -j\beta_e - j\frac{\beta_e C}{2} - \beta_e C\frac{\sqrt{3}}{2} \qquad (A.2)$$

$$-\Gamma(3) = -j\beta_e + j\beta_e C \qquad (A.3)$$

$$-\Gamma(4) = +j\beta_e - j\beta_e \frac{C^3}{4} \tag{A.4}$$

In these equations,

$$\beta_e = \frac{\omega}{u_0} \tag{A.5}$$

and

$$C^3 = \frac{K}{4R_0} \tag{A.6}$$

where β_e is the phase constant of a disturbance traveling with the electron beam; ω is the angular frequency of this disturbance; u_0 is the average beam velocity; C is Pierce's gain parameter; K is the circuit impedance; and R_0 is the beam impedance.

The circuit impedance is a measure of the electric field available for interaction with the electron beam. The beam impedance is the ratio of average beam voltage to average beam current.

The propagation constants (A.1) to (A.3) all include $-j\beta_e$, the propagation constant of the electron beam. Also included are some terms multiplied by C. Since C has a typical range of 0.01 to 0.1, these terms are small. These three waves therefore travel in the same direction as the electron beam and at similar speeds to it.

The propagation constant of (A.4) includes $+j\beta_e$. The fourth wave therefore travels in the opposite direction to the beam. The $-j\beta_e(C^3/4)$ term indicates that this wave travels slightly faster than the beam.

The $-j(\beta_e C/2)$ terms in (A.1) and (A.2) indicate that these two waves travel slower than the beam. The $+j\beta_e C$ term in (A.3) indicates that this wave travels faster than the beam.

The wave of (A.1) is a growing wave because its propagation constant includes a positive real part. The wave of (A.2) is a decaying wave. The waves of (A.3) and (A.4) neither grow nor decay.

The gain, G, for the synchronous case can be calculated from the real parts of the propagation constants. In Figure A.2, G is plotted against CN, where N is the distance along the circuit in wavelengths. The dashed line in the figure represents the growing

wave which can be calculated from:

$$G = A + BCN \tag{A.7}$$

where ***A*** is the initial loss due to the division of the applied voltage amongst the different waves and ***B*** is the increasing wave parameter, calculated directly from the real part of the propagation constant of the growing wave. In the synchronous case, without loss or space charge, the values of ***A*** and ***B*** are -9.54 dB and 47.3 respectively.

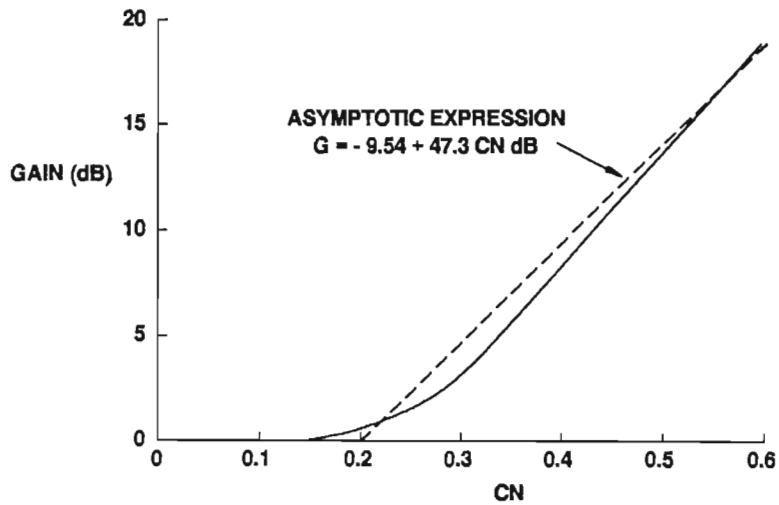

Figure A.2 Power Gain for Synchronous Case without Losses or Space Charge

(After J.R. Pierce, *Traveling-Wave Tubes*, D. Van Nostrand Company, Inc., 1950.)

A.2.2 The Non-Synchronous Case without Losses or Space Charge

When considering electron beam velocities, u_0, other than the velocity of a wave on the cold circuit, v_1, Pierce introduced a velocity parameter, ***b***, which relates u_0 to v_1:

$$u_0 = (1 + Cb)\ v_1 \tag{A.8}$$

Electrons travel faster than the cold circuit wave if ***b*** is positive and slower if negative. Substituting (A.8) into the expression for the propagation constant of waves on the cold circuit yields:

$$-\Gamma_1 = -j\frac{\omega}{v_1} = -j\beta_e(1 + Cb) \tag{A.9}$$

In addition to ***b***, Pierce introduced an incremental propagation constant, δ:

$$-\Gamma = -j\beta_e + \beta_e C\delta \tag{A.10}$$

The incremental propagation constant is a complex number with a real part ***x*** and an imaginary part ***y***:

$$\delta = x + jy \tag{A.11}$$

The travelling wave increases in amplitude if ***x*** is positive and decreases if negative. It travels faster than the electrons if ***y*** is positive and slower if negative. The values of ***x*** and ***y*** of the three forward waves can be computed as functions of the velocity parameter, ***b***. For the case without losses or space charge, the components of the first wave's incremental propagation constant, δ_1, are plotted against ***b*** in Figure A.3.

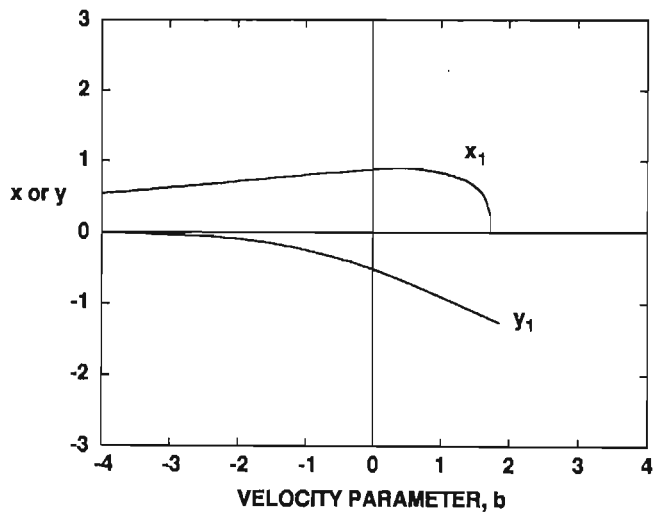

Figure A.3 Incremental Propagation Constant Components for Growing Wave

(After J.R. Pierce, *Traveling-Wave Tubes*, D. Van Nostrand Company, Inc., 1950.)

The real part, x_1, is positive over a large range of ***b***. Gain therefore occurs over a range of electron beam velocities. Since the imaginary part, y_1, is always negative, the growing wave always travels slower than the beam. This is explained qualitatively in Chapter 1.

A.2.3 The Effect of Loss

Some losses occur normally in RF circuits. Others are intentionally added to ensure TWT stability by attenuating feedback signals as discussed in Chapter 3. To account for these losses, Pierce introduced a circuit attenuation parameter, ***d***, into the propagation

constant of the cold circuit wave:

$$-\Gamma_1 = -j\beta_e(1 + Cb) - \beta_e Cd \tag{A.12}$$

here

$$d = 0.0183 \frac{L}{CN} \tag{A.13}$$

where L is the circuit loss in dB.

The circuit attenuation parameter results in a reduction of the real parts of the incremental propagation constants. The reduction in x_1 reduces the increasing wave parameter, B, as plotted in Figure A.4.

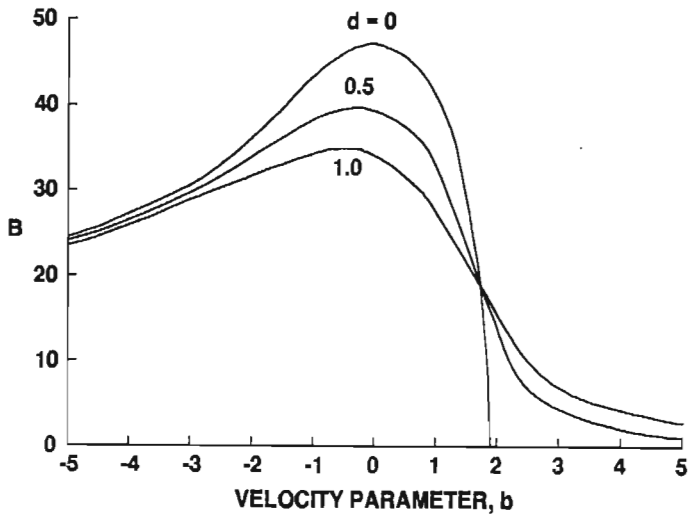

Figure A.4 Effect of Loss on *B* Factor in Gain of Increasing Wave

(After J.R. Pierce, *Traveling-Wave Tubes*, D. Van Nostrand Company, Inc., 1950.

A.2.4 The Effect of Space Charge

Space charge forces reduce the intensity of the bunches that form in the electron beam. They also result in plasma oscillations, in which the electron velocity, density, and current vary with distance [4].

When space charge is accounted for, the incremental propagation constants are modified and include a certain product, ***QC***. This is known as Pierce's space charge parameter and can be calculated by:

$$QC = \frac{\omega_p^2}{4\omega^2 C^2} \tag{A.14}$$

where ω_p is the angular frequency of the plasma oscillations.

The space charge parameter is a measure of the severity of space charge effects. Its effect on the incremental propagation constant of the growing wave is shown in Figure A.5. As ***QC*** increases, the range of beam velocities over which x_1 is positive, and gain occurs, is narrowed.

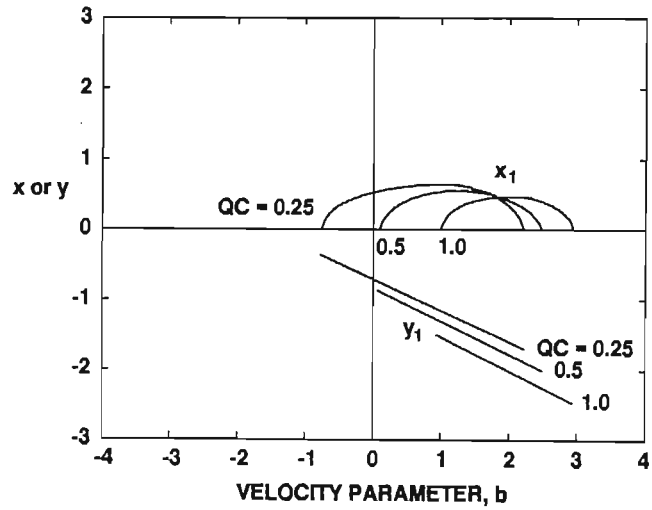

Figure A.5 Effect of Space Charge on Incremental Propagation Constants for Growing Wave and No Loss

(After A.S. Gilmour, *Microwave Tubes*, Artech House, 1986.)

A.2.5 Large Signal Gain

Pierce made certain assumptions and approximations in developing his small signal theory of TWT gain. These become less valid as signal levels grow and TWT operation becomes non-linear. As a result, the large signal gain of a TWT is lower than the small signal gain. This effect can be seen in Figure 8.2.

One reason for this gain reduction is that as the bunching process continues, space

charge forces increase making further bunching more difficult. Another reason is that the velocity of the beam is reduced as it gives up energy to the circuit wave. This results in the electron bunches moving out of phase with the circuit signal.

A point is reached where an increase in the input signal level does not result in an increase in output power. This saturation, also shown in Figure 8.2, occurs when the electron bunches begin to disperse and the amplitude of the circuit wave starts to decrease.

A.3 INSTRUCTIONS FOR CALCULATION OF SMALL-SIGNAL TWT GAIN [5]

The following calculation regards only the growing wave. It is accurate for TWTs with appreciable gain in which the effects of the other three waves are negligible.

The gain equation that approximately accounts for the cold loss of the circuit is:

$$G = A + BCN - \alpha L \qquad \text{(A.15)}$$

where G is the gain in dB; A is the initial loss in dB due to the division of the applied voltage amongst the different waves; B is the increasing wave parameter; C is Pierce's gain parameter; N is the length of the circuit in wavelengths; and α is the fraction of the cold loss, L, that needs to be subtracted from the gain.

The quantities A, B, C, N, α, and L are determined as follows:

A.3.1 Cold Loss in dB, L

This is best determined by measurement [6].

A.3.2 Length of Circuit in Wavelengths, *N*

This can be calculated by several methods. If ***c*** is the speed of light, u_0 is the speed of an electron and V_0 is the accelerating voltage, then:

$$\frac{c}{u_0} = \frac{505}{\sqrt{V_0}} \tag{A.16}$$

If ℓ is the length of the circuit, λ is the free space wavelength and λ_g is the wavelength along the axis of the helix, then:

$$\lambda_g = \lambda \frac{u_0}{c} \tag{A.17}$$

$$N = \frac{\ell}{\lambda_g} = \frac{\ell c}{\lambda u_0} \tag{A.18}$$

Or, if L_w is the total length of the wire in the helix:

$$N \cong \frac{L_w}{\lambda} \tag{A.19}$$

A.3.3 The Gain Parameter, *C*

The gain parameter can be expressed as:

$$C = \left(\frac{E^2}{\beta^2 P 8 V_0} \frac{I_0}{}\right)^{\frac{1}{3}} = \left(\frac{K I_0}{4 V_0}\right)^{\frac{1}{3}} \tag{A.20}$$

where ***K*** is the helix impedance (defined below), I_0 is the beam current and V_0 is the beam voltage.

A.3.4 The Helix Impedance, *K*

In Figure A.6, the term

$$K_s \left(\frac{\beta_0}{\gamma_0}\right)\left(1 + \left(\frac{\beta_0}{\gamma_0}\right)^2\right)^{\frac{3}{2}} \tag{A.21}$$

is plotted against $\gamma_0 a$ for different values of ***b/a***. K_s is the effective value of ***K*** for a solid electron beam of radius ***b*** inside a helix of radius ***a*** and natural propagation constant γ_0,

given by:

$$\gamma_0 = \frac{2\pi}{\lambda_g}\left(1 - \left(\frac{\lambda_g}{\lambda}\right)^2\right)^{\frac{1}{2}} \tag{A.22}$$

In most cases, the speed of the beam u_0 of (A.17) is low enough to make

$$\left(\frac{\lambda_g}{\lambda}\right)^2 < 1 \tag{A.23}$$

This yields the approximations

$$\gamma_0 = \frac{2\pi}{\lambda_g} \tag{A.24}$$

and

$$\gamma_0 a = \frac{2\pi a}{\lambda_g} \tag{A.25}$$

Now

$$\beta_0 = \frac{2\pi}{\lambda} \tag{A.26}$$

Therefore

$$1 + \left(\frac{\beta_0}{\gamma_0}\right)^2 = 1 + \left(\frac{\lambda_g}{\lambda}\right)^2 \tag{A.27}$$

and

$$\left(1 + \left(\frac{\beta_0}{\gamma_0}\right)^2\right)^{\frac{3}{2}} = 1 \tag{A.28}$$

Thus, K_s may be taken as the ordinate of Figure A.6 multiplied by c/u_0 from (A.16).

The impedance of a real helix may be somewhat less than this value of K_s which is for a helically conducting sheet.

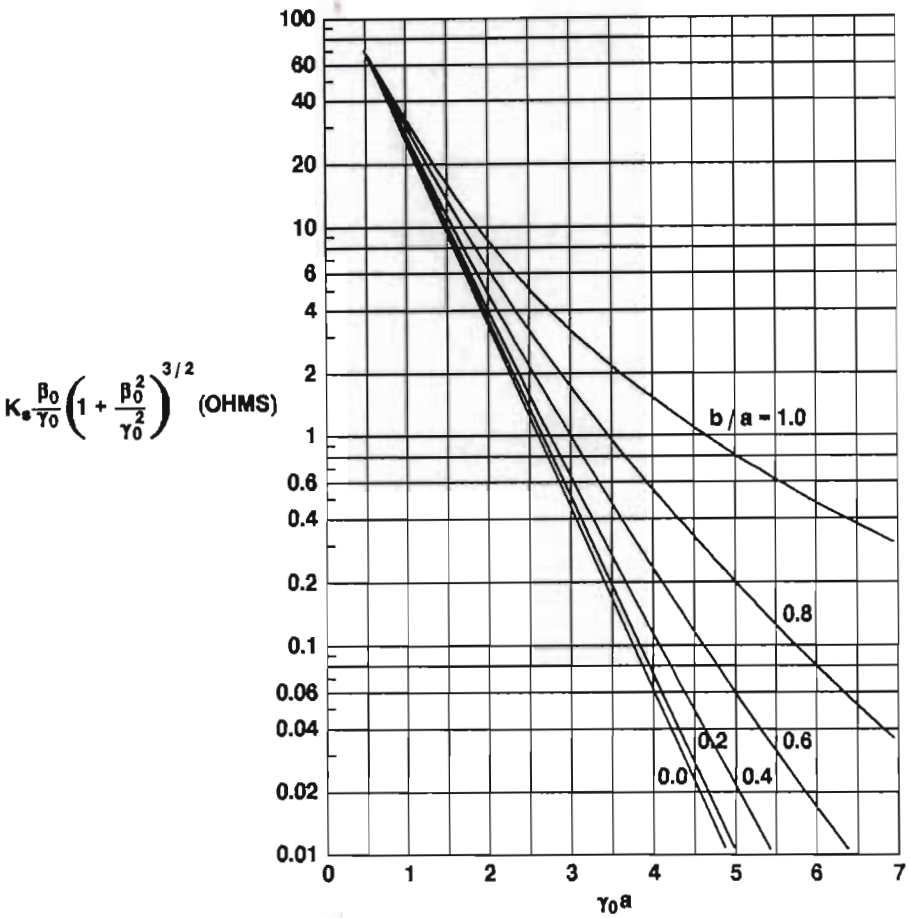

Figure A.6 Circuit Impedance K_s for a Solid Electron Beam

(After J.R. Pierce, *Traveling-Wave Tubes*, D. Van Nostrand Company, Inc., 1950.)

A.3.5 The Space Charge Parameter, *Q*

In Figure A.7, the quantity

$$Q_s \frac{\gamma_0}{\beta_e}\left(1 + \left(\frac{\beta_0}{\gamma_0}\right)^2\right)^{-\frac{1}{2}} \tag{A.29}$$

is plotted against γa for several values of b/a. Here Q_s is the effective Q for a solid beam of radius b. As before, the beam speed u_0 of (A.17) is usually low enough to make

$$\left(1 + \left(\frac{\beta_0}{\gamma_0}\right)^2\right)^{-\frac{1}{2}} = 1 \tag{A.30}$$

The quantity β_e of (A.29) is

$$\beta_e = \frac{2\pi a}{\lambda_g} \tag{A.31}$$

and from (A.22)

$$\beta_e = \gamma = \gamma_0 \tag{A.32}$$

for low beam speeds (and voltages). The ordinate of Figure A.7 can therefore be taken as Q_s.

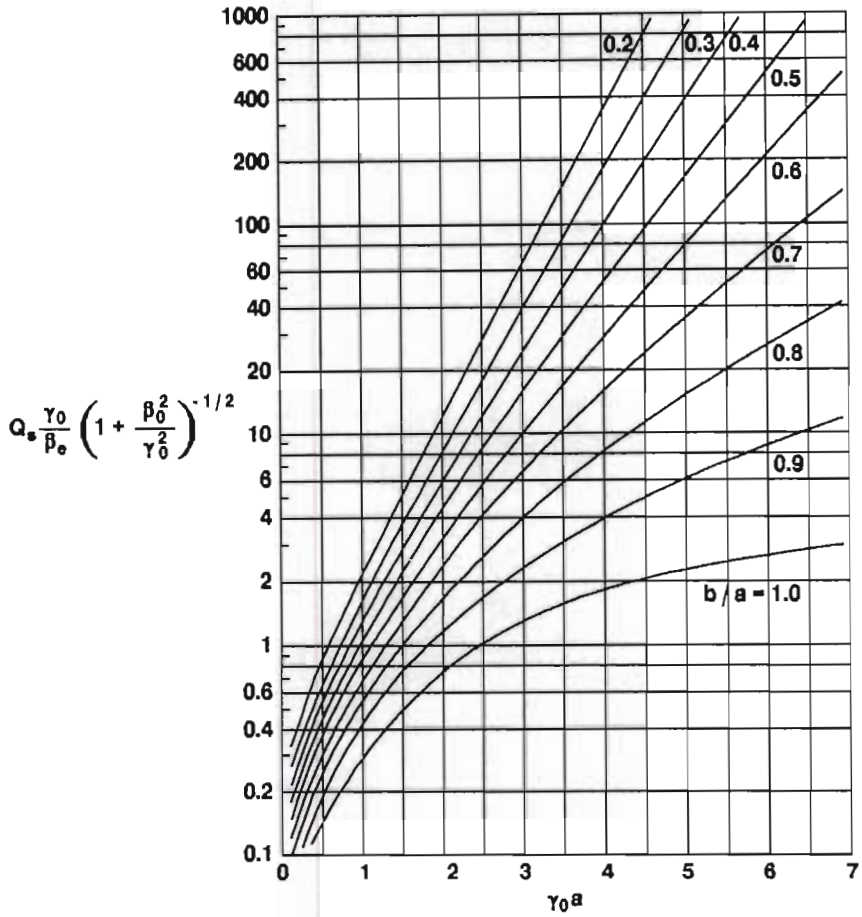

Figure A.7 Passive Mode Parameter Q_s for a Solid Electron Beam

(After J.R. Pierce, *Traveling-Wave Tubes*, D. Van Nostrand Company, Inc., 1950.)

A.3.6 The Increasing Wave Parameter, *B*

The increasing wave parameter is plotted against ***QC*** in Figure A.8.

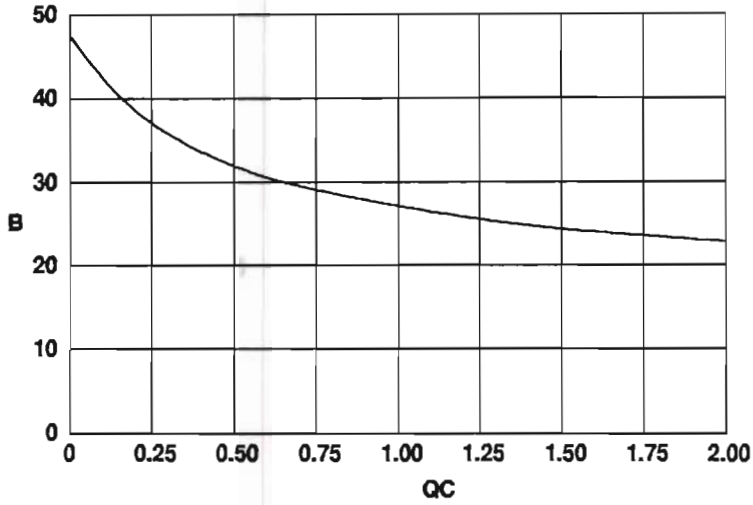

Figure A.8 The Increasing Wave Parameter, *B*

(After J.R. Pierce, *Traveling-Wave Tubes*, D. Van Nostrand Company, Inc., 1950.)

A.3.7 The Gain Reduction Parameter, α

The gain reduction parameter is equal to the magnitude of $\partial x_1 / \partial d$, which is plotted against QC in Figure A.9.

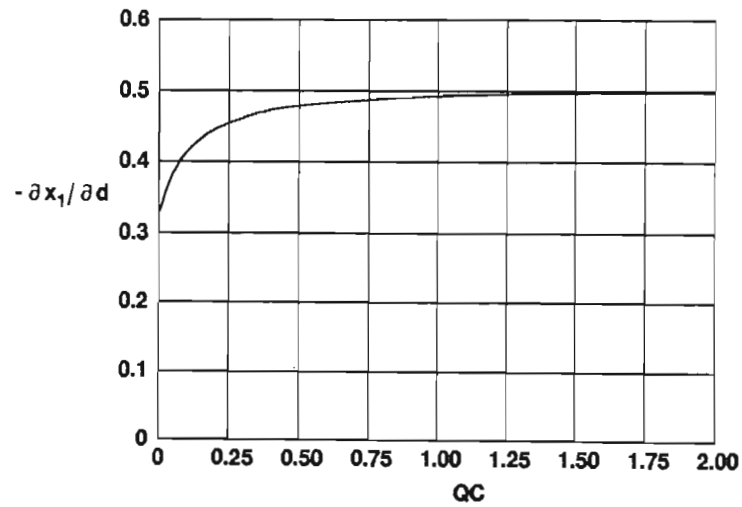

Figure A.9 The Rate of Change of x_1 with Attenuation Parameter d for d=0

(After J.R. Pierce, *Traveling-Wave Tubes*, D. Van Nostrand Company, Inc., 1950.)

A.3.8 The Loss Parameter, *d*

The loss parameter can be calculated from (A.13).

A.3.9 The Initial Loss, *A*

The initial loss is plotted against ***d*** in Figure A.10. The plot is for a space charge parameter, ***QC***, and a velocity parameter, ***b***, of zero and may therefore be somewhat in error. An error in ***A*** would put the gain, ***G***, in error by only a few dB however.

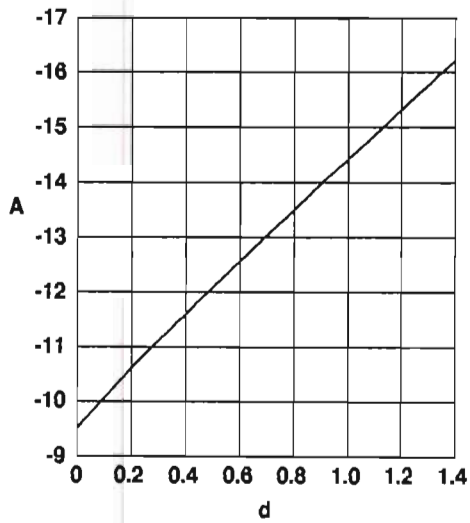

Figure A.10 The Relationship between *A* and *d* for *b* = 0 and *QC* = 0

(After J.R. Pierce, *Traveling-Wave Tubes*, D. Van Nostrand Company, Inc., 1950.)

REFERENCES

[1] J.R. Pierce, *Traveling-Wave Tubes*, D. Van Nostrand Company, Inc., 1950.

[2] A.S. Gilmour, *Microwave Tubes*, Artech House, pp. 242 to 258, 1986.

[3] J.R. Pierce, "Theory of the Beam-Type Traveling-Wave Tube", *Proc. I.R.E.*, Vol. 35, No. 2, p 111, February 1947.

[4] Reference [2], p. 217.

[5] Reference [1], Appendix VII.

[6] B.T.J. Maharaj, *Characterization of Helical Slow Wave Structures in Travelling Wave Tubes*, M.Sc. Thesis, Department of Electronic Engineering, University of Natal, 1989.

APPENDIX B

THE HP8510B VECTOR NETWORK ANALYZER [1], [2]

B.1 INTRODUCTION

The HP8510B Vector Network Analyzer is a powerful microwave measurements tool that accurately measures a network's scattering parameters. In this appendix these parameters are defined, their measurement with a vector network analyzer is described, and some concepts that need to be understood if the measurements are to be correctly interpreted are explained.

The Electronic Engineering Department of the University of Natal now has an HP8510C, recently upgraded from an HP8510B. The following notes are general and apply to both models.

B.2 SCATTERING PARAMETERS

A two-port network can be completely characterized by a set of four parameters. Low frequency parameter sets, such as the Y-parameters, are based on voltages and currents at the terminals of the two-port but at high frequencies these voltages and currents are difficult to measure and sometimes even difficult to define. Also, short and open circuits are required in the measurement of these parameters. These are difficult to realise over broad bandwidths and they result in the instability of most active devices.

Networks are characterized at high frequencies by measuring their input and output signals. Figure B.1 shows how some of the microwave energy incident on a network will be reflected from the input because of an impedance difference, some will be absorbed by the network and the rest will be transmitted through it.

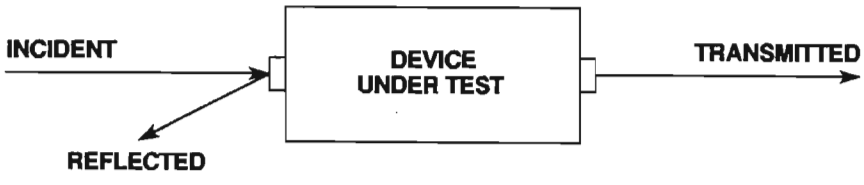

Figure B.1 Typical High Frequency Behaviour

The reflection coefficient (ρ) is defined as the voltage ratio of the reflected energy to the incident energy. The transmission coefficient ($\tau = 1+\rho$) is defined as the voltage ratio of the transmitted energy to the incident energy.

In the two-port network of Figure B.2, the incident waves have been called ***a*** waves and the output waves ***b*** waves.

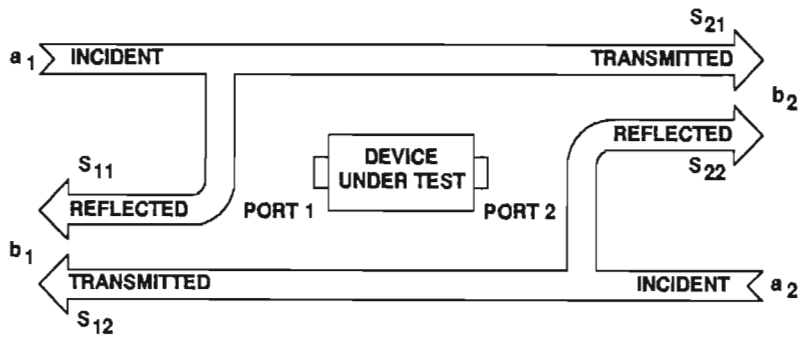

Figure B.2 Two-Port Network Scattering Parameters

Two linear equations are defined using the network's scattering or S-parameters and its ***a*** and ***b*** waves:

$$b_1 = S_{11}a_1 + S_{12}a_2 \qquad \text{(B.1)}$$

and

$$b_2 = S_{21}a_1 + S_{22}a_2 \qquad \text{(B.2)}$$

No short or open circuits are required to measure the S-parameters. To measure S_{11} and S_{21} the incident wave a_2 is made zero by terminating port two with a matched load (of impedance Z_0). This yields:

$$S_{11} = \frac{b_1}{a_1}\Big|_{a_2=0} \qquad \text{(B.3)}$$

and

$$S_{21} = \frac{b_2}{a_1}\Big|_{a_2=0} \qquad \text{(B.4)}$$

Similarly, a_1 is made zero to measure S_{22} and S_{12}:

$$S_{22} = \frac{b_2}{a_2}\Big|_{a_1=0} \qquad \text{(B.5)}$$

and

$$S_{12} = \frac{b_1}{a_2}\Big|_{a_1=0} \qquad \text{(B.6)}$$

B.3 VECTOR NETWORK ANALYSIS

A vector network analyzer measures both the magnitude and the phase of the S-parameters of a device under test (DUT). This DUT can be a one-port or a two-port network.

A network analyzer measurement system consists of the four major parts shown in Figure B.3: a signal source; signal separation devices; a receiver; and a signal processor/display section.

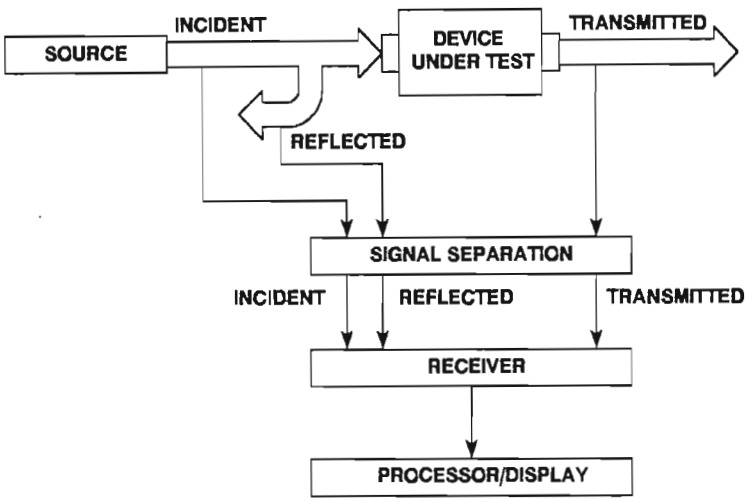

Figure B.3 Basic Network Analyzer Block Diagram

The signal source provides the incident signal. The frequency response of a DUT is measured by sweeping the synthesized source over a desired frequency range. Synthesized sources are used since they offer high stability and accuracy, and are thus suitable even for narrowband measurements. The HP8510C network analyzer at the University of Natal can make measurements in the 45 MHz to 26.5 GHz band.

The signal separation devices separate the incident, the reflected and the transmitted signals. The microwave signals are fed to a receiver that converts them to lower, intermediate frequency (IF) signals. Precision magnitude and phase measurements are made at the intermediate frequency.

The signal processor mathematically manipulates the measured data and corrects systematic measurement errors. Corrected measurement results are then displayed on a CRT in a range of formats and units of measure. The reflection parameters S_{11} and S_{22}

can be displayed directly, or as: VSWR; return loss; impedance; or reflection coefficient. Similarly, the transmission parameters S_{21} and S_{12} can be displayed directly, or as: device gain/loss; isolation; insertion phase; transmission coefficient; deviation from linear phase; group delay; or electrical length.

B.4 ACCURACY IMPROVEMENT BY CALIBRATION

Several sources of measurement error exist. These errors fall into one of three categories: systematic errors; random errors; and drift errors. The powerful measurements possible with the HP8510B are due to the significant increase in measurement accuracy that results from the mathematical removal of systematic errors.

Systematic errors are due to the imperfect nature of real devices. Crosstalk, impedance mismatch signals, and circuit element frequency responses, all contribute towards systematic measurement errors. Systematic errors are the most significant source of measurement uncertainty in most microwave measurements. These errors, however, are stable and repeatable and if quantified, can be mathematically removed.

The systematic errors are measured by connecting various high quality standards to the HP8510B during a calibration procedure. For example, three standards (a matched load, a short circuit and an open circuit) are required to characterize the three errors present in reflection measurements. The error vectors that are measured during the calibration procedure are stored in memory and used to correct each raw measurement datum. A small residual value of systematic error, due to imperfections in the calibration standards, does however remain.

After the calibration procedure, the reference plane of each measurement port is at the point where the reference standards were connected to the port. The linear magnitude of the test signal is unity at the reference plane and the phase of the test signal is zero. A reference plane can be moved by mathematically inserting an electrical delay. This provides more flexibility in insertion phase and Smith chart measurements.

Random errors are due to noise and connector repeatability. Noise errors are reduced by averaging and smoothing. Connector errors are reduced by using high quality

connectors and a minimum number of adaptors. It is important to keep connectors clean and to be aware of the degradation of lower quality connectors with each connection.

Drift errors are related to temperature, pressure, humidity, and other time dependant variables. They are best reduced by: allowing enough time for the HP8510B to warm up after switching it on; maintaining a constant ambient temperature; making measurements soon after calibration of the network analyzer; and checking its calibration after making measurements.

B.5 TIME DOMAIN MEASUREMENTS

A network analyzer measures in the frequency domain but it can also make time domain measurements by computing time domain results from frequency domain data using the inverse Fourier transform.

Time domain measurements show how a network responds to a specific waveform. Three types of network excitation waveforms are available on the HP8510B: a step; an impulse; and a band pass impulse. All three are shown schematically in Figure B.4. The calculated time domain responses of the network analyzer are identical to the responses measured by time domain reflectometer (TDR) instruments that actually send these excitation signals to a network.

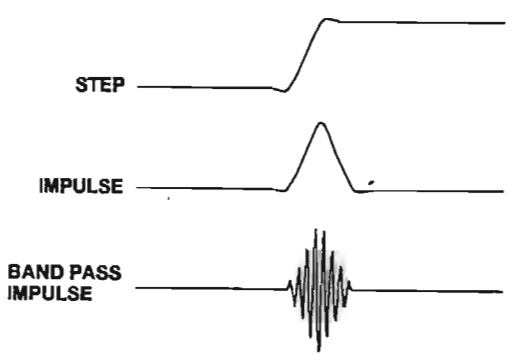

Figure B.4 Excitation Waveforms

Frequency domain data completely characterizes a DUT but gives no clue about what is causing a particular measured response. In the time domain however, the components of the reflected and the transmitted waves can be identified.

Time domain reflection measurements show the location and the impedance of different elements inside a circuit and the effects of internal re-reflections. Reflected response signals are shown normalised to the incident waveform. The real part of the data is the reflection coefficient as a function of time. The time axis corresponds to twice the time taken to reach each discontinuity. This is because an excitation signal must first travel to a discontinuity before a reflected response can travel back.

Time domain transmission measurements show main signal paths, isolation problems and internal re-reflections. The magnitude of the transmitted signal is the transmission coefficient of a given transmission path and the delay of the signal is equal to the propagation time through the transmission path.

B.6 INTERPRETATION OF TIME DOMAIN MEASUREMENTS

Figure B.5 shows the impulse and step responses due to various circuit elements.

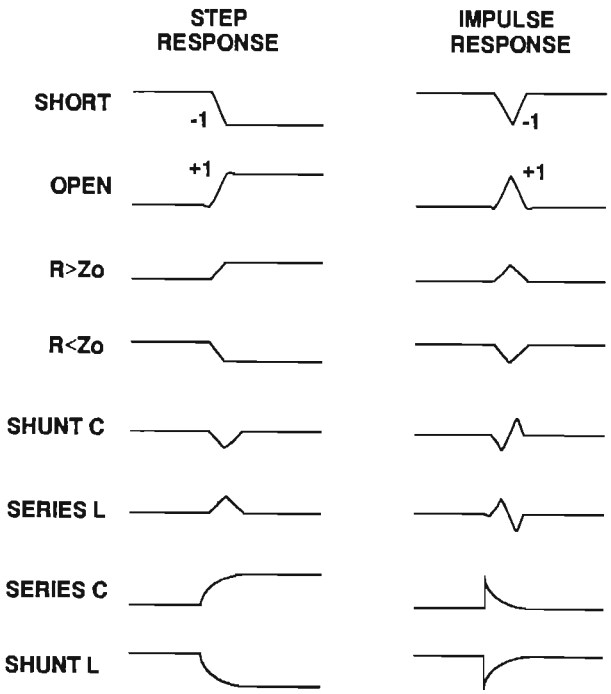

Figure B.5 Characteristic Time Domain Responses

Correct interpretation of time domain measurements requires an understanding of masking, alias free range, and resolution.

B.6.1 Masking

Masking is a physical phenomenon observed in time domain measurements where the response of one discontinuity affects the response of each subsequent discontinuity in the circuit.

There are two causes of masking. First, the energy reflected from one discontinuity will not reach the next discontinuity. Second, the energy absorbed by a lossy part of a circuit will never reach other parts of the circuit.

It is important that the loss of stimulus energy by both reflection and absorption be considered when interpreting time domain responses.

B.6.2 Alias Free Range

The inverse Fourier transform of continuous frequency domain data results in a single response in the time domain. If the frequency domain data is discrete, as in the HP8510B, the time domain response will repeat itself with a repetition time equal to the inverse of the frequency step size. This time determines the range of a time domain measurement.

The alias free range is defined as the length in time over which a measurement can be made without encountering a repetition of the response. Aliasing is defined as the overlap of a response with a repetition of the response and aliasing will occur if a response is longer than the alias free range.

B.6.3 Resolution

In reflection measurements, two discontinuities must be further apart than a specific minimum spacing before their responses can be uniquely defined. This spacing is a function of the rise time or the pulse width of the measurement stimulus. Similarly, the difference in length between two transmission paths must be greater than a specific minimum difference before the paths can be uniquely identified.

Response resolution is the minimum time spacing between two equal responses that allows each response to be uniquely identified. It is defined to be the 10 to 90 per cent rise time or the 50 per cent pulse width of the stimulus.

A tradeoff exists between range and resolution. A large frequency span is required to provide good resolution but this results in a small range.

B.7 GATING

Gating is a powerful feature that provides the flexibility to choose the interesting part of a time domain response and then convert back to the frequency domain as illustrated in Figure B.6. This removes the effects of the responses outside the gate from the frequency domain measurement.

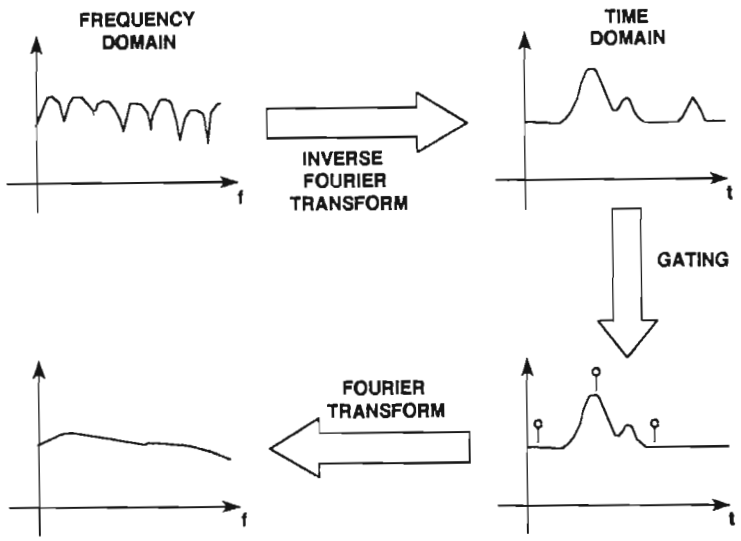

Figure B.6 The Time Domain Gating Operation

Gating errors are minimized if the gate is centred on the response of interest and is wide enough to include the whole response. Incomplete removal of nearby responses also results in errors, especially if the responses are large in magnitude and close in time to the retained response. Masking must also be considered when gating. The reflection response of the first of a series of discontinuities is not masked, however, and needs no special interpretation.

REFERENCES

[1] *Vector Measurements of High Frequency Networks*, Hewlett Packard Seminar Notes, April 1989.

[2] *Student Guide for Basic Network Measurements using the HP8510B Network Analyzer System*, HP Course Number HP8510B+24D, Edition 3.0, January 1988.

APPENDIX C

NUMERICAL SOLUTION OF THE PPM PARAXIAL RAY EQUATION

C.1 INTRODUCTION

The paraxial ray equation for a cosinusoidal magnetic field is a second order differential equation that relates beam radius to axial position. The equation was solved numerically using a method similar to that of Stokes [1].

C.2 THE PARAXIAL RAY EQUATION

Two assumptions were made in deriving the equation of motion for an electron at the edge of a beam in a periodic magnetic field: the magnetic field is axially symmetric and uniform over the beam cross section; and the electric field due to space charge acts only in a radial direction [2].

The paraxial ray equation, in the form given by Mendel *et al*, is [2]:

$$\ddot{\sigma} + \alpha(1 + \cos 2T)\sigma - \frac{\beta}{\sigma} = 0 \qquad \text{(C.1)}$$

where the magnetic field parameter is defined as

$$\alpha = \frac{1}{2}\left(\frac{\omega_L}{\omega}\right)^2 \qquad \text{(C.2)}$$

the space charge parameter is defined as

$$\beta = \frac{1}{2}\left(\frac{\omega_\rho}{\omega}\right)^2 \qquad \text{(C.3)}$$

and the above variables are defined as

$$\omega_\rho^2 = \frac{\rho\eta}{\varepsilon} \qquad z = u_0 t$$

$$\omega_L = \frac{1}{2}\eta B_0 \qquad \ddot{\sigma} = \frac{d^2\sigma}{dT^2}$$

$$\omega = \frac{2\pi u_0}{L} \qquad \sigma = \frac{r}{r_0}$$

$$\eta = \left|\frac{e}{m}\right| \qquad T = \omega t$$

where ρ is the volume charge density; ε is the dielectric permittivity; B_0 is the peak value of the longitudinal magnetic field at the axis; u_0 is the beam velocity; L is the magnetic field period; e is the electronic charge; m is the electronic mass; z is axial position; t is time; r is the beam radius; and r_0 is the initial beam radius.

C.3 NUMERICAL SOLUTION OF THE PARAXIAL RAY EQUATION

Equation (C.1) can be written as:

$$\ddot{\sigma} = \frac{\beta}{\sigma} - \alpha(1 + \cos 2T)\sigma \tag{C.4}$$

This can be rewritten as a system of two first order differential equations:

$$\dot{y}_1 = \frac{\beta}{y_2} - \alpha(1 + \cos 2T)y_2 \tag{C.5}$$

and

$$\dot{y}_2 = y_1 \tag{C.6}$$

where

$$y_1 = \dot{\sigma}$$

and

$$y_2 = \sigma$$

The system of equations was solved numerically using MATLAB (a numeric computation software package by The MathWorks, Inc.). A MATLAB function called ODE23 exists for solving such systems of ordinary differential equations. Solution is by automatic step size Runge-Kutta-Fehlberg integration methods and the algorithm uses a pair of second and third order formulae. Code was added to the ODE23 function to account for different magnetic periods and different magnetization profiles. This was easily done by using different values of L and B_0 to calculate α and β as T varied. The code required the initial values of normalized beam radius (y_1) and of radial velocity (y_2) to start the calculation. The effects of different beam diameters could be investigated by using initial normalised beam radii other than unity. Stack entry by diverging or converging beams could be simulated by using nonzero initial radial velocities. The solutions, y_1 and y_2, are

functions of T, and hence of axial position. Simulated results were plotted against T which increases by 2π with every PPM stack wavelength. The T axis is therefore titled "AXIAL POSITION IN PPM STACK PERIODS" and radians are given as its units.

The field at the entrance to each PPM stack, for example the one shown in Figure C.1, was more sinusoidal than cosinusoidal. Since equation (C.1) applies to cosinusoidal fields only, conversion of actual entry fields to equivalent ideal entry fields of corresponding amplitude (see Chapter 4, Section 4.2.2) was necessary. The solution was valid for the field in the middle of each stack since the field was virtually cosinusoidal. This is shown in Figure C.2 in which a cosinusoid has been superimposed on the profile of Figure C.1.

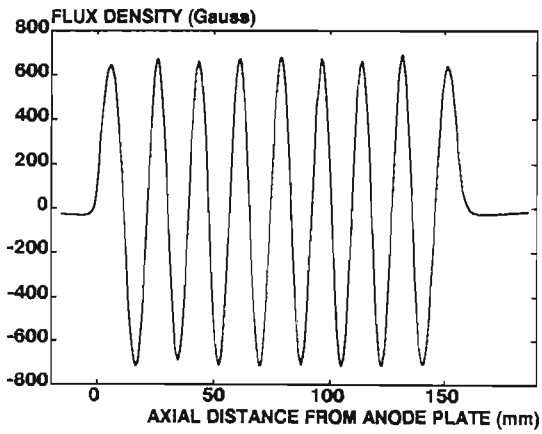

Figure C.1 Field Profile of the Stack of Figure 4.16

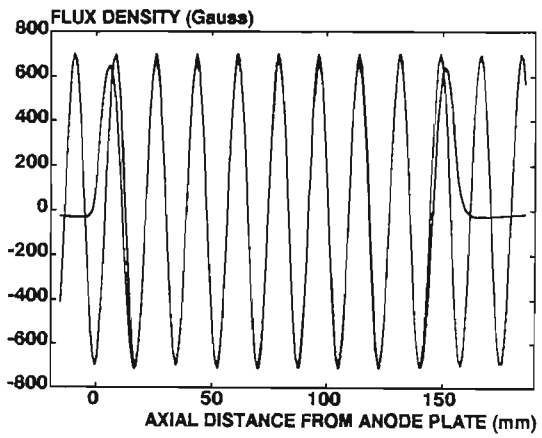

Figure C.2 Field Profile of the Stack of Figure 4.16 and Superimposed Cosine Wave

REFERENCES

[1] A.W. Stokes, *Magnetic Focusing of Electron Beams for Linear Beam Tubes*, M.Sc. Thesis, Department of Electronic Engineering, University of Natal, p. 81, July 1990.

[2] J.T. Mendel, C.F. Quate and W.H. Yocom, "Electron Beam Focusing with Periodic Permanent Magnet Fields", *IRE Proc.*, Vol. 42, pp. 800 to 810, May 1954.